

Integrated Ocean Drilling Program Expedition 333 Preliminary Report

NanTroSEIZE Stage 2: subduction inputs 2 and heat flow

12 December 2010–10 January 2011

Expedition 333 Scientists



Published by
Integrated Ocean Drilling Program Management International, Inc.,
for the Integrated Ocean Drilling Program

Publisher's notes

Material in this publication may be copied without restraint for library, abstract service, educational, or personal research purposes; however, this source should be appropriately acknowledged. Core samples and the wider set of data from the science program covered in this report are under moratorium and accessible only to Science Party members until 18 May 2012.

Citation:

Expedition 333 Scientists, 2011. NanTroSEIZE Stage 2: subduction inputs 2 and heat flow. *IODP Prel. Rept.*, 333. doi:10.2204/iodp.pr.333.2011

Distribution:

Electronic copies of this series may be obtained from the Integrated Ocean Drilling Program (IODP) Scientific Publications homepage on the World Wide Web at www.iodp.org/scientific-publications/.

This publication was prepared by the Japanese Implementing Organization, Center for Deep Earth Exploration (CDEX) at the Japan Agency for Marine-Earth Science and Technology (JAMSTEC), as an account of work performed under the international Integrated Ocean Drilling Program (IODP), which is managed by IODP Management International (IODP-MI), Inc. Funding for the program is provided by the following agencies:

National Science Foundation (NSF), United States

Ministry of Education, Culture, Sports, Science and Technology (MEXT), Japan

European Consortium for Ocean Research Drilling (ECORD)

Ministry of Science and Technology (MOST), People's Republic of China

Korea Institute of Geoscience and Mineral Resources (KIGAM)

Australian Research Council (ARC) and GNS Science (New Zealand),
Australian/New Zealand Consortium

Ministry of Earth Sciences (MoES), India

Disclaimer

Any opinions, findings, and conclusions or recommendations expressed in this publication are those of the author(s) and do not necessarily reflect the views of the participating agencies, IODP Management International, Inc., or Japan Agency for Marine-Earth Science and Technology.

Expedition 333 participants

Expedition 333 scientists

Pierre Henry
Co-Chief Scientist
Centre Européen de Recherche et
d'Enseignement des Géosciences
de l'Environnement
BP 80, 13545 Aix en Provence Cedex 04
Europole de l'Arbois, Bat Trocadero
France
henry@cerege.fr

Toshiya Kanamatsu
Co-chief Scientist
Institute for Research on Earth Evolution
Japan Agency for Marine-Earth Science and
Technology
2-15 Natsushima-cho, Yokosuka
Kanagawa 237-0061
Japan
toshiya@jamstec.go.jp

Moe Kyaw Thu
Expedition Project Manager
Center for Deep Earth Exploration
Japan Agency for Marine-Earth Science and
Technology
3173-25 Showa-machi, Kanazawa-ku
Yokohama, Kanagawa 236-0001
Japan
moe@jamstec.go.jp

Tiago Alves
Sedimentologist
Cardiff University
Park Place
Cardiff CF10 3AT
United Kingdom
alvest@cardiff.ac.uk

Thorsten Bauersachs
Organic Geochemist
Department of Organic Geochemistry
Institute for Geosciences
Christian-Albrechts-University
Ludewig-Meyn-Straße 10
24118 Kiel
Germany
thb@gpi.uni-kiel.de

Hugh Daigle
Physical Properties Specialist
Department of Earth Science
Rice University
6100 Main Street, MS 126
Houston TX 77005
USA
hugh.c.daigle@rice.edu

Koray Ekinci
Sedimentologist
Department of Geological Sciences
University of Missouri-Columbia
101 Geology Building
Columbia MO 65201
korayekinci@gmail.com

Shu Gao
Sedimentologist
School of Geographic and Oceanographic
Sciences
Nanjing University
22 Hankou Road
Nanjing
P.R. China
shugao@nju.edu.cn

Marion Garcon
Inorganic Geochemist
Laboratoire de Géodynamique des Chaînes
Alpines
BP 53, 38041 Grenoble Cedex 09
France
marion.garcon@ujf-grenoble.fr

Kiichiro Kawamura
Paleomagnetist
Fukada Geological Institute
2-13-12 Honkomagome
Bunkyo, Tokyo 113-0021
Japan
kichiro@fgi.or.jp

Yujin Kitamura

Paleomagnetist

Institute for Research on Earth Evolution
Japan Agency for Marine-Earth Science and
Technology

2-15 Natsushima-cho, Yokosuka

Kanagawa 237-0061

Japan

ykitamura@jamstec.go.jp

Jan Sverre Laberg

Sedimentologist

Department of Geology

University of Tromsø

N-9037 Tromsø

Norway

jan.laberg@uit.no

Gwangsoo Lee

Physical Properties Specialist

Department of Energy Resources Engineering

Pukyong National University

599-1, Daeyeon 3-Dong, Nam-Gu

Busan 608-737

Korea

coolks@pknu.ac.kr

Youngmin Lee

Physical Properties Specialist

Geothermal Resources Department

Korea Institute of Geoscience and Mineral
Resources

92 Gwahang-no, Yuseong-gu

Daejeon 305-350

Korea

ymlee@kigam.re.kr

Yuehan Lu

Organic Geochemist

Department of Geological Sciences

University of Alabama

Tuscaloosa AL 35487

USA

yuehan.lu@ua.edu

Boris Marcaillou

Physical Properties Specialist

Université des Antilles et de la Guyane (UAG)

Département de Géologie,

Campus de Fouillole

BP 592

Pointe a Pitre

97159 Guadeloupe

France

boris.marcaillou@univ-ag.fr

Osamu Matsubayashi

Physical Properties Specialist

National Institute of Advanced Industrial
Science and Technology

Institute for Geo-Resources and Environment

AIST Central 7

1-1-1 Higashi

Tsukuba, Ibaraki 305-8567

Japan

matsubayashi-osamu@aist.go.jp

Yoshitaka Nagahashi

Sedimentologist

Fukushima University

Faculty of Symbiotic Systems Science

1 Kanayagawa

Fukushima 960-1296

Japan

nagahashi@sss.fukushima-u.ac.jp

Beth Novak

Paleomagnetist

Department of Geology

Western Washington University

516 High Street

Bellingham WA 98225-9080

USA

novakb@students.wvu.edu

Yu Saito

Inorganic Geochemist

Doshisha University

1-3 Tatara Miyakodani

Kyotanabe City 610-0394

Japan

yu-saitoh@chikyu.ac.jp

Yasufumi Satoguchi

Sedimentologist

Lake Biwa Museum

1091 Oroshimo, Kusatsu

Shiga 525-0001

Japan

satoguti@lbm.go.jp

Elizabeth Sreaton

Physical Properties Specialist

University of Florida

Department of Geological Sciences

PO Box 112120

241 Williamson

Gainesville FL 32611

USA

sreaton@ufl.edu

Rachel P. Scudder
Inorganic Geochemist
Boston University
Department of Earth Sciences
675 Commonwealth Avenue, Room 141
Boston MA 02215
USA
rscudder@bu.edu

Bo Ra Song
Structural Geologist
Rice University
Department of Earth Science
6100 Main Street, MS 126
Houston TX 77005
USA
bora.song@rice.edu

Michael Strasser
Stratigraphic Correlator
MARUM Centre for Marine Environmental
Sciences
Department of Earth and Planetary Science
Bremen University
Leobener Strasse
28359 Bremen
Germany
mstrasser@uni-bremen.de

Asuka Yamaguchi
Structural Geologist
University of Tokyo
7-3-1 Hongo, Bunkyo-ku
Tokyo 113-0033
Japan
asukay@eps.s.u-tokyo.ac.jp

NanTroSEIZE chief project scientists

Masataka Kinoshita
Institute for Research on Earth Evolution
Japan Agency for Marine-Earth Science and
Technology
2-15 Natsushima-cho, Yokosuka
Kanagawa 237-0061
Japan
masa@jamstec.go.jp

Harold Tobin
Department of Geology and Geophysics
University of Wisconsin-Madison
1215 West Dayton Street
Madison WI 53706
USA
htobin@wisc.edu

NanTroSEIZE specialty coordinators

Toshiya Kanamatsu
Paleomagnetism/Biostratigraphy
Institute for Research on Earth Evolution
Japan Agency for Marine-Earth Science and
Technology
2-15 Natsushima-cho, Yokosuka
Kanagawa 237-0061
Japan
toshiyak@jamstec.go.jp

Gaku Kimura
Structural Geology
Department of Earth and Planetary Science
Graduate School of Science
University of Tokyo
7-3-1 Hongo, Bunkyo-ku
Tokyo 113-0033
Japan
gaku@eps.s.u-tokyo.ac.jp

Gregory Moore
Core-Log-Seismic Integration
Department of Geology and Geophysics
University of Hawaii
1680 East-West Road
Honolulu HI 96822
USA
gmoore@hawaii.edu

Demian Saffer
Physical Properties and Hydrogeology
The Pennsylvania State University
0310 Deike Building
University Park PA 16802
USA
dsaffer@geosc.psu.edu

Michael B. Underwood
**Lithostratigraphy and Sedimentary
Petrology**
University of Missouri
307 Geology Building
Columbia MO 65211
USA
underwoodm@missouri.edu

Geoff Wheat
Geochemistry and Microbiology
School of Fisheries and Ocean Sciences
University of Alaska Fairbanks
PO Box 475
Moss Landing CA 99775
USA
wheat@mbari.org

Shipboard personnel and technical representatives

Captains (Mantle Quest Japan)

Yasushi Minoura
Yuji Onda

Offshore Installation Managers (Mantle Quest Japan)

Seizaburo Higuchi
Stephen Krukowski

Operations Superintendents (CDEX)

Ikuo Sawada
Tomo Saruhashi

Drilling Engineers (CDEX)

Toru Aoki
Daiji Ikenomoto
Yasuhiro Kawano
Tadashi Otani

Operation Geologists (CDEX)

Kan Aoike
Takayasu Honda
Toshiro Kaminishi
Takuya Maeda
Kazuhiro Takahashi

Downhole Measurement Specialists (CDEX)

Yoshinori Sanada
Takamitsu Sugihara

Lab Manager (CDEX)

Chiaki Igarashi

Information Technology Managers (CDEX)

Yoshihiro Shiga
Kyoma Takahashi

Technical Advisors (CDEX)

Kazuyasu Wada
Yuichi Shinmoto

Curator and Assistant Curators (Marine Works Japan)

Yohei Arakawa
Toshikuni Yabuki
Masaru Yasunaga

Publications Assistant (Marine Works Japan)

Yoko Isoda

Coring Supervisor (AAI)

Marshall Pardey

Laboratory Officers (Marine Works Japan)

Tomoyuki Tanaka
Hiroaki Muraki

Assistant Laboratory Officers (Marine Works Japan)

Toru Fujiki
Shunsuke Miyabe
Soichi Moriya

Laboratory Technicians (Marine Works Japan)

Atsushi Ohashi
Akihiko Fujihara
Yuji Fuwa
Ei Hatakeyama
Yoshiki Kido
Yutaka Matsuura
Shunsuke Miyabe
Yuya Hitomi
Tatsuya Kawai
Sayaka Kawamura
Ryo Kurihara
Lena Maeda
Takami Mori
Masahiro Nishimura
Satomi Saito
Masumi Sakaguchi
Yusuke Sato
Kei Suminaga
Junki Sumizawa
Takahiro Suzuki
Naotaka Togashi
Yasumi Yamada
Nagisa Yamamoto

Abstract

The Nankai Trough Seismogenic Zone Experiment (NanTroSEIZE) program is a coordinated, multiexpedition drilling project designed to investigate fault mechanics and seismogenesis along subduction megathrusts through direct sampling, in situ measurements, and long-term monitoring in conjunction with allied laboratory and numerical modeling studies. Some of the fundamental scientific objectives of the NanTroSEIZE drilling project include characterizing the nature of fault slip and strain accumulation, fault and wall rock composition, fault architecture, and state variables throughout the active plate boundary system to a depth of 7000 m below seafloor. It is also important to show how such properties evolve from shallow, presubduction conditions in the Shikoku Basin to greater depths of the accretionary prism where fault slip is seismogenic. Within this context, the primary goals for Integrated Ocean Drilling Program (IODP) Expedition 333 were: (1) drilling and coring of previously unsampled intervals of sediment and basalt at IODP Sites C0011 and C0012 in the Shikoku Basin, together with downhole measurements of temperature, and (2) drilling and coring at a site near the updip terminus of the megasplay fault, as proposed in Ancillary Project Letter (738-APL: Nankai Trough Submarine Landslide History [NanTroSLIDE]).

The most important accomplishments were (1) determination of heat flow at Sites C0011 and C0012, (2) coring through a transition in physical properties within the upper part of the Shikoku hemipelagite, (3) repeated coring and sampling of fluid above the sediment/basement interface for shore-based geochemical studies, (4) coring into the basalt to 100 m below the sediment/basalt interface, and (5) drilling and sampling a nearly complete slope basin stratigraphic succession comprising six mass transport deposits that record ~1 m.y. submarine landsliding history near the shallow megasplay fault zone area.

Introduction

The Center for Deep Earth Exploration (CDEX) accomplished three Nankai Trough Seismogenic Zone Experiment (NanTroSEIZE) expeditions during 2010 and early 2011: Integrated Ocean Drilling Program (IODP) Expedition 326 (NanTroSEIZE Stage 3: plate boundary deep riser: top hole engineering), Expedition 332 (NanTroSEIZE Stage 2: riserless observatory), and Expedition 333 (NanTroSEIZE Stage 2: subduction inputs 2 and heat flow).

The objectives for Expedition 333 were to core and measure temperature within the shallow intervals at IODP Sites C0011 and C0012 that were not sampled during IODP Expedition 322 and to collect up to 220 m of additional basement material from Site C0012 (Fig. F1). These are the two subduction inputs sites for the Kumano transect, positioned above and on the northwest flank of a prominent basement high in the Shikoku Basin. Additionally, the coring objectives of an Ancillary Project Letter (738-APL), Nankai Trough Submarine Landslide History (NanTroSLIDE), were attempted to correlate the history of submarine landslides along the lower forearc slope to the history of slip along the megasplay fault.

Overview of the NanTroSEIZE complex drilling project

Subduction zones account for 90% of global seismic moment release, generating damaging earthquakes and tsunamis with potential disastrous effects on heavily populated areas (e.g., Lay et al., 2005). Understanding the processes that govern the strength, nature, and distribution of slip along these plate boundary fault systems is crucial for evaluating earthquake and tsunami hazards. Sediment-dominated subduction zones such as the Eastern Aleutian, Cascadia, Sumatra, and Nankai margins are characterized by repeated great earthquakes of magnitude $M \sim 8.0+$ (Ruff and Kanamori, 1983). Although the causative mechanisms are not well understood (e.g., Byrne et al., 1988; Moore and Saffer, 2001; Saffer and Marone, 2003), the updip limit of the seismogenic zones at these margins is thought to correlate with a topographic break, often associated with the outer rise of the forearc (e.g., Byrne et al., 1988; Wang and Hu, 2006). At Nankai, seismic reflection profiles across the forearc outer rise document an out-of-sequence thrust (OOST) fault system (the megasplay fault) that branches from the plate boundary décollement close to the updip limit of inferred coseismic rupture of the 1944 Tonankai $M 8.2$ earthquake (Moore et al., 2007) (Fig. F2).

The NanTroSEIZE project is a complex drilling project (CDP): a multiexpedition, multistage component of IODP focused on understanding the mechanics of seismogenics and rupture propagation along subduction plate boundary faults. NanTroSEIZE is a coordinated effort to sample and instrument the plate boundary system at several locations offshore the Kii Peninsula, Japan (Tobin and Kinoshita, 2006b). The main objectives are to understand

- The mechanisms and properties governing the updip aseismic–seismic transition of the megathrust and plate interface fault systems;

- Processes of earthquake and tsunami generation, as well as strain accumulation and release; and
- The mechanical strength and hydrogeologic behavior of the plate boundary fault and megasplay.

The following hypotheses are paraphrased from the original IODP proposals and outlined in Tobin and Kinoshita (2006a, 2006b):

1. Systematic, progressive material and state changes control the onset of seismogenic behavior on subduction thrust faults.
2. Subduction megathrusts are weak faults.
3. Plate motion is accommodated primarily by coseismic slip in a concentrated zone (i.e., the fault is locked during the interseismic period).
4. Physical properties of the plate boundary system (including the fault system and its hanging wall and footwall) change with time during the earthquake cycle.
5. A significant, laterally extensive upper plate fault system (the megasplay) slips in discrete events that may include tsunamigenic slip during great earthquakes. It remains locked during the interseismic period and accumulates strain.

To address Hypothesis 1 above, it is essential to document the composition and geo-technical/frictional/hydrogeological properties of the subduction inputs (i.e., the initial conditions) before the igneous rocks and sedimentary strata reach the deformation front and begin to change. As stated in Hypothesis 5 above, two of the first-order goals in characterizing the seismogenic zone along the Nankai Trough are to document the role of the megasplay fault in accommodating plate motion (both seismically and interseismically) and to characterize the fault's mechanical and hydrological behavior. This research bears on understanding both fault behavior and tsunami hazards.

Presently, the NanTroSEIZE CDP encompasses 12 sites along a transect that extends from the northwest edge of the Shikoku Basin across the frontal thrust region, the mid-slope megasplay region, and into the Kumano Basin forearc region (Figs. [F1](#), [F2](#)). One of these sites (IODP Site C0002) currently includes a pilot hole for the planned deep riser drilling operations. The other sites targeted fault zones in the shallow, aseismic portions of the accretionary complex (Kinoshita, Tobin, Ashi, Kimura, Lallemand, Sreaton, Curewitz, Masago, Moe, and the Expedition 314/315/316 Scientists, 2009) and the subduction inputs (Underwood et al., 2010).

From late 2007 through early 2008, IODP Expeditions 314, 315, and 316 were carried out as a unified program known as NanTroSEIZE Stage 1. Expedition 314 was dedicated to downhole measurement of physical properties and borehole imaging through logging while drilling (LWD). Expedition 315 was devoted to core sampling and downhole temperature measurement at two sites in the hanging wall: IODP Site C0001 just seaward of the outer rise and Site C0002 in the Kumano Basin. Expedition 316 targeted the frontal thrust region and megasplay in their shallow aseismic portions: IODP Site C0004 near the surface expression of the megasplay in the Kumano Basin, IODP Sites C0006 and C0007 at the frontal thrust of the accretionary wedge, and IODP Site C0008 in a trench-slope basin seaward of the splay fault. For more details, see Kinoshita, Tobin, Ashi, Kimura, Lallemand, Screatton, Curewitz, Masago, Moe, and the Expedition 314/315/316 Scientists (2009).

IODP Expeditions 319 and 322 followed in 2009, as NanTroSEIZE Stage 2. Expedition 319 prepared boreholes at IODP Sites C0009 and C0010 for future installation of long-term monitoring systems. At Site C0009, Expedition 319 also conducted the first riser operation in IODP history, as well as a walkaway vertical seismic profile experiment (Saffer, McNeill, Byrne, Araki, Toczko, Eguchi, Takahashi, and the Expedition 319 Scientists, 2010). Expedition 322 cored Sites C0011 and C0012 in the Shikoku Basin to document the composition and material properties of sediment and uppermost igneous basement that eventually enters the Nankai subduction zone. Expedition 332 in 2011 further succeeded by placing new system at Site C0010 after retrieving data over a 15 month period and installing a permanent observatory system at Site C0002 (Kopf et al., 2011).

Background

Geological setting

The Nankai Trough is a convergent plate boundary where the Philippine Sea plate underthrusts the southwestern Japan margin at rates of 4.0–6.0 cm/y along an azimuth of 300°–315°N (Seno et al., 1993; Miyazaki and Heki, 2001; Mazzotti et al., 2000; Henry et al., 2001) down an interface dipping 3°–7° (Kodaira et al., 2000a). The subducting lithosphere of the Shikoku Basin was formed by backarc spreading during a time period of approximately 15–25 Ma (Okino et al., 1994).

The three major seismic stratigraphic sequences identified in the northern Shikoku Basin are the lower and upper Shikoku Basin facies and local spillover of Quaternary

trench-wedge turbidites. The upper Shikoku Basin facies seismic off the Kumano Basin transect area thins toward the north, whereas the lower seismic succession has a more complicated isopach geometry strongly influenced by basement topography (Le Pichon et al., 1987a, 1987b; Mazzotti et al., 2002; Moore, Taira, Klaus, et al., 2001; Moore et al., 2001; Ike et al., 2008b). Throughout the basin, seismic thickness decreases above large basement highs and the inferred sand-rich packages of the lower Shikoku Basin pinch out against or lap into basement highs. Basement highs are imaged within the subduction zone (Kodaira et al., 2003, Dessa et al., 2004) where they influence margin structure (Lallemand et al., 1992; Le Pichon et al., 1996; Park et al., 1999; Mazzotti et al., 2002; Bangs et al., 2006; Moore et al., 2009) and seismicity (Kodaira et al., 2000b; Park et al., 2004). The mechanical and hydrogeological differences between strata above subducting basement highs and regions with smooth basement topography could be significant for modulating fault zone dynamics and earthquake rupture behavior.

The lower forearc slope of the Nankai Trough consists of a series of thrust faults that have shortened the accreted sedimentary units of the prism (e.g., Moore et al., 2009; Screamon et al., 2009). Swath bathymetry and multichannel seismic (MCS) data show a pronounced and continuous outer arc high extending >120 km along strike, which may be related to slip on the megasplay fault (Moore et al., 2009; Martin et al., 2010). The outer arc high coincides with the updip end of the splaying system of thrust faults that branch from a strong seismic reflector interpreted by Park et al. (2002) as a major OOST. The megasplay fault is hypothesized to represent the mechanical boundary between the inner and outer accretionary wedge and between aseismic and seismogenic fault behavior (Wang and Hu, 2006). At depth, this megasplay produces a high-amplitude reflector (Fig. F2). It branches into a family of thrust splays in the upper few kilometers below the seafloor, including the thrust splay drilled during Stage 1 Expeditions 314, 315, and 316 (Moore et al., 2007, 2009).

The plate boundary, when traced in the downdip direction on seismic profiles, eventually ramps down from a sediment/sediment interface to the sediment/basalt or an intrabasalt interface (Park et al., 2002). This shift in lithologic position of the fault must coincide with fundamental changes in the rock's mechanical and/or hydrologic properties, but how so? Shore-based studies indicate that systematic fragmentation of upper basement and incorporation of basalt slabs into shear-zone mélanges could be controlled by primary layering of the igneous rock (Kimura and Ludden, 1995). By coring additional basement rocks seaward of the trench, we hope to discriminate between the presubduction features in basement inherited from backarc spreading in

the Shikoku Basin and the changes imparted by increasing pressure-temperature (P-T) conditions and stress at depth (documented in the future by deep riser drilling).

Previous drilling achievements

Sites C0011 and C0012

Expedition 322 was designed to document characteristics of incoming sedimentary strata and uppermost igneous basement prior to their arrival at the subduction front (Saito et al., 2009). To accomplish those objectives, coring was conducted at two sites on the subducting Philippine Sea plate. Site C0011 is located on the northwest flank of a prominent bathymetric high (the Kashinosaki Knoll; Ike et al., 2008a), whereas Site C0012 is located near the crest of the knoll (Fig. F2).

The resulting data, which include LWD during Expedition 319, provide a great deal of new information on presubduction equivalents of the seismogenic zone (Underwood et al., 2010). Core samples at Site C0011 were obtained by rotary core barrel (RCB) drilling from 340 to 876 m core depth below seafloor (CSF) where the hole was abandoned because of failure of the drill bit. After jetting-in to ~70 meters below seafloor (mbsf), RCB coring at Site C0012 penetrated almost 23 m into igneous basement and recovered the sediment/basalt interface intact at 537.81 m CSF. This incomplete coring program left major gaps in the stratigraphic coverage, particularly within intervals of the upper Shikoku Basin facies. Core quality and core recovery were also poor, which compromised the scientific outcomes. Nevertheless, the merger of lithofacies and age-depth models shows how correlative units change from an expanded section at Site C0011 to a condensed section at Site C0012. The composite section also captures most of the important ingredients of basin evolution, including a previously unrecognized interval of late Miocene volcanoclastic sandstone designated the middle Shikoku Basin facies. An older (early–middle Miocene) turbidite sandstone/siltstone facies with mixed volcanoclastic-siliciclastic detrital provenance occurs in the lower Shikoku Basin; this unit may be broadly correlative with superficially similar Miocene turbidites on the western side of the basin (Underwood, 2007). The age of basal sediment (reddish-brown pelagic claystone) at Site C0012 is older than 18.9 Ma.

Geochemical analyses of pore fluids on top of the basement high show clear evidence of upward diffusion of sulfate and other dissolved chemical species from the basement (Underwood et al., 2010). The depth of the sulfate reduction zone is also anomalously deep at Site C0012. Chlorinity values increase toward basement because of hydration reactions in the sediment and diffusional exchange with basement fluids.

In contrast to Site C0011, where chlorinity decreases with depth, the more saline fluids at Site C0012 are largely unchanged by the effects of focused flow and/or in situ dehydration reactions associated with rapid burial beneath the trench wedge and frontal accretionary prism. Thus, Site C0012 finally provides a reliable geochemical reference site, unaffected by subduction processes.

Seismic studies/site survey data

Site survey data have been collected in the drilling area over many years, including multiple generations of 2-D seismic reflection (e.g., Park et al., 2002), wide-angle refraction (Nakanishi et al., 2002), passive seismicity (e.g., Obana et al., 2004; Obara and Ito, 2005; Ito and Obara, 2006), heat flow (Yamano et al., 2003), side-scan sonar, swath bathymetry, and visual observations from submersible and remotely operated vehicle (ROV) dives (Ashi et al., 2002). In 2006, Japan and the United States conducted a joint 3-D seismic reflection survey over a ~11 km × 55 km area, acquired by PGS Geophysical, an industry service company (Moore et al., 2007). This 3-D data volume was used to refine selection of drill sites and targets in the complicated megasplay fault region, define the regional structure and seismic stratigraphy, analyze physical properties of the subsurface through seismic attribute studies in order to extend information away from boreholes, and assess drilling safety (Moore et al., 2009). A smaller 3-D survey was conducted over proposed Sites NT1-01A (C0012) and NT1-07A (C0011) in 2006 by the Japan Agency for Marine-Earth Science and Technology-Institute for Research on Earth Evolution (JAMSTEC-IFREE) (Park et al., 2008). Prestack depth migration of those data led to refined velocity models and revised estimates of sediment thickness and total drilling depths.

Sites C0011 and C0012

Scientific objectives

As mentioned previously, the upper stratigraphic intervals (upper Shikoku Basin facies) were not adequately sampled during Expedition 322. Therefore, one of the priorities for Expedition 333 was to fill in the coring gaps and expand the age-depth models into the Pliocene and Quaternary. The shallow section is also important for comprehensive profiles of organic and interstitial water geochemistry. Thermal structure, including the effects of fluid circulation in the basement, is another of the critical input variables to document because of its influence on sediment diagenesis and

fluid chemistry (Spinelli and Underwood, 2005; Saffer and McKiernan, 2009; Spinelli and Wang, 2008). The age of subducting lithosphere within the Kumano transect area is ~20 Ma (Okino et al., 1994), as verified by coring at Site C0012 (Underwood et al., 2010). The Kashinosaki Knoll lies west of the Zenisu Ridge intraoceanic thrust, which brings backarc basin crust to crop out at the seafloor further to the east (Lallemant et al., 1989; Henry et al., 1997). However, the respective contributions of active compressive tectonics and seamount volcanism to the Kashinosaki Knoll morphology are unclear, and the exact timing of volcanic activity responsible for the birth of the Kashinosaki Knoll (Ike et al., 2008) still needs to be established by radiometric dating of the basalt. Dense near-surface heat flow measurements around the Kashinosaki Knoll indicate significantly higher value than the theoretical value estimated from the age of the Shikoku Basin (Kinoshita et al., 2008). Deeper thermal structure is required to document the entire heat flow pattern around the sites with high-quality borehole temperature measurement. As subduction carries Shikoku Basin strata toward and beneath the accretionary prism, we expect fluids and physical properties to change downsection and downdip in response to hydration reactions (e.g., volcanic glass to zeolite + smectite), dehydration reactions (e.g., opal-to-quartz and smectite-to-illite), and crystalline cement precipitation (carbonates, zeolites, and silica). Documenting such changes is an essential ingredient of the NanTroSEIZE science plan. Sharp diagenetic fronts (especially opal-to-quartz) have been linked to anomalous offsets in profiles of porosity, *P*-wave velocity, and other geotechnical properties (Spinelli et al., 2007). LWD data from Site C0011 show offsets at ~250 m LWD depth below seafloor (LSF) that may be caused by this type of reaction (Underwood et al., 2010). Alteration of dispersed volcanic glass is also potentially important during diagenesis but, as yet, this component of the sediment budget is poorly understood (Scudder et al., 2009). Similarly, hydrous authigenic phases in the basalt (e.g., saponite from ridge-flank hydrothermal alteration) are susceptible to diagenetic reactions at higher temperatures. Updip migration of fluids (including hydrocarbons) toward the Shikoku Basin from landward zones of deeper seated dehydration reactions is a distinct possibility (Saffer et al., 2008), and this idea can be tested through a comprehensive program of geochemical analyses. Interpretation of the geochemistry, however, requires constraints on the in situ temperature.

Characterization of basement composition and structure is a high priority for NanTroSEIZE. Permeability and fluid flow within oceanic basalt are affected by many variables (Fisher, 1998). A long-term goal is to monitor and sample fluids in the basement using subseafloor observatories, but design of those experiments hinges on coring and logging results. As a prelude, we planned to concentrate first on documenting the

basement's structural architecture, hydrologic properties, and early alteration products. Products of early alteration within the uppermost basalt (e.g., saponite and calcite) change the rock's bulk chemistry and physical properties (porosity and permeability). The extent of this alteration is important for constraining the volatile content of subducting crust. In addition, coring at least 100 m into basement and wireline logging during a future expedition will capture heterogeneities in fracture patterns and porosity that might be involved in delamination of the basalt downdip in the seismogenic zone.

The specific set of questions addressed by additional drilling at input sites are

- Is fluid circulation in basement and permeable sedimentary layers influencing heat flow and diagenesis at Sites C0011 and C0012?
- How does contrasting interstitial fluid chemistry at Sites C0011 and C0012 relate with in situ diagenesis and fluid flow?
- Can a change of physical properties between 200 and 250 mbsf at Site C0011 be related to lithologic variation or silica diagenesis? Does the same transition occur at Site C0012?
- Was magmatic activity heterogeneous in composition and age on the backarc basin basement high (Kashinosaki Knoll)?
- Is alteration of the upper oceanic basement heterogeneous and how does such alteration influence geochemical and fluid budgets?

NanTroSLIDE Ancillary Project Letter

Scientific objectives

Expedition 333 drilled and sampled the slope basin seaward of the megasplay that is characterized in 3-D seismic data by stacked mass transport deposits (MTDs) (Strasser et al., 2011) (Fig. F3). The aim of the coring was to establish the submarine landslide history and reconstruct transport dynamics. Core from Site C0018 (proposed Site NTS-1A) was to be integrated with 3-D seismic interpretation and data from nearby NanTroSEIZE sites to determine the relation of submarine landslides to tectonic evolution. By establishing a better physical understanding of tectonic processes and slope failures, we planned to also gain a general understanding of failure-related sedimentation patterns and the significance of episodic mass transport events. Ulti-

mately, this could help us assess the tsunamigenic potential of tectonic landslides. The primary goals of drilling Site C0018 were

1. To establish a well-dated Quaternary mass-movement event stratigraphy and
2. To sample the distal part of an exceptionally thick MTD for analyzing its rheological behavior to constrain sliding dynamics and tsunamigenic potential.

These aim at providing answers to the following questions:

1. What is the frequency of submarine landslides?
2. What is the source materials of the MTDs?
3. What is the importance of accretionary wedge remobilization versus surficial processes?
4. What controls type, size, and magnitude of turbidites and MTDs and how do they change through time?
5. How do large MTDs relate to the timing of splay fault activity as inferred from NanTroSEIZE Stage 1 drilling (Strasser et al., 2009)?
6. What are the dynamics of large submarine landslides and can we infer their tsunamigenic potential?

By addressing these questions, we aimed to isolate tectonic processes influencing magnitude and occurrence of submarine landslides along active subduction zone margins and to understand their potential for triggering catastrophic events in terms of both hazards (tsunamigenic landslides) and sediment mass transfer within the context of margin evolution.

Drilling strategy

Site C0018 (proposed Site NTS-1A) (water depth = 3100 m) is located on a margin-perpendicular transect 4.5 km southwest of the NanTroSEIZE Stage 1 drilling transect (Fig. F1). It is located 5 km south-southwest of Site C0008, which was drilled into a small slope basin seaward of the megasplay fault (Kinoshita, Tobin, Ashi, Kimura, Lallemant, Sreaton, Curewitz, Masago, Moe, and the Expedition 314/315/316 Scientists, 2009). Site C0008 results show the utility of using the ages of MTDs to reconstruct slope failure activity related to megasplay fault movements (Strasser et al., 2009). Apart from the deepest section, Site C0008 lacks clear evidence for MTDs because of a significant hiatus in its upper part, suggesting erosion related to a prominent slope collapse structure seaward of the megasplay fault (Strasser et al., 2011;

Conin et al., 2011). On the basis of new 3-D seismic data interpretation, the Ancillary Project Letter proponents have identified a lower slope basin that (1) better represents the depocenter for downslope mass transport, (2) is clearly characterized by stacked MTDs as seismically imaged by acoustically transparent to chaotic bodies with ponded geometries (Fig. F3), and (3) includes a large, as thick as 180 m, MTD. Expedition 333 drilled at a location where the MTD bodies wedge out and where basal erosion is minimal. Continuous coring with hydraulic piston coring system (HPCS) and extended shoe coring system (ESCS)/extended punch coring system (EPCS) to ~350 mbsf allowed sampling of the MTDs across the most complete and longest stratigraphic succession.

Principal results

Site C0018

The primary goals of drilling IODP Site C0018 were to establish a well-dated Quaternary mass-movement event stratigraphy and to sample the distal part of an exceptionally thick MTD for analyzing its rheological behavior to constrain sliding dynamics and tsunamigenic potential (Fig. F3). Identification of MTD intervals in cores relied on a combination of observations:

- *Indications for sediment remobilization and internal deformation during mass transport:* Evidence for sediment remobilization includes convolute strata, chaotic and brecciated facies, mud pebbles, absence of bioturbation, and mixed sediments of different grain sizes. Deformation styles can be highly variable, and parts that only experienced moderate plastic deformation concentrated to restricted zones may contain intervals of coherently bedded sediments. Dipping beds, small folds, and faults are common occurrences in these parts. However, assessment of bedding dips and fault orientation is needed to distinguish deformation attributable to slope instability from postdepositional tectonic deformation, which could result from strain in the underlying accretionary wedge. Paleomagnetism (i.e., for HPCS coring: dispersed paleomagnetic declination and inclination) can provide additional arguments to recognize zones of sediment perturbation, notably in the absence of bedding. Contrasts of physical properties and physical composition may also help define the boundaries between intact and remobilized sediments.
- *Upper boundary/contact:* The upper contact surface of MTDs may be identified from the presence of a boundary between undisturbed subhorizontal and bioturbated sediment above and disturbed sediments below, without evidence for shearing. A

turbidite, originating from erosion resulting from viscous drag of the frontal part of the moving mass, as has been shown experimentally, could be a marker associated with the larger events (Lee et al., 2004; Solheim et al., 2005).

- *Lower boundary/contact of MTDs:* The lower contact may appear as an erosional boundary between flowed and/or sheared sediments above and flat-lying sediments below. However, deformation could also occur in the underlying sediments as a consequence of shear during flow and/or postdepositional loading (e.g., Schnellmann et al., 2005; Frey-Martínez et al., 2006; Alves and Lourenço, 2010). The lower contact may also appear as subhorizontal shear zone. A shear zone in the context of the Nankai accretionary wedge can be of tectonic origin, and, when related to gravity sliding, is not necessarily tied to a single event. Multiple shear zones can also result from nonuniform strain distribution within the MTD. However, structural relationships and stratigraphy may lead to propose a shear zone as forming the base of an MTD.
- *Biostratigraphy and chronology:* Age constraints, as inferred from biostratigraphy, magnetostratigraphy, tephrostratigraphy, and (postcruise) isotope stratigraphy, can resolve conformable MTD-overlying and MTD-underlying strata and/or age gaps, as well as the possible admixture of older nannofossil and/or plankton assemblages within MTDs. The age of the hemipelagic/pelagic sediments deposited immediately above the MTD can define the minimum age of the underlying landslide, considering the slide as one single, discrete event. The base of a MTD may, however, have a different significance depending on where observations are performed. In the distal downslope part of the MTD, the base may represent a depositional surface, on which the remobilized material ceased downslope movement. In this case, the sediment immediately below the MTD can have a similar or only slightly older age as remobilized strata immediately above. In more proximal parts, however, basal erosion is likely a frequent process that can result in a hiatus. In the source region, the base of the slide is presumably a zone of concentrated shear that may not necessarily be described as a single plane.

Operations

After recovering transponders by ROV, the *Chikyu* left Hole C0002G at 0300 h on 10 December 2010. After 8 nmi of transit with an average speed of 4 kt, the *Chikyu* arrived at the first transponder location for Site C0018 at 0500 h. Deployment of four transponders and calibration finished at 2045 h and we began preparation for HPCS/EPCS/ESCS coring. The 11 $\frac{1}{16}$ inch HPCS/EPCS/ESCS bottom-hole assembly (BHA) was run into Hole C0018A at 1445 h on 11 December. Coring began at 0115 h on 12 De-

ceMBER and continued to the 36th core, and we decided to finish at 314.15 mbsf at 2103 h on 16 December (Table T1). Operational problems were few and minor during the course of 4 days of coring. Those included damage to a seal in the inner barrel, failures on shooting, and a broken lower part of the sinker bar assembly. After recovering the inner barrel and sinker bar assembly, we spotted kill mud, displaced the hole with seawater, and pulled out of the hole. The bit was back on the rig floor at 0500 h on 17 December.

Core recovery was excellent for piston coring with HPCS to 153.85 m drilling depth below seafloor (DSF) (Core 333-C0018A-17H), but core liner collapse or expansion in the core barrel caused problems for several cores (Cores 333-C0018A-9H and 16H were damaged). After experiencing repeated incomplete penetration and reaching the estimated MTD bottom, the coring system was shifted to EPCS at 190.65 m DSF (Core 333-C0018A-24T). EPCS recovery was variable, ranging from 90.7% to 0% with average recovery of 47.2%, as attempts to adjust the penetration of the EPCS cutting shoe ahead of the drill bit met with mixed success. We switched to ESCS after the seventh core. ESCS core recovery was surprisingly better than expected with good recovery ranging 70.8% to 114.9% with average recovery of 87.35%.

Both EPCS and ESCS were used below the MTD (EPCS from 190.65 m DSF and ESCS from 257.15 m DSF), and core quality assessment from X-ray computed tomography (CT) scans showed no major difference between EPCS and ESCS cores. Both systems formed fractured biscuits 2–4 cm thick. However, the ESCS cores appear to contain more slurry. Once split, degradation between EPCS and ESCS is obvious, as the thickness of shear zones between biscuits and core liner increases. With ESCS cores, it would be very difficult to identify small MTDs, as some were present in the formation below 257.15 m DSF. Some cores, including HPCS, were also strongly affected by gas expansion, resulting in voids and bubbly slurry intervals.

Overview

Slope sediments cored in Hole C0018A are divided into two lithologic subunits. Lithologic Subunit IA is primarily composed of hemipelagic mud (or silty clay) with interbedded volcanic ash layers and is affected by MTDs (Fig. F4). Lithologic Subunit IB is a sandy turbidite sequence. Two thick ash layers were correlated on the basis of superficial appearance with onland tephra deposits (Azuki and Pink) that originated from Kyushu volcanoes (Hayashida et al., 1996). The Pink ash layer, dated on land as 0.9–1.05 Ma, lies at 183.8–190.65 m CSF, close the base of Subunit IA and the base of the thick MTD. The Azuki ash layer, dated on land as 850,000–900,000 y, is found at

125.65–126.45 m CSF, <1 m above the top of the thick MTD. These correlative ages were used to constrain magnetostratigraphy and are compatible with preliminary micropaleontological data.

Six intervals with evidence for MTDs are observed within Subunit IA and numbered from top to bottom for convenience (Fig. F4). The upper boundary/contact is well defined for MTDs 1, 2, and 6 and is marked by a turbidite for two of them (MTDs 2 and 6) (Fig. F5). MTD 1 extends over 2.9 m of chaotic and convolute bedding in Core 333-C0018A-1H. MTD 2 comprises in its lower part several intervals of coherent bedding limited by probable shear zones. The lowermost one defines the base of the MTD 2 interval (Fig. F6). MTD 3 comprises an interval with visual evidence for remobilization near its top, and examination of CT scan and structural data lead to considering this interval as part of a thicker MTD zone. MTD 4 is a relatively thin interval (50 cm) associated with a fluidized ash layer (Fig. F7). MTD 5 extends over cores that were also disturbed by the coring process. A zone of remobilization is identified based on visual evidence and CT scan in Core 333-C0018A-9H, although this core was damaged during extraction from the core barrel. Evidence for a shear zone with a sharp lower boundary on CT scan images defines the base of MTD 5; however, it is yet unclear whether this MTD interval corresponds to a single event deposit. MTD 6 is a 61.36 m interval between 127.55 and 188.57 m CSF and corresponds to the main MTD body identified in the seismic data. As already noted, a turbidite deposit is found immediately above its upper boundary. Chaotic and convolute bedding (Fig. F8) and mixing of ash with hemipelagite deposits are observed in the cores, but other intervals remain coherently bedded. Several shear zones are identified from CT scans in the lower part of MTD 6, but none could be positively identified as the basal surface. The base of the thick MTD was thus defined at the top of the Pink ash layer.

Important findings are a correlation of MTD occurrence with a change in sedimentation from turbidite to hemipelagite dominated and the presence of a thick ash layer at or near the base of the thick MTD. Whereas the presence of a thick ash layer at, or near, the lithologic boundary is likely coincidental, the peculiar stratigraphic context of the thick MTD suggests that sediment properties, and their variations, have a major influence on MTD occurrence and size.

Lithology

Hole C0018A was entirely drilled in a slope basin pile/stratigraphic succession. Slope deposits overlying the accretionary wedge were defined as lithologic Unit I in previous expedition reports. In Hole C0018A, a marked difference was observed in cores

between a dominantly hemipelagic section bearing ash layers, volcanoclastic sands, occasional siliclastic turbidites and intercalated MTDs forming Subunit IA (above 190.65 m CSF), and a sequence of sandy turbidites forming Subunit IB and interpreted as a sand-rich slope basin (Fig. F9). These subunits correlate with seismic Units 1a and 1b of Kimura et al. (2011). Within Subunit IA, the interval between 24.04 and 57.51 m CSF contains more abundant silty and sandy turbidites than intervals above and below. Three facies (IAi, IAii, and IAiii) are thus defined within Subunit IA. Turbidites in Facies IAii are dominantly of volcanoclastic origin. Conversely, samples with relatively higher plagioclase content, lower quartz content, and higher clay content in Facies IAii reflect an altered ash component (Fig. F10). Sequences of thin (~5 cm), silty to very fine sand turbidites are also found above ash layers in the lower part of Facies IAiii. Sands in Subunit IB have a mixed composition with quartz, plagioclase, and abundant lithic fragments of both metamorphic and volcanic origin, and thus are not considered to be volcanoclastic sands. An increase in quartz content and in the variability of mineral composition from Subunits IA to IB is observed in the X-ray diffraction (XRD) data (Fig. F10). Below 190.65 m CSF there is also a marked decrease in the relative abundance of nannofossils, diatoms, and spicules. Calcite content from bulk powder XRD, calcium content from X-ray fluorescence (XRF) (Fig. F11), and carbonate content from coulometric analysis are consistently higher in Subunit IA than in Subunit IB and tend to increase uphole within Subunit IA. This may be interpreted as a consequence of uplift above the carbonate compensation depth (Strasser et al., 2009)

Two remarkably coarse-grained ash layers occur within Unit I and are attributed to cataclysmic eruptions in Kyushu, known from widespread tephra deposits on land. A normally coarse (sand-sized) ash 80 cm thick is found at 125.65–126.45 m CSF and interpreted as the Azuki event, dated on land as 850.000–900.000 y (Yoshikawa and Mitamura, 1999) (Fig. F7). A dark sand-sized to fine ash layer, which was fluidized upon coring, is found at 183.8–190.65 m CSF. Deposits from this event are characterized by abundant plate-shaped volcanic glass particles interpreted as bubble wall shards. Our provisional correlation is with the Pink event, dated on land as 0.99–1.05 Ma (Yoshikawa and Mitamura, 1999) (Fig. F7). The Subunit IA/IB boundary lies below this ash layer.

Structural geology

Structural features of Site C0018 mainly record gravity-driven deformation and mass-movement processes. The main structural features from visual core description at this site are subhorizontal and southeast-dipping beds and northward- and southward-

dipping normal faults, outside MTD intervals in the upper part of the borehole (0–127.26 m CSF); scattered bedding dips, fault zones, and flow structures within the thick MTD (127.55–188.57 m CSF); and subhorizontal beds and fissility below the thick MTD (188.62–313.655 m CSF) (Figs. [F12](#), [F13](#)). A remarkable overturned fold was also observed within MTD 2 at 41.2 m CSF (Fig. [F14](#)). CT scans may provide additional evidence for shearing. Lines with very high CT values (3000 or more) were identified as early diagenetic pyrite, which may constitute a marker of ductile deformation. Furthermore, small faults and thin shear bands (<3 mm) associated with MTDs appear generally denser on CT scan images (Fig. [F15](#)), although still in the usual range for high-porosity sediment (<1500). Several intervals with pyrite mineralizations organized as lineations and bearing low-angle planar discontinuities with associated increased CT values are tentatively interpreted as shear zones (e.g., Fig. [F7](#)).

Biostratigraphy

Preliminary biostratigraphic determination for Site C0018 was based on examination of calcareous nannofossils. All core catcher samples and additional samples from sections were examined. Several nannofossil events were recognized with mostly good preservation. Although some reworked specimens were identified in the examined intervals, most specimens can be considered in situ. The result shows no significant time gap in Hole C0018A. The lowest core catcher at 313.61 m CSF indicates an age younger than 1.67 Ma. Ages derived from nannofossil events suggest a slower sedimentation rate (~6 cm/k.y.) in the interval of 0–25.525 m CSF corresponding to Facies IA_i and a higher apparent sedimentation rate (~23 cm/k.y.) in the interval of 25.53–313.61 m CSF. This interval includes most MTDs within Subunit IA as well as Subunit IB, which is composed of sandy turbidites.

Paleomagnetism

Shipboard paleomagnetic studies for Site C0018 were performed with remanent magnetization and magnetic susceptibility measurements of discrete samples. Recovered sediments showed considerable variation in magnetic properties and demagnetization behavior. The natural remanent magnetization (NRM) intensities span more than two orders of magnitude, and variations in magnetic susceptibility are consistent with the variations in NRM intensity. Remagnetization imparted by the coring process is commonly encountered and is characterized by NRM inclinations that are strongly biased toward vertical (mostly toward +90°) in a majority of cores. Alternating-field (AF) demagnetization to 30 mT effectively removed this drilling-induced remagnetization, as observed by a significant decrease in intensity and a shift of

inclination toward shallower or negative values for intervals with normal or reversed polarity, respectively. Magnetostratigraphy is determined based on the inclination data demagnetized at 30 mT. The most diagnostic feature in the paleomagnetic polarity is a change from normal to reversed polarity within Core 333-C0018A-14H, which corresponds to the Brunhes/Matuyama Chron boundary (0.78 Ma). According to tephra chronological data, the base of a normal chron below the thick MTD horizon is correlated to the base of Jaramillo Subchron (1.07 Ma). Cores recovered with HPCS generally show a clustered distribution in declination within each core, but the declinations in the MTD intervals are scattered. This supports irregular rotation of sediments in MTDs.

Physical properties

From the surface to ~200 m CSF, bulk density generally increases and porosity decreases downhole, accompanied by increasing penetration and shear strength, thermal conductivity, and resistivity (Fig. F16). Porosity and resistivity are generally correlated and, arguably, MTD intervals display an increased compaction gradient compared with the average porosity-depth trend, and slight reversals (porosity increasing with depth) are observed near the base of MTDs 2, 3, 5, and 6. For the latter case (MTD 6), this could be in part related to the lithologic change between Subunits IA and IB. Shear strength displays more scatter within MTD intervals. Within the thick MTD, all physical property values (porosity, thermal conductivity, strength, and resistivity) show greater scatter than above or below. A drop in shear strength below the thick MTD at ~190 m CSF may at least in part be an artifact related to the change of coring system from HPCS to EPCS, and then ESCS. Below 200 m CSF, physical properties show no distinct trend.

Inorganic geochemistry

The main geochemical objectives at this site were to document the variations in chemical composition of the interstitial water. Whole-round lengths ranged from 20 to 31.5 cm, and interstitial water volumes per centimeter of core ranged from 1.95 to 2.15 mL/cm between 0 and 130.5 m CSF (Fig. F17). Because of the consolidated nature of the formation in the deeper portion of this site and the coring techniques used, some of the deeper cores were quite disturbed. Sulfate concentration, calcium concentration, and alkalinity point to a sharp methane-sulfate reaction zone at ~15 m CSF. Below this level, we could use the sulfate concentration to identify and quantify contamination. Chlorinity increases rapidly in the upper ~30 m of Hole C0018A and then gradually increases with depth (Fig. F18). The gradual increase in chlorinity in Hole

C0018A may reflect ash alteration, which consumes water. The distribution of major and minor cations documents extensive alteration of volcanogenic sediments as well (Fig. F19). The thick MTD interval is associated with lower phosphate concentration. This feature is not explained.

Organic geochemistry

Methane is the predominant hydrocarbon component in most cores and ranges between 0 and 19,339 ppmv (Fig. F20). Ethane is either below detection or present in low concentrations (i.e., <2 ppmv). No heavier hydrocarbon gases were detected. All C_1/C_2 ratios are >4000, suggesting that methane is biogenic and organic matter is immature. Calcium carbonate ($CaCO_3$) contents average at 12.5 wt% and vary in a wide range (0.2–25.4 wt%) (Fig. F21). Total organic carbon (TOC), total nitrogen (TN), and total sulfur (TS) contents are low in the majority of cores, averaging 0.58 ± 0.16 , 0.07 ± 0.02 , and 0.21 ± 0.19 wt%, respectively. Parameters including $CaCO_3$, TOC, TN, and TS contents all show larger variations in the upper ~87 m CSF and become less variable in deeper sediments. The atomic ratios of TOC to TN (TOC/TN_{at}) fall in the range of ~3.5–15, suggesting organic matter is mostly derived from marine sources but also contains terrestrial material in some horizons.

Core-seismic integration

At Site C0018, the base of the thick MTD (MTD 6) appears very reflective in profiles from 3-D seismic data and of negative polarity. This could be related to a step increase of porosity observed at the base of the thick MTD (Fig. F16). It is unclear whether the change of physical properties observed at this level is the consequence of deformation within the MTD or of a change of lithology at the transition between lithologic Subunits IA and IB, or both. Seismic onlap surfaces above MTD 6 define the base of several suspected MTDs in seismic data. These correlate with intervals in cores with evidence for remobilization (MTDs 2, 4, and 5) (Fig. F22). The layered sequence below the thick MTD corresponds to lithologic Subunit IB, which is composed of turbidites, but these reflectors cannot be interpreted as individual events in the turbidite sequence.

Downhole temperature measurements

During HPCS operations, downhole temperature was measured with the advanced piston corer temperature tool (APCT-3) at ~30 m intervals. Starting from 35.15 m DSF, six data points were obtained to 190.65 mbsf, but the deepest measurements at 161.65 m DSF and 190.65 mbsf may be unreliable. Other data follow a nearly linear

increase in temperature with depth ($0.0581^{\circ}\text{C}/\text{m}$) (Fig. F23). Heat flow, which was calculated by taking into account thermal conductivity measured on cores, is $62 \text{ mW}/\text{m}^2$.

Site C0011

The main reasons for returning to Site C0011 were to perform temperature measurements for heat flow determination and expand the age-depth models into the Pliocene and Quaternary. This was necessary because as the upper stratigraphic intervals (upper Shikoku Basin facies) were not adequately sampled during Expedition 322. The additional coring provides complete profiles of organic and interstitial water geochemistry, and samples across prominent discontinuities in physical properties identified on LWD data. Site C0011 is located on the northern flank of the Kashinosaki Knoll (Fig. F24, F25).

Operations

Transponders were retrieved from 0600 to 1530 h on 17 December 2010. The *Chikyu* then moved to Site C0011's first transponder location over a 22 nmi distance at an average speed of 5.5 kt. The ship began setting transponders at 1930 h and finished at 0700 h on December 18.

The HPCS/EPCS/ESCS coring assembly was made up, run into Hole C0011C, and tagged the seafloor at 1700 h; coring began at 1800 h on 18 December. After oil leakage from the HPCS was found, the decision was made to pull out to 13 m above the seafloor, and coring in Hole C0011C ended at 22.5 mbsf. From 0015 h on 19 December, the BHA was jetted in Hole C0011D to 6 mbsf and drilled in to 21 mbsf before starting HPCS coring again at 0245 h. Coring continued to 184.5 m DSF where the decision was made to switch to EPCS because of the continuous partial penetrations. However, EPCS coring did not bring good quality and recovery cores, and we switched to the ESCS after three cores at 1200 h on 21 December. After reaching 380 mbsf, which is 30 m deeper than the target depth, coring was stopped at 0900 h on 24 December, and we spotted the kill mud and displaced same with seawater before pulling out. Core bit and all assembly were on rig floor at 2000 h.

Coring operations were smooth except for oil leakage from the HPCS, which forced us to end Hole C0011C at a very shallow depth. Core recovery was good with an overall average of 101.7% in Hole C0011C and 102.2% in Hole C0011D. HPCS cores were the best of the three different core types in terms of both recovery and quality, with an average recovery of 102.4%, ranging from 117.3% to 82.8%. EPCS did not get good

core recovery, ranging from 77.2% to 38.6%. ESCS cores were good in recovery with an average of 103.3%, ranging from 158.6% to 9.3%, and remarkably good cores were obtained in the weakly cemented tuffaceous sandstone, an improvement over Expedition 322 RCB coring. There were two incidents of core liner broken, and core jammed once.

Lithology

A total of 380 m of strata was drilled in Holes C0011C and C0011D (Fig. F26). Two lithologic units were identified with very good recovery rates. Unit I corresponds to Shikoku Basin hemipelagites and Unit II corresponds to middle Shikoku Basin volcanic sand facies (Underwood et al., 2010). In addition, two lithologic subunits were interpreted within Unit I, Subunit IA (youngest), and Subunit IB. Cored lithologies include silty clay, clay, and mudstone interbedded with coarse to fine volcanic ash (Fig. F26). The Subunit IA/IB boundary occurs at 251.56 m core depth below seafloor, Method B (CSF-B) and is defined by the appearance (below) of harder dark gray mud and mudstone with abundant bioturbation and by the disappearance of volcanic ash layers with unaltered glass. A more dramatic lithologic change occurs below 347.82 m CSF-B where we found an abrupt shift into coarser-grained tuffaceous sandstone and heterolithic gravel and sand. This change marks the Unit I/II boundary. Unit I was not cored during Expedition 322.

Subunit IA comprises a 251 m thick succession of greenish gray silty clay with minor amounts of grayish silty clay and <50 cm intercalations of volcanic ash, often bearing unaltered glass shards. Bioturbation is particularly observed in the upper part of the unit. The genera *Zoophycos* and *Chondrites* burrows are abundant. Overall, ash layers are more abundant in the upper half of the subunit to ~100 m CSF-B (Fig. F26). In addition, XRD data from the dominant silty clay lithology indicate an average content of 57% clay minerals, 18% quartz and plagioclase, and 7% calcite for the subunit. However, both variations in the relative percentage of calcite are recorded at specific intervals with a maximum in calcite abundance of 26% at 3.16 m CSF-B (Fig. F27). Although uncommon, siliceous fossils (diatoms, radiolarians, and sponge spicules) are present in Subunit IA. The dominant lithology of Subunit IB is a greenish brown to dark gray weakly lithified mudstone with minor contribution of altered volcanic ash beds (Fig. F26). Clay minerals and altered volcanic glass are the most abundant particles on smear slides and an increase in the severity of glass alteration as depth increases is observed below the transition from Subunit IA to IB (Fig. F28). Clay content from XRD data averages 67% for the mudstone, ranging from 74% to 46% (Fig. F27). Quartz content ranges from 12% to 19% and averages 17%, and plagioclase

ranges from 9% to 18% and averages 12%. Calcite is present in the subunit, varying from 0% to 31% (Figs. F27) and reaching a maximum near the transition from Subunit IA to IB. Siliceous microfossils are absent from smear slides (with one exception) in Subunit IB.

The upper part of Unit II is dominated by coarser-grained tuffaceous sandstones and heterolithic gravel, gravelly sandstone, and sandstones with sharp and well-defined upper and lower boundaries (Fig. F29), similar to recoveries during Expedition 322. These beds are separated by indurated mudstone very similar to that of Subunit IB. The relative clay mineral abundance drops in association with a higher percentage of sandy material. From XRD data, the content of quartz is consistent at ~16%, whereas plagioclase values vary from 11% to 46%. Biotite, orthopyroxene, and hornblende are common in the tuffaceous sandstones (Fig. F26). Siliceous microfossils and fresh glass shards are found again in Unit II.

Four volcanic ash layers comprise stratigraphic markers at Site C0011. The first ash layer, which correlates with the Azuki volcanic ash layer on land (0.85 Ma; Hayashida et al., 1996), occurs at 21.77 m CSF-B (Fig. F29). The second ash layer, which the Pink ash correlates with (1.05 Ma; Hayashida et al., 1996), occurs at 31.32 m CSF-B. The correlative products of both events are preserved on land as thin discrete accumulations of ash. In addition, a bed correlative to the onland Ohta ash layer (4.0 Ma; Satoguchi et al., 2005) is present at 158.6 m CSF-B and a provisional match to the onland Habutaki ash layer (2.8-2.9 Ma; Satoguchi et al., 2005) is located at 76.825 m CSF-B.

XRF analyses were performed on 57 samples from Holes C0011C and C0011D to estimate the bulk chemical composition of the sediments and to characterize compositional trends with depth and/or lithologic characteristics (Fig. F30). As shown by the underlying units (Underwood et al., 2010), major element contents in the hemipelagic mud and mudstone of Unit I span a relatively small range of values, and the compositions resemble those of the upper continental crust as defined by Taylor and McLennan (1985). A few samples of volcanic ash and volcanoclastic layers were analyzed. They all have higher silica and lower aluminum content than the background sediment and slightly lower iron content but variable alkaline content. Several samples have a high-potassium rhyolite composition. Other samples, and notably the tuffaceous sandstones in Unit II, have relatively high sodium and calcium but low potassium content and correspond to more typical calco-alkaline rhyolite and dacite compositions. This variability in bulk chemistry suggests that volcanic materials originate from different sources (presumably Kyushu vs. Izu-Bonin).

The deposition mode for Subunit IA was dominated by hemipelagic settling. A small MTD is observed in the uppermost few meters of Holes C0011C and C0011D, between 0.85 and 2.77 m CSF-B (Core 333-C0011C-1H). However, several volcanic ash layers display turbidite characteristics (basal lamination and upward fining), suggesting these were remobilized by subaqueous gravity flow. Deposition of Subunit IB was dominated by hemipelagic settling with minor contributions of volcanic coarse sand-sized ash and fine (silt- and clay-sized) ash that becomes more abundant toward the base of the subunit. During the deposition of the upper part of Unit II, the paleoenvironment was dominated by transport of sand from a volcanic source. Miocene sandy turbidites have been previously identified in the Nankai Trough and Shikoku Basin. The Miocene siliciclastic turbidites at Site 1177 are generally older and were derived from a relatively large land mass, most likely southern Japan. That middle–late Miocene (15–7 Ma) dispersal system spread terrigenous sediment over a broad area of the Shikoku Basin (Moore, Taira, Klaus, et al., 2001; Fergusson, 2003). Conversely, the younger tuffaceous sandstones at Site C0011, on the northeast side of the basin, have been linked to a provenance in the Izu-Bonin volcanic arc (Underwood et al., 2010).

Structural geology

Holes C0011C and C0011D provide sparse and subtle structures. Structural features encountered in Hole C0011B are subhorizontal to moderately dipping beds, high- to moderately dipping small faults, planar shear zones, and low-angle healed faults (found in lithologic Subunit IB and Unit II) (Fig. F31). Sediment-fill veins (vein structures) also develop in the shallow part. Most faults and shear zones are observed over the 30–190 m CSF interval, which may be in part due to better observations on HPCS rather than ESCS cores. Two conjugate sets of northwest–southeast and north-northeast–south-southwest striking normal faults can be distinguished (Fig. F32). The strikes of these conjugate sets are, respectively, orthogonal to Nankai subduction convergence (300°–310°N; Miyazaki and Heki, 2001; Henry et al. 2001; Loveless and Meade, 2010) and orthogonal to the local direction of compression inferred from kinematic modeling of the Zenisu-Izu fault system (20°N; Mazzotti et al., 2001). It is therefore possible that the state of stress at Site C0011 is influenced by intraplate deformation within the Philippine Sea plate.

Paleomagnetism

Shipboard paleomagnetic studies for Holes C0011C and C0011D were performed with remanent magnetization and magnetic susceptibility measurements of discrete samples. Recovered sediments showed considerable variations in magnetic properties

and demagnetization behavior in Holes C0011C and C0011D. Because AF demagnetization of 30 mT can effectively remove drilling-induced remagnetization, the remanent magnetization of 30 mT inclinations were used for magnetostratigraphy. Based on our data, the geologic age throughout the cores is from 0 to ~7 Ma (Fig. F33). An average sedimentation rate in the cores is calculated at ~4.6 cm/k.y. The sedimentation rate changes rapidly downhole from ~2.7 cm/k.y. to ~7.5 cm/k.y. at ~80 m CSF-B (or ~3.0 Ma).

Physical properties

Bulk density and resistivity values generally increase from the surface to 50 m CSF, reflecting normal consolidation of sediments (Fig. F34). However, from ~50 to 80 m CSF density and resistivity decrease and then remain anomalously constant from 80 to 240 m CSF. Below 240 m CSF, density and resistivity increase abruptly and then continue along a normal consolidation trend. This behavior is similar to that observed at Ocean Drilling Program (ODP) Leg 190 Sites 1173 and 1177, where the base of the zone showing retarded compaction was ascribed to dissolution of opal-CT cement (Spinelli et al., 2007). Sediment strength generally increases with depth, though vane shear and penetrometer measurements could not be made below 160 m CSF because of high sediment strength (Fig. F35). Resistivity and acoustic velocity measurements conducted on discrete cubes from below 215 m CSF show normal trends of increasing resistivity and velocity with depth, including elevated resistivity and velocity in volcanoclastic sands at the top of Unit II (Fig. F36). Anisotropies in the vertical plane show that with depth the z-direction becomes slower and more resistive, which is consistent with uniaxial consolidation of transversely isotropic, bedded sediments. Two transitions were shown by LWD data at Site C0011, one at 212 m LSF (downward decrease in gamma ray with a small associated decrease in resistivity) and one at 251.5 m LSF (downward increase in resistivity and gamma ray). The transition at 251.5 m LSF is obviously associated with the strong porosity and resistivity gradient observed between Subunits IA and IB. At this date, the upper transition is not correlated with any remarkable observations on cores except, perhaps, a 1 m thick silt layer at 200.4–201.4 m CSF. During HPCS operations, downhole temperature was measured with the APCT-3 at ~30 m intervals. We completed one measurement in Hole C0011C at 22.5 mbsf and eight measurements in Hole C0011D from 49 to 184 mbsf. Data show a nearly linear increase in temperature with depth ($0.0913^{\circ}\text{C}/\text{m}$) (Fig. F23), corresponding to a heat flow value of $89.5 \text{ mW}/\text{m}^2$. Temperature extrapolated at basement (~1050 m, from seismic profile), taking into account heat conductivity variations in the cored intervals, is $\sim 80^{\circ}\text{C}$.

Inorganic geochemistry

Inorganic geochemical objectives at this site were to document the variations in interstitial water chemical composition in shallower depth, which were recovered during Expedition 322. Whole-round lengths ranged from 19 to 41 cm and pore water volumes per centimeter of core range from 1.7 to 2.8 mL/cm between 0 and 378.6 m CSF (Fig. F37). Because of the more consolidated nature of the formation in the deeper portion of this site and the coring techniques used, some of the deeper cores were quite disturbed. We were able to use sulfate concentrations to identify and quantify contamination in the deeper cores. Results are generally consistent between Hole C0011B (Expedition 322) and Holes C0011C/C0011D (Expedition 333) data, except for bromide, for which there is an offset, still unexplained. Chlorinity increases rapidly with depth in the upper ~25 m of Holes C0011C and C0011D, stays close to seawater value from 25 to 250 m CSF in Hole C0011D, and then gradually decreases below 130 m CSF in Hole C0011D (Fig. F38). The chlorinity decrease, which continues to the deeper interstitial waters of Hole C0011B taken during Expedition 322, may reflect the updip migration of interstitial water freshened by the smectite-illite reaction at greater depths below the trench and prism toe. Another remarkable feature is a sharp drop in silica concentration (also coincidental with a lithium concentration maximum) at the level of the transition from lithologic Subunit IA to IB (Fig. F39). Remarkably, this drop correlates with a decrease in porosity from ~65% to ~55% observed over <10 m in moisture and density data as well as with a concurrent resistivity increase in LWD and core data. The high (~800 mM) silica concentration in the fluid in Subunit IA supports the hypothesis that the retarded compaction in lithologic Subunit IA is due to a opal-CT cement, as proposed for Sites 1173 and 1177 (Spinelli et al., 2007). At the level of the tuffaceous sandstones (350–370 mbsf), a secondary silica concentration maximum is observed, which may be related to ash alteration. This interval is also characterized by higher barium concentration and slightly decreased lithium and strontium relative to the trend defined from concentrations above and below.

Organic geochemistry

Methane was the only hydrocarbon gas detected at Site C0011 and it occurs only in low concentrations (2 ppmv) in the uppermost 250 m of the cored sequence (Fig. F40). Thereafter, methane concentration gradually increased to reach highest values (~900 ppmv) at 380 m CSF.

TOC, TN, and TS contents are generally low in all lithologic units, averaging 0.31 ± 0.10 , 0.06 ± 0.01 and 0.14 ± 0.97 wt%, respectively (Fig. F41). At the base of Subunit IA and top of Subunit IB, several samples display higher TS values, including a pyrite-rich specimen at ~12 wt%. Carbon to nitrogen ratios (TOC/TN) were 5.67 ± 1.60 , indicating a marine origin for the sedimentary organic matter. The calcium carbon content varied between 0.2 and 24.5 wt% and shows highest concentration in the upper part of Subunit IA and over the transition from Subunit IA to IB. Rock-Eval derived T_{\max} values range from 399° to 414°C and indicate a thermally immature state of the organic matter.

Site C0012

The main objectives of returning to Site C0012 were to perform temperature measurements for heat flow determination, to expand the age-depth models into the Pliocene and Quaternary, and to core the basement to at least 100 m below the sediment/basement interface. Knowledge of thermal state, interstitial water geochemistry, hydrologic properties, and basement alteration are needed to characterize the state of the subduction inputs and model their evolution with downdip increases in temperature and pressure.

Operations

Without picking up the transponders from Site C0011, the *Chikyu* moved to Site C0012 after the coring assembly was retrieved on board at 1930 h on 24 December 2010. Transit in dynamic positioning (DP) mode over a distance of 5 nmi at 5 kt finished at 2030 h. From 2200 h, transponders were dropped and set at four different locations and calibrated. The location was set at 0815 h on 25 December upon finishing of DP calibration.

The HPCS/EPCS/ESCS coring assembly was made up and run into Hole C0012C to 3528 m drilling depth below rig floor (DRF). After tagging the seafloor at 3540.5 m DRF at 1600 h, HPCS coring began at 1630 h. After coring the eleventh core, a hydraulic piston system motor malfunction caused a delay from 1300 to 1500 h. After coring the fifteenth core at 2130 h, the core wire parted when the sinker bar assembly was overloaded. Hence, the sinker bar fell to the bottom of the hole and the damaged core line was cut at ~100 m. The hole was abandoned after spotting kill mud.

The *Chikyu* moved to Hole C0012D while waiting on weather from 0600 to 0800 h on 27 December. Test coring was done at seafloor at 1000 h and washed down to

20 mbsf at 1330 h and then drilled down to 118 mbsf. HPCS coring began at 1745 h and continued to 180 mbsf, where strong wind caused ship offset by ~16 m and stopped coring at this hole. We pulled out of Hole C0012D above the seafloor at 1900 h and waited on weather.

The *Chikyu* moved to Hole C0012E and the decision was made to drill down and core the sediment/basement interface with the ESCS to make the best use of a short good weather window. Hole C0012E was spudded at 1030 h on 29 December, washed down to 28.5 mbsf, and then drilled to 500 mbsf, which was reached at 1045 h on 30 December. After preparation for coring, the first ESCS core was taken at 1415 h and coring continued to 528.5 mbsf. Coring was stopped at 2245 h because of deterioration of the weather and the BHA was pulled out of hole.

Making up the RCB coring assembly for Hole C0012F started at 0230 h on 1 January 2011 while waiting on weather. The BHA was run to 3530 m DRF, spudded at 1315 h, and drilled to 520 mbsf. RCB coring began at 1500 h on 2 January but ended at 1930 h after the second core was taken because of abnormal pressure while coring. After cleaning the outer core barrel and the hole, the center bit assembly was set for a circulation test. The test was successful, but the center bit assembly could not be retrieved because the pull bar broke, which ended coring operations in Hole C0012F. Pulling out of the hole took place between 0730 and 1615 h.

The RCB coring assembly for Hole C0012G was made with a roller cone bit after finding out that more than half of the teeth on the polycrystalline diamond compact drill bit (PDC) used in Hole C0012F were worn out. Running pipe down started at 1815 h on 3 January, and Hole C0012G was spudded at 0900 h on 4 January. We drilled to 515 mbsf and began RCB coring with full advance at 1315 h on 5 January. Full advance coring continued to 591 mbsf with medium to poor recovery. We then switched to a shorter advance to improve core recovery to 630.5 mbsf. Coring in Hole C0012G ended at 1545 h on 7 January, and kill mud spotting and pulling out of the hole lasted until 0330 h on 8 January.

Coring operations were disturbed twice by short intervals of low-pressure weather. In addition to weather, there were two incidents that forced us to pull out of the hole: a parted core wire and a parted center bit at the bottom. Core quality and recovery varied depending on the formation or lithology and also with corer and drill bit types. Core recovery was excellent for the piston cores in Holes C0012C and C0012D, with average rates of 103.3% and 104%, respectively, and also presents a marked improve-

ment in quality from Expedition 322 RCB coring. In comparison to Site C0011, cores from Site C0012 had almost constant recovery without broken cores or becoming jammed. However, Cores 333-C0012D-8H to 13H (bottom of Hole C0012D) were affected by coring disturbance (flow in and stretching). ESCS was used in Hole C0012E to core only at the sediment/basement interface and yielded the best quality cores compared to three other attempts with RCB. Average recovery was 48.6%, ranging from 11.4% to 87.9%. Holes C0012F and C0012G used RCB coring but with different bits. RCB coring with a damaged PDC bit in Hole C0012F yielded two cores with an average recovery of 48.2%. Hole C0012G was cored deep into the basaltic basement with a roller cone bit. Core recovery was 22.4% in average, varied between 9.6% and 45.8% for the full advance cores, and varied between 4.1% and 73.2% for the half advance in the deeper part of the hole.

Lithology

In Holes C0012C and C0012D, 180 m of lithologic Unit I (Shikoku Basin hemipelagites) and the upper part of lithologic Unit II (middle Shikoku Basin volcanic sand facies) were drilled during Expedition 333 (Fig. F42). The remaining holes (C0012E, C0012F, and C0012G) aimed at drilling red calcareous claystone and basalt at the contact between sediments in the Shikoku Basin and the igneous oceanic crust. The cores brought new information on lithologic Unit I not acquired during Expedition 322 because of severe coring disturbance and poor recovery. Three lithologic subunits were interpreted in Unit I: Subunit IA (youngest), Subunit IB, and Subunit IC. The subunits are distinguished based on the presence, frequency of occurrence, and thickness of volcanic ash layers. The lithologies in Holes C0012C and C0012D include dark greenish gray clay and silty clay and silt interbedded with volcanic ash and minor occurrences of thin sand. A major change in the frequency of the occurrence of ash layers is recorded at ~71.5 m CSF, thereby defining the Subunit IA/IB boundary. Ash alteration was observed from 91.2 m CSF-B to the lower part of Subunit IB. Within Subunit IB, ash layers are scarce to ~124.2 m CSF, below which another interval of dark greenish gray clay/silty clay with abundant ash layers extends to 151.61 m CSF-B. This depth for the base of Unit I matches closely with the designation of 150.9 m CSF that was made during Expedition 322 (Underwood et al., 2010). Beginning at 151.61 m CSF, Unit II comprises turbidite sands and sandstones with sharp and well-defined upper and lower boundaries. Commonly, beds have normal grading, but some are intercalated with intervals of massive beds with or without clay clasts. At the base of normal graded beds, pebble and sand clasts are composed of coarse ash and lapilli tuff. The lower part of Unit II comprises several layers of carbonate-cemented sand-

stones with calcite and barite veins. These beds are separated by mudstone very similar to that of Subunit IC. The base of Unit II was not cored during Expedition 333 but was fixed at 219.8 m CSF in Hole C0012A (Underwood et al., 2010).

Nannofossils are the dominant group of microfossils and are found in both Units I and II. Sponge spicules, diatoms, and radiolarians occur as a rare or trace component in most of Subunit IA, being relatively more abundant at the top of the subunit. Below ~85 m CSF-B they were not identified. Bulk powder XRD data indicate an average content of 63% clay minerals, with the lowest content (~45%) characterizing the uppermost 15 m. There is on average about 19% quartz and 18% plagioclase; both show uniform values throughout Units I and II (Fig. F43). The calcite content is highest in the upper 15 m, where it reaches ~25% (Figs. F43). Below 15 m CSF the calcite content of Subunit IA is very low, dropping the average for the subunit to 4% except for Subunit IB where it varies from 0% to 20% and averages 6%. Major element concentrations of Unit I and II from XRF analyses span a relatively small range of values (Fig. F44) and resemble those of the upper continental crust as defined by Taylor and McLennan (1985).

The cored portion of Units I and II has an estimated Holocene–late Miocene age (~0–8.3 Ma). The Azuki volcanic ash bed, dated on land as 850.000–900.000 y (Yoshikawa and Mitamura, 1999) was identified at 5.7 m CSF-B. The Pink ash bed, dated on land as 0.99–1.05 Ma (Yoshikawa and Mitamura, 1999), correlates with an ash layer at 7.7 m CSF-B. A third major volcanoclastic event, the Ohta ash bed, dated on land as 4.0 Ma (Satoguchi et al., 2005), seems to coincide with an ash bed at 44.04 m CSF-B (Fig. F42). The depth of the presumed Azuki and Pink ash beds implies very slow sedimentation rates over the last ~1 Ma. This interpretation is, however, consistent with the depth of the Brunhes-Matuyama reversal and of the Jaramillo Chron from natural magnetic remanence data. This interval of condensed sedimentation lies on an angular unconformity and hiatus at ~15 m CSF, interpreted as the top of a slump. Other, yet unresolved, hiatuses may account for the very slow apparent sedimentation rate above this unconformity.

The deposition of Subunits IA and IC was dominated by hemipelagic settling and frequent volcanic eruptions, whereas the time interval of Subunit IB experienced fewer volcanic eruptions. During deposition of the upper part of Unit II, the paleoenvironment was dominated by deposition from a sandy system with a volcanic provenance. In comparison to Holes C0011C and C0011D, the Miocene sandy turbidites are finer grained on top of the bathymetric high and the thick tuffaceous sandstone layers

characteristic of the middle Shikoku Basin facies were not observed. On the other hand, pebbly and mixed layers evocative of MTDs were found.

Hole C0012E recovered two cores of greenish yellow mudstone intercalated with thin sandstone layers from 500 m CSF, corresponding to the base of lithologic Unit V (volcaniclastic-rich facies) defined during Expedition 322 (Underwood et al., 2010), and one core from 519 m CSF that recovered 6.8 m of reddish brown calcareous claystone with lighter green layers, overlying altered pillow basalts. The interface between the red calcareous claystone and the basaltic basement was also recovered in Holes C0012G and C0012F. The red calcareous claystone corresponds to Expedition 322 lithologic Unit VI (pelagic claystone) (Underwood et al., 2010) and holds veins of calcite with traces of barite as well as several layers with accumulations of manganese oxide forming millimeter- to centimeter-sized lumps. As observed during Expedition 322, the basalt is highly altered and some voids remaining between basalt pillows are filled with analcime. Hole C0012G cored pillows and massive phyric basalts from 525.69 m CSF to the base of the hole at 630.5 m CSF. Observations of thin sections showed that all olivine and glass (except in one sample) as well as a large fraction of the plagioclases have been replaced by secondary phases—dominantly saponite and zeolites—that are also present as vesicle fillings. The basalt experienced localized alteration under iron oxidizing conditions with accumulation of iron hydroxides in veins, but most of the rock mass was pervasively altered under reducing conditions forming saponite and, locally, pyrite. A more complete description will be available after the shore-based sampling party planned at Kochi Core Center.

Structural geology

Structures observed at Site C0012 mainly consist of bedding planes, faults, shear zones, and chaotic structures (Fig. F45). Bedding planes show a large range of dipping angles from 3° to 70° but are organized in zones of low and high bedding dips. Bedding planes with low dips are characteristically observed in Zone I (0–15 m CSF) (Fig. F45B) and Zone III (85–145 m CSF). However, high dip angle beds are found in Zone II (15–85 m CSF), where they consistently strike northeast–southwest (Fig. F45C) and dip southeast, and in Zone IV (145–180 m CSF) where the distribution of strikes and dips appears scattered. There is an angular unconformity between Zone I low-angle bedding and Zone II high-angle bedding. Faults are mostly normal faults with high dip angles, striking northwest–southeast, and dipping northeast or southwest, suggesting northeast–southwest extension (Fig. F45D). Shear zones generally have high dip angles with large displacements. Chaotic structures are composed of disrupted beds, folds, and injections of sand or mud and observed at the bottom of Zone II and

Zone IV. Considering the location of Site C0012 on a topographic high southwest of a steep slope evocative of a slide scar, one interpretation proposed is that Zone II corresponds to a slump that was later covered by flat-lying sediments, whereas Zone IV may have been affected by multiple (and older) sliding events. Paleomagnetic data suggests that the unconformity between Zone I and Zone II correlates with an age hiatus. Similar observations within the upper part of Unit III during Expedition 322 suggested that a slumping event associated with the remobilization of the uppermost sedimentary layers also occurred about 9.5 m.y. ago (Underwood et al., 2010).

Paleomagnetism

Paleomagnetic shipboard studies for Site C0012 were performed with remanent magnetization and magnetic susceptibility measurements of discrete samples (Fig. F46). Magnetostratigraphic correlations indicate the age of the sediments in Holes C0012C and C0012D range from present day at the seafloor to >8 Ma at the bottom of the hole (~180 m CSF). Following AF demagnetization to 30 mT, inclination values were variable. Bedding correction performed on the specimens clustered the data near the expected ~52° but did not affect the chron and subchron boundaries. The Bruhnes/Matuyama boundary was detected in Core 333-C0012C-2H, and tephra chronology identified the Pink tephra layer in Core 333-C0012C-3H within the lower portion of the Jaramillo Subchron and the Ohta tephra layer in Core 333-C0012C-6H within the Gilbert Chron. A thickness of only 9 m between these two chrons indicates that the lower section of the Matuyama Chron is probably missing. Correlation of the magnetic susceptibility between Sites C0011 and C0012 indicates a hiatus at ~14 m CSF at Site C0012, spanning roughly 2 m.y. (1.07–3 Ma), coincident with an angular unconformity (Fig. F46). Below this level, the sedimentation rate displays some variations, notably a possible hiatus at the base of the slump (~5 Ma), and faster sedimentation rates in lithologic Unit II before 7.4 Ma.

Physical properties

From the surface to ~10 m CSF, porosity decreases downhole, as expected for progressive burial. Below 10 m CSF, porosity slightly increases and then remains relatively constant until ~70 m CSF, which coincides with the lithologic Subunit IA/IB boundary (Fig. F47). Within this anomalous interval, electrical resistivity also remains constant while shear strength increases, and there is an anomalous shift in the concentration of dissolved silica. Between 70 and 100 m CSF, porosity sharply decreases and electrical resistivity and shear strength increase. Porosity increases and then decreases between 100 and 170 m CSF, followed by a steady compaction trend,

with some scatter in sand-rich units, to the base of the borehole. Sandstones are also indicated by spikes of high magnetic susceptibility and low natural gamma ray. Site C0012 porosity values from below 240 m CSF are generally lower than those from similar depths at Site C0011 (Fig. F48). A possible explanation for the lower porosity at Site C0012 is removal of overlying material by erosion or slope failure. This interpretation would be consistent with the observed time gap of ~2 m.y. found between 12 and 18 m CSF and the structural evidence of an angular unconformity. Claystones from below 500 m CSF range in porosity from 0.28 to 0.46 and show *P*-wave velocities ~2000 m/s (Fig. F49). Within the basalt, measured porosity is extremely variable and ranges from 0.09 to 0.37. Measured *P*-wave velocities vary between 3000 and 5000 m/s.

Electrical resistivity is greater in the *z*-direction within the claystones but lower within the basement. Higher resistivity in the *z*-direction in the sediments is consistent with a transversely isotropic medium in which the bedding planes are approximately horizontal (Fig. F49). Within the basement, electrical conductivity may be enhanced by subvertical veins or fractures filled with more conductive material, resulting in a lower resistivity in the *z*-direction.

Thermal gradient values are evaluated from the APCT-3 measurements made at 10 depths in Holes C0012C and C0012D together, and the mean thermal gradient value determined is 0.135 K/m (Fig. F23). The estimated heat flow value at this site is 141 mW/m², amounting to ~50% higher than the 89.5 mW/m² determined for the adjacent Hole C0011C that was drilled during this expedition. Based on the determined heat flow value of 141 mW/m², as well as the thermal conductivity values that we have obtained on board by core measurements, temperature at the top of basement (at 526 m CSF) is estimated to be ~65°C, which is significantly lower than the estimated value of 80°C at Site C0011. We suspect that fluid convection, perhaps occurring in the basement, is transferring heat between the two sites, thus resulting in a higher heat flow at Site C0012, which is located on the topographic high. However, the effect on heat flow of sedimentation and also of sediment removal by gravity sliding at Site C0012, should also be considered in models.

Inorganic geochemistry

The main objective of the inorganic geochemistry program at this site was to document the geochemical properties of subduction inputs at a site located above a basement high, near the crest of the Kashinosaki Knoll. A total of 28 pore fluid samples were squeezed from selected whole-round sections for chemical and isotopic analyses. To obtain enough interstitial water for shipboard and shore-based analyses, 19–31 cm

long sections were squeezed in Holes C0012C and C0012D. In the red claystone located directly above the basement in Hole C0012E, sections 59.5–61 cm in length were squeezed. Pore fluid volumes per length of interstitial water section decrease with depth, from 2.75 to 0.71 mL/cm of core in the upper ~180 m CSF of Holes C0012C and C0012D (Fig. F50). In the deeper material above the basement, volumes were lower, ranging from 0.22 to 0.08 mL/cm. The sulfate profile for Site C0012 documents a much deeper sulfate reduction zone than observed at the other sites drilled during this expedition. During Expedition 322 it was observed that minimum sulfate concentration, which occurs at ~300 m CSF at Site C0012, coincided with a marked increase in methane concentration (Saito et al., 2010). The Expedition 322 scientists interpreted the sulfate profile at Site C0012 as being driven locally by anaerobic methane oxidation. The deeper anomaly may be attributed to lower sedimentation rates (because of the bathymetric high Site C0012 sits on), to a lower average organic matter content at Site C0012, or to differences in fluid migration. Additionally, in both Holes C0012E and C0012A sulfate increases in concentration in the interval below ~450 m CSF, which may indicate diffusion from fluid in basaltic basement with a higher sulfate concentration. In general, analytical results are consistent between Expeditions 333 and 322 (Figs. F51, F52) and interpretations proposed after Expedition 322 are not put in question by the newly acquired data. However, shipboard Br concentrations during Expedition 333 tend to be systematically lower, whereas Li and Sr concentrations tend to be higher. Overall, the combined data set reflects in situ alteration of volcanic ash alteration in the sediment and basalt alteration in the crust as well as exchange by diffusion. More specifically, the decrease in Mg and K, increase in Li and Sr, and variations in silica (Fig. F52) in the upper 200 m are probably controlled by volcanic ash alteration and equilibration of the pore fluid with clay minerals. Silica concentration drops below the Subunit IA/IB boundary at ~70 m, where a decrease in porosity and an increase in resistivity are also observed. This again suggests a relationship between pore fluid composition and the presence of opal cement. However, the silica concentration remains relatively high and variable in the 200–500 mM range from 90 to 200 m and then, according to Expedition 322 data, decreases again. These variations would not be well explained by existing models for opal dissolution and quartz precipitation (Spinelli et al., 2007). This suggests that other sources of silica are present (e.g., volcanic ash alteration) and that silica concentration in this interval is not limited by quartz precipitation. The trend of increasing chlorinity (Fig. F51), Ca, and Sr (Fig. F52) concentration and decreasing Na in the lower part of the borehole is interpreted as a consequence of diffusion between sediment and basement fluids.

Organic geochemistry

At Site C0012, methane and ethane were either below detection or present at only low concentrations. No heavier hydrocarbon gases (i.e., C₃ and C₄) were found. The only two samples that contained both methane and ethane were found at depths of ~501 and ~520 m CSF and had C₁/C₂ ratios <100, indicating a possible thermogenic origin of these hydrocarbon gases (Fig. F53). Calcium carbonate (CaCO₃) concentrations ranged between 0.2 and 45.1 wt% and averaged 6.1 wt% (Fig. F54). Sediment below 500 m CSF contained higher amounts of CaCO₃ compared to the upper 180 m CSF of the cored sequence. TOC, TN, and TS concentrations were low, ranging between 0.03 and 0.46 wt%, 0.03 and 0.07 wt%, and 0 and 0.49 wt%, respectively. The TOC/TN_{at} fell in the range of 1.3–9.3, suggesting a marine origin of the organic matter. The variations of these four elemental parameters shared a similar pattern, including scattered values but displaying a generally increasing trend with depth in the upper 52 m CSF, relatively uniform values between 52 and 180 m CSF, as well as low values between ~500 and 525 m CSF.

Preliminary scientific assessment

Expedition 333 achieved its primary objectives regarding the sedimentary sequence. Basement coring was limited to the upper 100 m as a consequence of adverse weather conditions and a technical failure (destruction of PDC bit). Yet, additional cores from across the sediment/basalt interface and from basalt obtained at deeper levels than during Expedition 322 will yield important shore-based results. Temperature measurements with the APCT-3 at all three sites and thermal conductivity measurements on cores yielded precise determinations of heat flow, which are slightly lower than heat flow probe data acquired on the Muroto transect (Kinoshita et al., 2008). Cores filling the gaps between the seafloor and the top of RCB coring during Expedition 322 were recovered, and some overlap was achieved to provide a continuous data set. The sediment/basement interface was recovered again, with ESCS in Hole C0012E and RCB in Holes C0012F and C0012G, and interstitial fluid samples were extracted again from the sediment immediately above the interface. The 8.20 m core taken across the interface with ESCS was of very good quality. Postcruise work on these new samples will complement the analyses performed on Expedition 322 cores, notably with fluid isotopic chemistry and hydrological and mechanical tests.

At the NanTroSLIDE site, coring with HPCS, EPCS, and finally ESCS provided nearly continuous recovery across a thick MTD (our primary target) near its edge. The depth, thickness, age, composition, and structural character of this MTD were determined, as well as that of several thinner intervals of sediment disturbed by slope instability processes. The target depth (350 mbsf) was not drilled, but sufficient recovery was achieved below the thick MTD to 314 m CSF to characterize the underlying sediments as a turbidite sequence holding little evidence for postdepositional remobilization. The primary goals of drilling at Site C0018 were thus reached. Tephrochronology, paleomagnetism, and preliminary micropaleontology results are consistent, and good quality dating will be obtained over most of the cored interval in spite of the reworking of sediment inherent to a MTD sequence. The age of the thick MTD can already be bracketed between 0.85–0.9 Ma and 1.05 Ma from two ash layers of known age. Most HPCS cores taken within the MTD are of good quality and were sampled for shore-based geotechnical measurements. A thick ash layer lying immediately below the MTD was given special attention.

Data acquired during Expedition 333 address important questions regarding the state of material input to the subduction zone, which were left partially unanswered after Expedition 322. Some results on heat flow, stratigraphy, physical properties, and diagenesis are already well established by the end of the expedition. These, combined with knowledge acquired at other Nankai area drill sites (IODP and ODP) provide a basis for preliminary interpretations and orientation for postcruise studies. Other questions, notably regarding basement and sediment-basement fluid interaction, can only be achieved by postcruise work. Another important aspect of the NanTroSLIDE site is ground-truthing of MTD occurrences, based on seismic reflection images. Coring brought simple answers to several of the questions asked and some unexpected findings. The sedimentological and structural observations lead to refined hypotheses on MTD processes and their interaction with tectonic activity and sedimentation on Nankai margin.

Can a change of physical properties between 200 and 250 mbsf at Site C0011 be related to lithologic variation or diagenesis? Does the same transition occur at Site C0012?

A major change of physical properties is found at ~250 mbsf at Site C0011 and has tentatively been identified between 60 and 80 mbsf at Site C0012. This transition appears as a lithologically determined feature enhanced by diagenesis. The ash content in the sediment decreases below this boundary and an increase of the state of alteration of volcanic glass shards is observed in the remaining ash layers. Siliceous fossils

are also present above, and there is a sharp decrease in dissolved silica concentration below the boundary. From an analogy with results obtained after Leg 190, it can be proposed that the process responsible for an anomalously high porosity of the sediment above this boundary is cementation by opal-CT and opal dissolution with precipitation of quartz below the boundary (Spinelli et al., 2007). However, it is questionable that the transition observed is an opal/quartz boundary for several reasons: (1) temperature of the reaction would be unusually low at this site (currently 25°C, as opposed to 55°C at Site 1173); and (2) fresh glass is found again in volcanoclastic sands at a deeper level, associated with high silica concentration in the interstitial water. An alternate possibility is that opal-CT cements never formed in the sediment below the boundary because of a cryptic difference in bulk sediment composition (biogenic silica and/or ash content) or a difference in fluid composition and temperature at the time of diagenesis. Preliminary chronostratigraphy based on paleomagnetism suggests the age of the transition from cemented ash-bearing hemipelagites to compacted hemipelagites at Site C0011 (5.25 Ma) is slightly younger at Site 1177 (4.5 Ma), the reference site for the Ashizuri transect. It is even younger at Site 1173 (3.0 Ma), the reference site for the Muroto transect, where higher heat flow and temperature can account for a more advanced silica diagenesis and result in an upward migration of the transition in the sedimentary column (Spinelli et al., 2007). On the Kumano transect, this transition could coincide with a primary (depositional) lithologic boundary.

Is fluid circulation in basement and permeable sedimentary layers influencing heat flow and diagenesis at Sites C0011 and C0012?

Heat flow measured during Expedition 333 is 90 mW/m² at Site C0011 and 140 mW/m² at Site C0012, respectively ~20% lower and 30% higher than the heat flow expected from conductive cooling of a 20 Ma lithosphere (Kinoshita et al., 2008). The temperatures extrapolated to basement are, respectively, 79° and 65°C at Sites C0011 and C0012. Large variations of heat flow correlated with basement topography are often reported in zones where off-ridge hydrothermal convection is occurring and may be accounted for by supercritical Rayleigh convection (e.g., Fisher et al., 2003). Such a mechanism could account for the heat flow contrast between Site C0011 located on the flank of the Kashinosaki Knoll where sediment thickness is ~1 km and Site C0012, located near its summit where sediment thickness is 520 m. Whether larger scale fluid circulation in the basement (Spinelli and Wang, 2008), rather than mantle and magmatic processes, should be invoked to explain regionally elevated heat flow in the eastern part of the Shikoku Basin remains an open question.

Data acquired during Expedition 333 provide few new arguments in favor of fluid flow along permeable sedimentary horizons. At Site C0011, a higher barium concentration is observed at the level of the presumably permeable middle Shikoku Basin volcanic sandstone interval, as well as slightly higher (Ca and K) and lower (Sr and Li) concentrations of several other elements. These are possibly influenced by lateral flow. However, rigorous assessment of lateral flow will require postcruise modeling with consideration of local equilibrium and diagenetic reactions. This is now possible due to successful heat flow measurements.

How does contrasting pore fluid chemistry at Sites C0011 and C0012 relate with in situ diagenesis, fluid flow, and heat flow?

Temperature and heat flow determinations indicate that the temperature conditions in the uppermost basement at Site C0011 are within the temperature window for the onset of the smectite-illite reaction (~55°–90°C). Unfortunately, coring during Expedition 322 was aborted almost 200 m above the top of basement at Site C0011. Although it is unlikely that the reaction has progressed to a significant extent in any of the cored sections, illitization should be expected in the lower part of Site C0011 and it should continue into the trench where the Shikoku Basin sediments are buried to greater depths. Overall, the temperature conditions at correlative stratigraphic levels do not vary strongly between the two drill sites. Consequently, differences in fluid composition between the two sites (e.g., increasing versus decreasing chlorinity toward basement) likely result from diffusion and advection processes.

Is magmatic activity heterogeneous in composition and age on a backarc basin basement high? Is alteration of the upper oceanic basement heterogeneous and how does it influence geochemical and fluid budgets?

These questions can only be answered postcruise, but preliminary analyses do not indicate heterogeneity in composition in the 100 m cored. Early oxidizing alteration localized around fractures and pillow rims may be distinguished from pervasive replacement under reducing conditions of glass and mineral phases (olivine and, often, plagioclases) by saponite and zeolites, which may preclude precise radiometric dating. Core recovery was poor in the upper part of the basement but improved downward as advance was reduced. Although drilling operations during Expedition 333 demonstrate the possibility to maintain a steady rate of penetration while coring in basement, suggestions for improving efficiency and core quality may be driven by our experience as well as that of Expedition 322.

Other questions at input sites

We already pointed out an important outcome of Expedition 333, which is the description of a transition in physical properties and lithology that has strong similarities (sharp porosity decrease with depth, variation in ash occurrence and alteration state, and variation in silica concentration in the interstitial water) with transitions observed on the Muroto and Ashizuri transects at the facies boundary between the upper and lower Shikoku Basin. The depth of this basin-wide transition is at least in part determined by silica diagenesis (Spinelli et al., 2007) and, as may be expected for a diagenetic front, is diachronous, ranging from 5.25 Ma at Site C0011 to 2.5–3 Ma on the Muroto transect (Moore et al., 2001). On the other hand, Expedition 322 identified important local variations in facies in the lower part of the sedimentary column (>7.5 Ma), which led to the definition of the middle Shikoku Basin volcanic sand facies (Underwood et al., 2010). In this context, it is remarkable that the active décollement of the accretionary wedge is located in the 5–7 Ma interval on the Muroto and Ashizuri transects (Moore et al., 2001) and, arguably, also in the 5–7 Ma interval on the Kumano transect, based on chronostratigraphic data from Sites C0006 and C0007 (Kinoshita, Tobin, Ashi, Kimura, Lallemand, Screatton, Curewitz, Masago, Moe, and the Expedition 314/315/316 Scientists, 2009) and on the correlation between Site C0011 stratigraphy and seismic profiles (Moore et al., 2009; Underwood et al., 2010). Compared with deposits above and below, this interval may be characterized by fewer (or absent) ash layers and an absence of turbidites. Understanding how the décollement apparently localizes in a specific stratigraphic interval in spite of lateral sediment heterogeneity (or, more specifically, understanding the relationships between the décollement, the diagenetic front above, and the turbidite sequences below) remains an important problem.

Site C0012 appeared strongly influenced by mass wasting processes. First, a sedimentation hiatus is found between ~1.2 and 3 Ma. Second, the sediments below the hiatus down to 90 m are affected by slumping, with dips up to 60°. Disturbed sediments evocative of MTDs were also found in the lowermost part of the interval cored during Expedition 333, as already noticed at these depths during Expedition 322. A deeper occurrence of a hiatus above slumped sediment at ~9.5 Ma was documented during Expedition 322 (Underwood et al., 2010). Repetition of mass wasting events is very understandable considering the location of Site C0012 immediately above the edge of a major slide scar that is obvious in the bathymetry and seismic data. How this may affect heat flow data should be taken into consideration in modeling efforts. Mass wasting (possibly combined with fluid movement) may also help explain the high

variability of seafloor heat flow probe measurements (Kinoshita et al., 2008) Furthermore, considering Site C0012 as a reference for sedimentation deposited on a structural high in the Shikoku Basin may bring a better understanding of stratigraphy within the accretionary wedge. For instance, Sites C0006 and C0007 at the toe of the accretionary wedge display a hiatus over the same age range (1.2–3 Ma) as Site C0012, below the transition between the Shikoku Basin hemipelagites and the distal trench deposits. We wonder whether this hiatus is related to the original depositional environment, which may also have been a structural high, or is the consequence of later tectonic deformation during offscraping.

What is the frequency of submarine landslides near the megasplay fault?

The spacing between intervals where evidence for sediment remobilization was observed in the cores at Site C0018 suggests submarine slope destabilization does not occur systematically during subduction earthquakes. The recurrence of great subduction earthquakes in the Nankai Trough is of the order of 100–200 y, whereas the recurrence of MTDs at Site C0018 is on the 100,000–200,000 y timescale. The rhythm of turbidite deposition on the slope in lithologic Subunit IB below the main MTD is probably on the 1000 y timescale and thus may not be controlled by the earthquake cycle either.

What is the source material of the MTDs? What is the importance of accretionary wedge remobilization versus surficial processes?

The MTDs sampled are remobilized slope sediments in agreement with current MCS interpretation. This, however, does not preclude that the underlying accretionary wedge could have been affected by earlier mass wasting events, or that part of the sediment deposited on this slope originate from erosion of the outer arc high (Strasser et al., 2011).

What controls type, size, and magnitude of turbidites and MTDs and how do they change through time?

MTDs display a wide range of thicknesses from about 50 cm to 20–60 m for the thickest deposits, which can be imaged by MCS. Processes of sediment mobilization may differ depending on the scale of the event and comparison of the thick MTD with smaller scale ones observed in the slope sediment sequence above will bring important insight.

Turbidite type deposits were found at the top of two MTDs and likely result from the deposition of sediments suspended during the event. However, most turbidites found at this site appear unrelated to the MTDs.

How do large MTDs relate with the timing of splay fault activity as inferred from NanTroSEIZE Stage 1 drilling?

All MTDs cored are younger than 1 Ma, and therefore postdate the initiation of the main phase of activity of this splay fault branch as defined by Strasser et al. (2009) and Kimura et al. (2011).

What are the dynamics of large submarine landslides and can we infer their tsunamigenic potential?

One important aim of postcruise research will be to understand the relationship between variations in the geotechnical properties of the sediment, and occurrence and size of instabilities. We hypothesize that the occurrences of large tsunamigenic submarine landslides, in subduction zones as elsewhere, require specific conditions, such as the presence of discrete layers sensitive to liquefaction at some depth (several tens of meters) below the seafloor. These layers may, for example, correspond to loose granular material or to strain softening clays.

Other questions regarding the NanTroSLIDE site?

The finding of a transition from turbidite-dominated sedimentation to hemipelagite and ash across the thick MTD at ~1 MA was not expected. However, this may reflect a change of depositional environment observed in this part of the accretionary wedge slope: there are few sand/silt turbidites over the last 1–1.3 Ma at Sites C0004 and C0008 and over the last 1.6 Ma at Site C0001 (Kinoshita, Tobin, Ashi, Kimura, Lalle-mant, Screatton, Curewitz, Masago, Moe, and the Expedition 314/315/316 Scientists, 2009). One possible explanation is that the uplift of the outer arc high at 1.3–1 Ma (Gulick et al., 2010) confined most of the turbidity currents to the Kumano forearc basin and thus shut off sand input to the vicinity of Site C0018. Alternatively, the local evolution observed could correspond to a local change of slope and depositional environment from a perched basin trapping sand transported by turbidity currents to a slope environment.

Another important outcome of observation on cores is the heterogeneous nature of deformation within MTD deposits. Chaotic, pebbly, or mixed sediment intervals co-exist with intervals of coherent bedding dips. Localized deformation structures such

as shear zones and fault were also identified. As observations on core are done at a smaller scale than the resolution of MCS profiles, the transparent appearance of the MTD on these profiles can be understood even though they often retain coherent intervals. However, the inner style of deformation of the MTDs cored at Site C0018 is more akin to slumps, dominated by plastic deformation, than to mud flows behaving as fluid.

References

- Alves, T.M., and Lourenço, S.D.N., 2010. Geomorphologic features related to gravitational collapse: submarine landsliding to lateral spreading on a late Miocene–Quaternary slope (SE Crete, eastern Mediterranean). *Geomorphology*, 123(1–2):13–33. doi:10.1016/j.geomorph.2010.04.030
- Ashi, J., Kuramoto, S., Morita, S., Tsunogai, U., Goto, S., Kojima, S., Okamoto, T., Ishimura, T., Ijiri, A., Toki, T., Kudo, S., Asai, S., and Utsumi, M., 2002. Structure and cold seep of the Nankai accretionary prism off Kumano—outline of the off Kumano survey during YK01-04 Leg 2 cruise. *JAMSTEC J. Deep-Sea Res.*, 20:1–8. (in Japanese, with abstract in English)
- Bangs, N.L.B., Gulick, S.P.S., and Shipley, T.H., 2006. Seamount subduction erosion in the Nankai Trough and its potential impact on the seismogenic zone. *Geology*, 34(8):701–704. doi:10.1130/G22451.1
- Byrne, D.E., Davis, D.M., and Sykes, L.R., 1988. Loci and maximum size of thrust earthquakes and the mechanics of the shallow region of subduction zones. *Tectonics*, 7(4):833–857. doi:10.1029/TC007i004p00833
- Conin, M., Henry, P., Bourlange, S., Raimbourg, H., and Reuschlé, T., 2011. Interpretation of porosity and LWD resistivity from the Nankai accretionary wedge in light of clay physicochemical properties: evidence for erosion and local overpressuring. *Geochem., Geophys., Geosyst.*, 12:Q0AD07–Q0AD23. doi:10.1029/2010GC003381
- Dessa, J.-X., Operto, S., Kodaira, S., Nakanishi, A., Pascal, G., Uhira, K., and Kaneda, Y., 2004. Deep seismic imaging of the eastern Nankai Trough, Japan, from multifold ocean bottom seismometer data by combined travel time tomography and prestack depth migration. *J. Geophys. Res., [Solid Earth]*, 109(B2):B02111. doi:10.1029/2003JB002689
- Ferguson, C.L., 2003. Provenance of Miocene–Pleistocene turbidite sands and sandstones, Nankai Trough, Ocean Drilling Program Leg 190. In Mikada, H., Moore, G.F., Taira, A., Becker, K., Moore, J.C., and Klaus, A. (Eds.), *Proc. ODP, Sci. Results*, 190/196: College Station, TX (Ocean Drilling Program), 1–28. doi:10.2973/odp.proc.sr.190196.205.2003
- Fisher, A.T., 1998. Permeability within basaltic oceanic crust. *Rev. Geophys.*, 36(2):143–182. doi:10.1029/97RG02916
- Fisher, A.T., Stein, C.A., Harris, R.N., Wang, K., Silver, E.A., Pfender, M., Hutnak, M., Cherkouhi, A., Bodzin, R., and Villinger, H., 2003. Abrupt thermal transition reveals hydrothermal boundary and role of seamounts within the Cocos plate. *Geophys. Res. Lett.*, 30(11):1550–1553. doi:10.1029/2002GL016766
- Frey-Martínez, J., Cartwright, J., and James, D., 2006. Frontally confined versus frontally emergent submarine landslides: a 3D seismic characterisation. *Mar. Pet. Geol.*, 23(5):585–604. doi:10.1016/j.marpetgeo.2006.04.002
- Gulick, S.P.S., Bangs, N.L.B., Moore, G.F., Ashi, J., Martin, K.M., Sawyer, D.S., Tobin, H.J., Kuramoto, S., and Taira, A., 2010. Rapid forearc basin uplift and megasplay fault development from 3D seismic images of Nankai Margin off Kii Peninsula, Japan. *Earth Planet. Sci. Lett.*, 300(1–2):55–62. doi:10.1016/j.epsl.2010.09.034
- Hayashida, A., Kamata, H., and Danhara, T., 1996. Correlation of widespread tephra deposits based on paleomagnetic directions: link between a volcanic field and sedimentary sequences in Japan. *Quat. Int.*, 34–36:89–98. doi:10.1016/1040-6182(95)00072-0
- Heki, K., 2007. Secular, transient and seasonal crustal movements in Japan from a dense GPS array: implication for plate dynamics in convergent boundaries. In Dixon, T., and Moore,

- C. (Eds.), *The Seismogenic Zone of Subduction Thrust Faults*: New York (Columbia Univ. Press), 512–539.
- Henry, P., Mazzotti, S., and Le Pichon, X., 2001. Transient and permanent deformation of central Japan estimated by GPS: 1. Interseismic loading and subduction kinematics. *Earth Planet. Sci. Lett.*, 184(2):443–453. doi:10.1016/S0012-821X(00)00335-6
- Henry, P., Mazzotti, S., Maury, R., Robert, C., and Lallemand, S.J., 1997. Uplifted oceanic crust outcrops on Zenisu Ridge. *JAMSTEC J. Deep-Sea Res.*, 13:509–520. http://doc-srv.godac.jp/MSV2_DATA/23/13_39.pdf
- Ike, T., Moore, G.F., Kuramoto, S., Park, J.-O., Kaneda, Y., and Taira, A., 2008a. Tectonics and sedimentation around Kashinosaki Knoll: a subducting basement high in the eastern Nankai Trough. *Isl. Arc*, 17(3):358–375. doi:10.1111/j.1440-1738.2008.00625.x
- Ike, T., Moore, G.F., Kuramoto, S., Park, J.-O., Kaneda, Y., and Taira, A., 2008b. Variations in sediment thickness and type along the northern Philippine Sea plate at the Nankai Trough. *Isl. Arc*, 17(3):342–357. doi:10.1111/j.1440-1738.2008.00624.x
- Ito, Y., and Obara, K., 2006. Dynamic deformation of the accretionary prism excites very low frequency earthquakes. *Geophys. Res. Lett.*, 33(2):L02311. doi:10.1029/2005GL025270
- Kimura, G., and Ludden, J., 1995. Peeling oceanic crust in subduction zones. *Geology*, 23(3):217–220. doi:10.1130/0091-7613(1995)023<0217:POCISZ>2.3.CO;2
- Kimura, G., Moore, G.F., Strasser, M., Sreaton, E., Curewitz, D., Streiff, C., and Tobin, H., 2011. Spatial and temporal evolution of the megasplay fault in the Nankai Trough. *Geochem., Geophys., Geosyst.*, 12:Q0A008–Q0A030. doi:10.1029/2010GC003335
- Kinoshita, M., Kanamatsu, T., Kawamura, K., Sibata, T., Hamamoto, H., and Fujino, K., 2008. Heat flow distribution on the floor of Nankai Trough off Kumano and implications for the geothermal regime of subducting sediments. *JAMSTEC J. Deep-Sea Res.*, 8:13–28. http://docsrv.godac.jp/MSV2_DATA/23/JAM_RandD08_02.pdf
- Kinoshita, M., Tobin, H., Ashi, J., Kimura, G., Lallemand, S., Sreaton, E.J., Curewitz, D., Masago, H., Moe, K.T., and the Expedition 314/315/316 Scientists, 2009. *Proc. IODP, 314/315/316*: Washington, DC (Integrated Ocean Drilling Program Management International, Inc.). doi:10.2204/iodp.proc.314315316.2009
- Kodaira, S., Nakanishi, A., Park, J.-O., Ito, A., Tsuru, T., and Kaneda, Y., 2003. Cyclic ridge subduction at an inter-plate locked zone off central Japan. *Geophys. Res. Lett.*, 30(6):1339–1342. doi:10.1029/2002GL016595
- Kodaira, S., Takahashi, N., Nakanishi, A., Miura, S., and Kaneda, Y., 2000a. Subducted seamount imaged in the rupture zone of the 1946 Nankaido earthquake. *Science*, 289(5476):104–106. doi:10.1126/science.289.5476.104
- Kodaira, S., Takahashi, N., Park, J.-O., Mochizuki, K., Shinohara, M., and Kimura, S., 2000b. Western Nankai Trough seismogenic zone: results from a wide-angle ocean bottom seismic survey. *J. Geophys. Res., [Solid Earth]*, 105(B3):5887–5905. doi:10.1029/1999JB900394
- Kopf, A., Araki, E., Toczko, S., and the Expedition 332 Scientists, 2011. NanTroSEIZE Stage 2: riserless observatory. *IODP Prel. Rept.*, 332. doi:10.2204/iodp.pr.332.2011
- Lallemand, S.E., Malavieille, J., and Calassou, S., 1992. Effects of oceanic ridge subduction on accretionary wedges: experimental modeling and marine observations. *Tectonics*, 11(6):1301–1313. doi:10.1029/92TC00637
- Lallemand, S., Chamot-Rooke, N., Le Pichon, X., and Rangin, C., 1989. Zenisu Ridge: a deep intraoceanic thrust related to subduction, off southwest Japan. *Tectonophysics*, 160(1–4):151–153, 157–174. doi:10.1016/0040-1951(89)90389-2

- Lay, T., Kanamori, H., Ammon, C.J., Nettles, M., Ward, S.N., Aster, R.C., Beck, S.L., Bilek, S.L., Brudzinski, M.R., Butler, R., DeShon, H.R., Ekström, G., Satake, K., and Sipkin, S., 2005. The great Sumatra-Andaman earthquake of 26 December 2004. *Science*, 308(5725):1127–1133. doi:10.1126/science.1112250
- Le Pichon, X., Iiyama, T., Chamley, H., Charvet, J., Faure, M., Fujimoto, H., Furuta, T., Ida, Y., Kagami, H., Lallemand, S., Leggett, J., Murata, A., Okada, H., Rangin, C., Renard, V., Taira, A., and Tokuyama, H., 1987a. Nankai Trough and the fossil Shikoku Ridge: results of Box 6 Kaiko survey. *Earth Planet. Sci. Lett.*, 83(1–4):186–198. doi:10.1016/0012-821X(87)90065-3
- Le Pichon, X., Iiyama, T., Chamley, H., Charvet, J., Faure, M., Fujimoto, H., Furuta, T., Ida, Y., Kagami, H., Lallemand, S., Leggett, J., Murata, A., Okada, H., Rangin, C., Renard, V., Taira, A., and Tokuyama, H., 1987b. The eastern and western ends of Nankai Trough: results of Box 5 and Box 7 Kaiko survey. *Earth Planet. Sci. Lett.*, 83(1–4):199–213. doi:10.1016/0012-821X(87)90066-5
- Le Pichon, X., Wmamt, S., Tokuyama, H., Thoué, F., Huchon, P., and Henry, P., 1996. Structure and evolution of the backstop in the eastern Nankai Trough area (Japan): implications for the soon-to-come Tokai earthquake. *Island Arc*, 5(4):440–454. doi:10.1111/j.1440-1738.1996.tb00164.x
- Lee, C., Nott, J.A., and Keller, F.B., 2004. Seismic expression of the Cenozoic mass transport complexes, deepwater Tarfaya-Agadir Basin, offshore Morocco. *Proc.—Annu. Offshore Technol. Conf.*, 36:16741-MS. doi:10.4043/16741-MS
- Loveless, J.P., and Meade, B.J., 2010. Geodetic imaging of plate motions, slip rates, and partitioning of deformation in Japan. *J. Geophys. Res., [Solid Earth]*, 115(B2):B02410–B02445. doi:10.1029/2008JB006248
- Martin, K.M., Gulick, S.P.S., Bangs, N.L.B., Moore, G.F., Ashi, J., Park, J.-O., Kuramoto, S., and Taira, A., 2010. Possible strain partitioning structure between the Kumano fore-arc basin and the slope of the Nankai Trough accretionary prism. *Geochem., Geophys., Geosyst.*, 11:Q0AD02. doi:10.1029/2009GC002668
- Mazzotti, S., Henry, P., and Le Pichon, X., 2001. Transient and permanent deformation of central Japan estimated by GPS: 2. Strain partitioning and arc–arc collision. *Earth Planet. Sci. Lett.*, 184(2):455–469. doi:10.1016/S0012-821X(00)00336-8
- Mazzotti, S., Lallemand, S.J., Henry, P., Le Pichon, X., Tokuyama, H., and Takahashi, N., 2002. Intraplate shortening and underthrusting of a large basement ridge in the eastern Nankai subduction zone. *Mar. Geol.*, 187(1–2):63–88. doi:10.1016/S0025-3227(02)00245-1
- Mazzotti, S., Le Pichon, X., Henry, P., and Miyazaki, S.-I., 2000. Full interseismic locking of the Nankai and Japan-West Kuril subduction zones: an analysis of uniform elastic strain accumulation in Japan constrained by permanent GPS. *J. Geophys. Res., [Solid Earth]*, 105(B6):13159–13178. doi:10.1029/2000JB900060
- Miyazaki, S., and Heki, K., 2001. Crustal velocity field of southwest Japan: subduction and arc-arc collision. *J. Geophys. Res., [Solid Earth]*, 106(B3):4305–4326. doi:10.1029/2000JB900312
- Moore, G.F., Bangs, N.L., Taira, A., Kuramoto, S., Pangborn, E., and Tobin, H.J., 2007. Three-dimensional splay fault geometry and implications for tsunami generation. *Science*, 318(5853):1128–1131. doi:10.1126/science.1147195
- Moore, G.F., Park, J.-O., Bangs, N.L., Gulick, S.P., Tobin, H.J., Nakamura, Y., Sato, S., Tsuji, T., Yoro, T., Tanaka, H., Uraki, S., Kido, Y., Sanada, Y., Kuramoto, S., and Taira, A., 2009. Structural and seismic stratigraphic framework of the NanTroSEIZE Stage 1 transect. In Kinoshita, M., Tobin, H., Ashi, J., Kimura, G., Lallemand, S., Sreaton, E.J., Curewitz, D.,

- Masago, H., Moe, K.T., and the Expedition 314/315/316 Scientists, *Proc. IODP*, 314/315/316: Washington, DC (Integrated Ocean Drilling Program Management International, Inc.). doi:10.2204/iodp.proc.314315316.102.2009
- Moore, G.F., Taira, A., Klaus, A., Becker, L., Boeckel, B., Cragg, B.A., Dean, A., Fergusson, C.L., Henry, P., Hirano, S., Hisamitsu, T., Hunze, S., Kastner, M., Maltman, A.J., Morgan, J.K., Murakami, Y., Saffer, D.M., Sánchez-Gómez, M., Screaton, E.J., Smith, D.C., Spivack, A.J., Steurer, J., Tobin, H.J., Ujiie, K., Underwood, M.B., and Wilson, M., 2001. New insights into deformation and fluid flow processes in the Nankai Trough accretionary prism: results of Ocean Drilling Program Leg 190. *Geochem., Geophys., Geosyst.*, 2(10):1058. doi:10.1029/2001GC000166
- Moore, G.F., Taira, A., Klaus, A., et al., 2001. *Proc. ODP, Init. Repts.*, 190: College Station, TX (Ocean Drilling Program). doi:10.2973/odp.proc.ir.190.2001
- Moore, J.C., and Saffer, D., 2001. Updip limit of the seismogenic zone beneath the accretionary prism of southwest Japan: an effect of diagenetic to low-grade metamorphic processes and increasing effective stress. *Geology*, 29(2):183–186. doi:10.1130/0091-7613(2001)029<0183:ULOTSZ>2.0.CO;2
- Nakanishi, A., Takahashi, N., Park, J.-O., Miura, S., Kodaira, S., Kaneda, Y., Hirata, N., Iwasaki, T., and Nakamura, M., 2002. Crustal structure across the coseismic rupture zone of the 1944 Tonankai earthquake, the central Nankai Trough seismogenic zone. *J. Geophys. Res.*, 107(B1):2007. doi:10.1029/2001JB000424
- Obana, K., Kodaira, S., and Kaneda, Y., 2004. Microseismicity around rupture area of the 1944 Tonankai earthquake from ocean bottom seismograph observations. *Earth Planet. Sci. Lett.*, 222(2):561–572. doi:10.1016/j.epsl.2004.02.032
- Obara, K., and Ito, Y., 2005. Very low frequency earthquakes excited by the 2004 off the Kii Peninsula earthquakes: a dynamic deformation process in the large accretionary prism. *Earth, Planets Space*, 57(4):321–326.
- Okino, K., Shimakawa, Y., and Nagaoka, S., 1994. Evolution of the Shikoku Basin. *J. Geomagn. Geoelectr.*, 46(6):463–479.
- Park, J.-O., Moore, G.F., Tsuru, T., Kodaira, S., and Kaneda, Y., 2004. A subducted oceanic ridge influencing the Nankai megathrust earthquake rupture. *Earth Planet. Sci. Lett.*, 217(1–2):77–84. doi:10.1016/S0012-821X(03)00553-3
- Park, J.-O., Tsuru, T., Kaneda, Y., Kono, Y., Kodaira, S., Takahashi, N., and Kinoshita, H., 1999. A subducting seamount beneath the Nankai accretionary prism off Shikoku, southwestern Japan. *Geophys. Res. Lett.*, 26(7):931–934. doi:10.1029/1999GL900134
- Park, J.-O., Tsuru, T., Kodaira, S., Cummins, P.R., and Kaneda, Y., 2002. Splay fault branching along the Nankai subduction zone. *Science*, 297(5584):1157–1160. doi:10.1126/science.1074111
- Park, J.-O., Tsuru, T., No, T., Takizawa, K., Sato, S., and Kaneda, Y., 2008. High-resolution 3D seismic reflection survey and prestack depth imaging in the Nankai Trough off southeast Kii Peninsula. *Butsuri Tansa*, 61:231–241. (in Japanese, with abstract in English)
- Ruff, L., and Kanamori, H., 1983. Seismic coupling and uncoupling at subduction zones. *Tectonophysics*, 99(2–4):99–117. doi:10.1016/0040-1951(83)90097-5
- Saffer, D., McNeill, L., Byrne, T., Araki, E., Toczko, S., Eguchi, N., Takahashi, K., and the Expedition 319 Scientists, 2010. *Proc. IODP*, 319: Tokyo (Integrated Ocean Drilling Program Management International, Inc.). doi:10.2204/iodp.proc.319.2010
- Saffer, D.M., and Marone, C., 2003. Comparison of smectite- and illite-rich gouge frictional properties: application to the updip limit of the seismogenic zone along subduction

- megathrusts. *Earth Planet. Sci. Lett.*, 215(1–2):219–235. doi:10.1016/S0012-821X(03)00424-2
- Saffer, D.M., and McKiernan, A.W., 2009. Evaluation of in situ smectite dehydration as a pore water freshening mechanism in the Nankai Trough, offshore southwest Japan. *Geochem., Geophys., Geosyst.*, 10(2):Q02010. doi:10.1029/2008GC002226
- Saffer, D.M., Underwood, M.B., and McKiernan, A.W., 2008. Evaluation of factors controlling smectite transformation and fluid production in subduction zones: application to the Nankai Trough. *Isl. Arc*, 17(2):208–230. doi:10.1111/j.1440-1738.2008.00614.x
- Saito, S., Underwood, M.B., and Kubo, Y., 2009. NanTroSEIZE Stage 2: subduction inputs. *IODP Sci. Prosp.*, 322. doi:10.2204/iodp.sp.322.2009
- Saito, S., Underwood, M.B., and Kubo, Y., and the Expedition 322 Scientists, 2010. *Proc. IODP, 322: Tokyo (Integrated Ocean Drilling Program Management International, Inc.)*. doi:10.2204/iodp.proc.322.2010
- Satoguchi, Y., Higuchi, Y., and Kurokawa, K., 2005. Correlation of the Ohta tephra bed in the Tokai group with a tephra in the Miura group, central Japan. *Chishitsugaku Zasshi*, 111(2):74–86.
- Schnellmann, M., Anselmetti, F.S., Giardini, D., and McKenzie, J.A., 2005. Mass movement-induced fold-and-thrust belt structures in unconsolidated sediments in Lake Lucerne (Switzerland). *Sedimentology*, 52(2):271–289. doi:10.1111/j.1365-3091.2004.00694.x
- Screaton, E.J., Kimura, G., Curewitz, D., and the Expedition 316 Scientists, 2009. Expedition 316 summary. In Kinoshita, M., Tobin, H., Ashi, J., Kimura, G., Lallemand, S., Screaton, E.J., Curewitz, D., Masago, H., Moe, K.T., and the Expedition 314/315/316 Scientists, *Proc. IODP, 314/315/316: Washington, DC (Integrated Ocean Drilling Program Management International, Inc.)*. doi:10.2204/iodp.proc.314315316.131.2009
- Scudder, R.P., Murray, R.W., and Plank, T., 2009. Dispersed ash in deeply buried sediment from the northwest Pacific Ocean: an example from the Izu-Bonin arc (ODP Site 1149). *Earth Planet. Sci. Lett.*, 284(3–4):639–648. doi:10.1016/j.epsl.2009.05.037
- Seno, T., Stein, S., and Gripp, A.E., 1993. A model for the motion of the Philippine Sea plate consistent with NUVEL-1 and geological data. *J. Geophys. Res., [Solid Earth]*, 98(B10):17941–17948. doi:10.1029/93JB00782
- Solheim, A., Berg, K., Forsberg, C.F., and Bryn, P., 2005. The Storegga Slide complex: repetitive large scale sliding with similar cause and development. In Solheim, A., Bryn, P., Berg, K., and Mienert, J. (Eds.), *Ormen Lange—an Integrated Study for the Safe Development of a Deep-Water Gas Field within the Storegga Slide Complex, NE Atlantic Continental Margin*. *Mar. Pet. Geol.*, 22(1–2):97–107. doi:10.1016/j.marpetgeo.2004.10.013
- Spinelli, G.A., Mozley, P.S., Tobin, H.J., Underwood, M.B., Hoffman, N.W., and Bellew, G.M., 2007. Diagenesis, sediment strength, and pore collapse in sediment approaching the Nankai Trough subduction zone. *Geol. Soc. Am. Bull.*, 119(3–4):377–390. doi:10.1130/B25920.1
- Spinelli, G.A., and Underwood, M.B., 2005. Modeling thermal history of subducting crust in Nankai Trough: constraints from in situ sediment temperature and diagenetic reaction progress. *Geophys. Res. Lett.*, 32(9):L09301. doi:10.1029/2005GL022793
- Spinelli, G.A., and Wang, K., 2008. Effects of fluid circulation in subduction crust on Nankai margin seismogenic zone temperatures. *Geology*, 36(11):887–890. doi:10.1130/G25145A.1

- Strasser, M., Moore, G.F., Kimura, G., Kitamura, Y., Kopf, A.J., Lallemand, S., Park, J.-O., Sreaton, E.J., Su, X., Underwood, M.B., and Zhao, X., 2009. Origin and evolution of a splay fault in the Nankai accretionary wedge. *Nat. Geosci.*, 2(9):648–652. [doi:10.1038/ngeo609](https://doi.org/10.1038/ngeo609)
- Strasser, M., Moore, G., Kimura, G., Kopf, A., Underwood, M., Guo, J., and Sreaton, E., 2011. Slumping and mass-transport deposition in the Nankai forearc: evidence from IODP drilling and 3-D reflection seismic data. *Geochem., Geophys., Geosyst.* 12:Q0AD13. [doi:10.1029/2010GC003431](https://doi.org/10.1029/2010GC003431)
- Taylor, S.R., and McLennan, S.M., 1985. *The Continental Crust: Its Composition and Evolution*: Oxford (Blackwell Scientific).
- Tobin, H.J., and Kinoshita, M., 2006a. Investigations of seismogenesis at the Nankai Trough, Japan. *IODP Sci. Prosp.*, NanTroSEIZE Stage 1. [doi:10.2204/iodp.sp.nantroseite1.2006](https://doi.org/10.2204/iodp.sp.nantroseite1.2006)
- Tobin, H.J., and Kinoshita, M., 2006b. NanTroSEIZE: the IODP Nankai Trough Seismogenic Zone Experiment. *Sci. Drill.*, 2:23–27. [doi:10.2204/iodp.sd.2.06.2006](https://doi.org/10.2204/iodp.sd.2.06.2006)
- Underwood, M.B., 2007. Sediment inputs to subduction zones: why lithostratigraphy and clay mineralogy matter. In Dixon, T., and Moore, J.C. (Eds.), *The Seismogenic Zone of Subduction Thrust Faults*: New York (Columbia Univ. Press), 42–85.
- Underwood, M.B., Saito, S., Kubo, Y., and the Expedition 322 Scientists, 2010. Expedition 322 summary. In Saito, S., Underwood, M.B., and Kubo, Y., and the Expedition 322 Scientists, *Proc. IODP, 322*: Tokyo (Integrated Ocean Drilling Program Management International, Inc.). [doi:10.2204/iodp.proc.322.101.2010](https://doi.org/10.2204/iodp.proc.322.101.2010)
- Wang, K., and Hu, Y., 2006. Accretionary prisms in subduction earthquake cycles: the theory of dynamic Coulomb wedge. *J. Geophys. Res., [Solid Earth]*, 111(B6):B06410. [doi:10.1029/2005JB004094](https://doi.org/10.1029/2005JB004094)
- Yamano, M., Kinoshita, M., Goto, S., and Matsubayashi, O., 2003. Extremely high heat flow anomaly in the middle part of the Nankai Trough. *Phys. Chem. Earth*, 28(9–11):487–497. [doi:10.1016/S1474-7065\(03\)00068-8](https://doi.org/10.1016/S1474-7065(03)00068-8)
- Yoshikawa, S., and Mitamura, M., 1999. Quaternary stratigraphy of the Osaka Plain, central Japan and its correlation with oxygen isotope record from deep sea cores. *Chishitsugaku Zasshi*, 105(5):332–340. (in Japanese with English abstract).

Expedition 333 Preliminary Report

Table T1. Expedition 333 coring summary. (See table note.)

Hole	Latitude	Longitude	Water depth (mbsl)	Cores (N)	Cored (m)	Recovered (m)	Recovery (%)	Drilled (m)	Penetration (m)	Time on site (days)
333-										
C0018A	33°09.4195'N	136°40.8888'E	3084.35	36	314.15	271.44	86.4	314.15	314.15	8
C0011C	32°49.7436'N	136°52.9250'E	4050.5	3	22.5	22.99	102.2	22.5	22.5	1
C0011D	32°49.7436'N	136°52.9250'E	4050.5	52	359	351.49	97.9	380	380	6
C0012C	32°44.8947'N	136°55.0417'E	3510.5	15	124.5	128.62	103.3	124.5	124.5	2
C0012D	32°44.9001'N	136°55.0418'E	3510.5	13	63.8	66.38	104	180	180	1
C0012E	32°44.9001'N	136°55.0418'E	3510.5	3	28.5	13.85	48.6	528.5	528.5	2
C0012F	32°44.8815'N	136°55.0066'E	3510.5	2	5.5	2.65	48.2	525.5	525.5	4
C0012G	32°44.8848'N	136°55.0153'E	3510.5	15	115.5	25.92	22.4	630.5	630.5	4
Expedition 333 totals:				139	1033.45	883.34	76.625	2705.65	2705.65	28

Note: N = number.

Figure F1. Bathymetric map, with 2-D MCS profile locations, NanTroSEIZE Stage 1 and 2 drill sites (white circles), and Expedition 333 drill sites (red circles). White barbed line = position of deformation front of accretionary prism, yellow arrow = estimated far-field vectors between Philippine Sea plate and Japan (Seno et al. 1993; Heki, 2007).

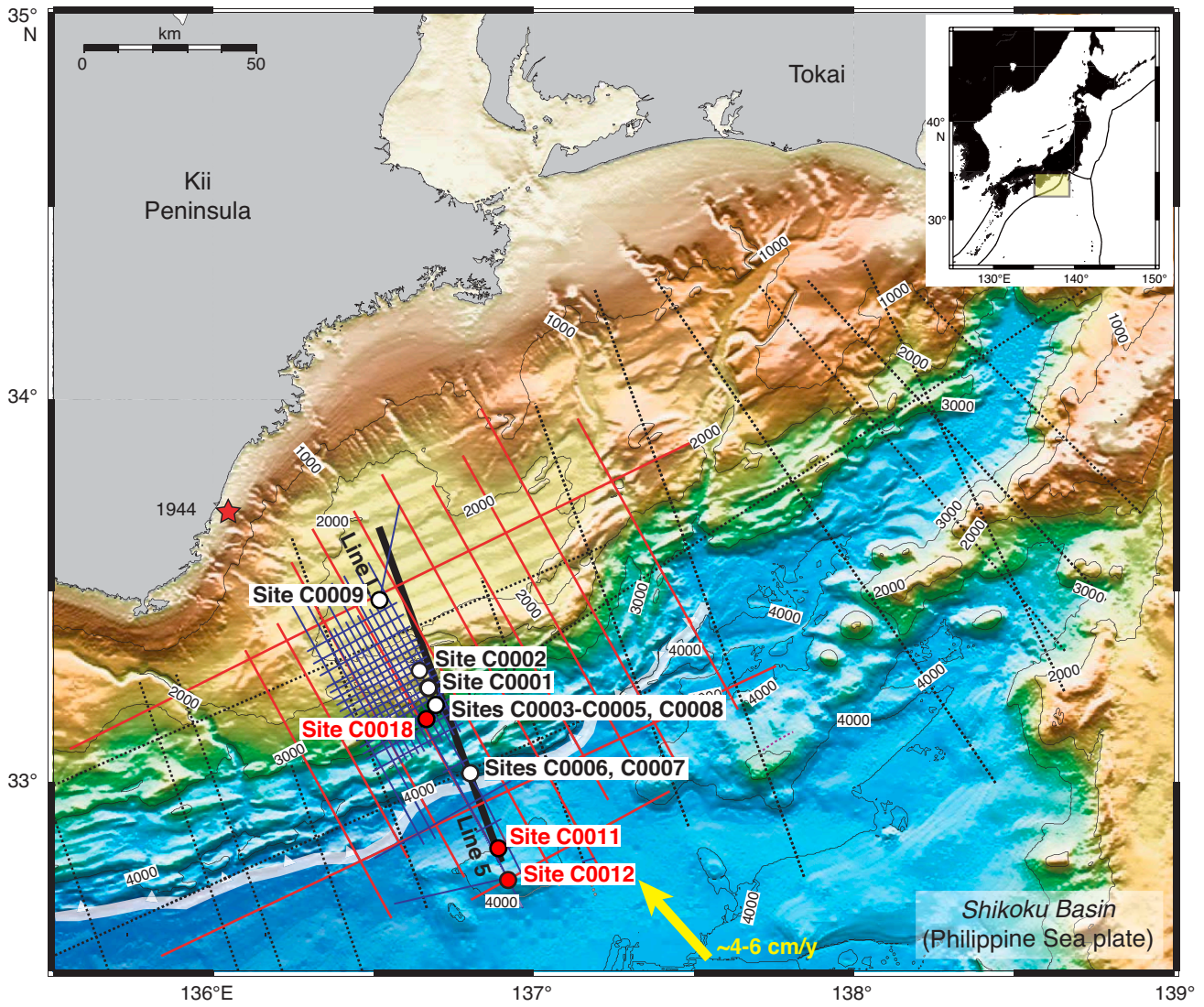


Figure F2. Spliced composite profile of a representative depth section from NanTroSEIZE 3-D data volume (Moore et al., 2009) and Line 95 from IFREE mini-3-D seismic survey (Park et al., 2008). Projected positions of Stage 1 and 2 drilling sites, including Sites C0018, C0011, and C0012, are shown.

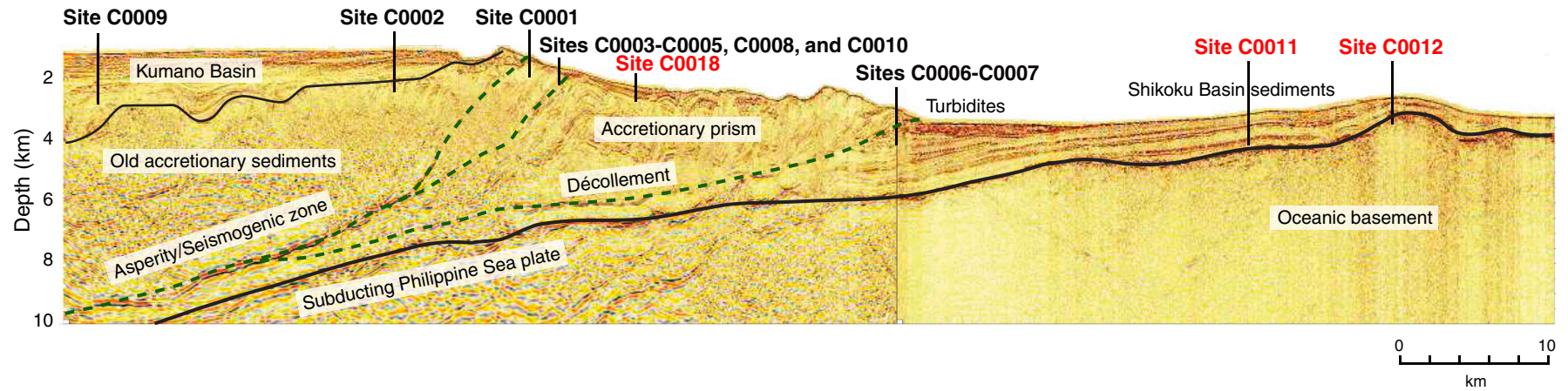


Figure F3. Detailed bathymetry and structure around Site C0018 at the footwall of the splay fault (Strasser et al., 2011). Block diagram and MCS cross-lines (XLs). IL = in-line. VE = vertical exaggeration.

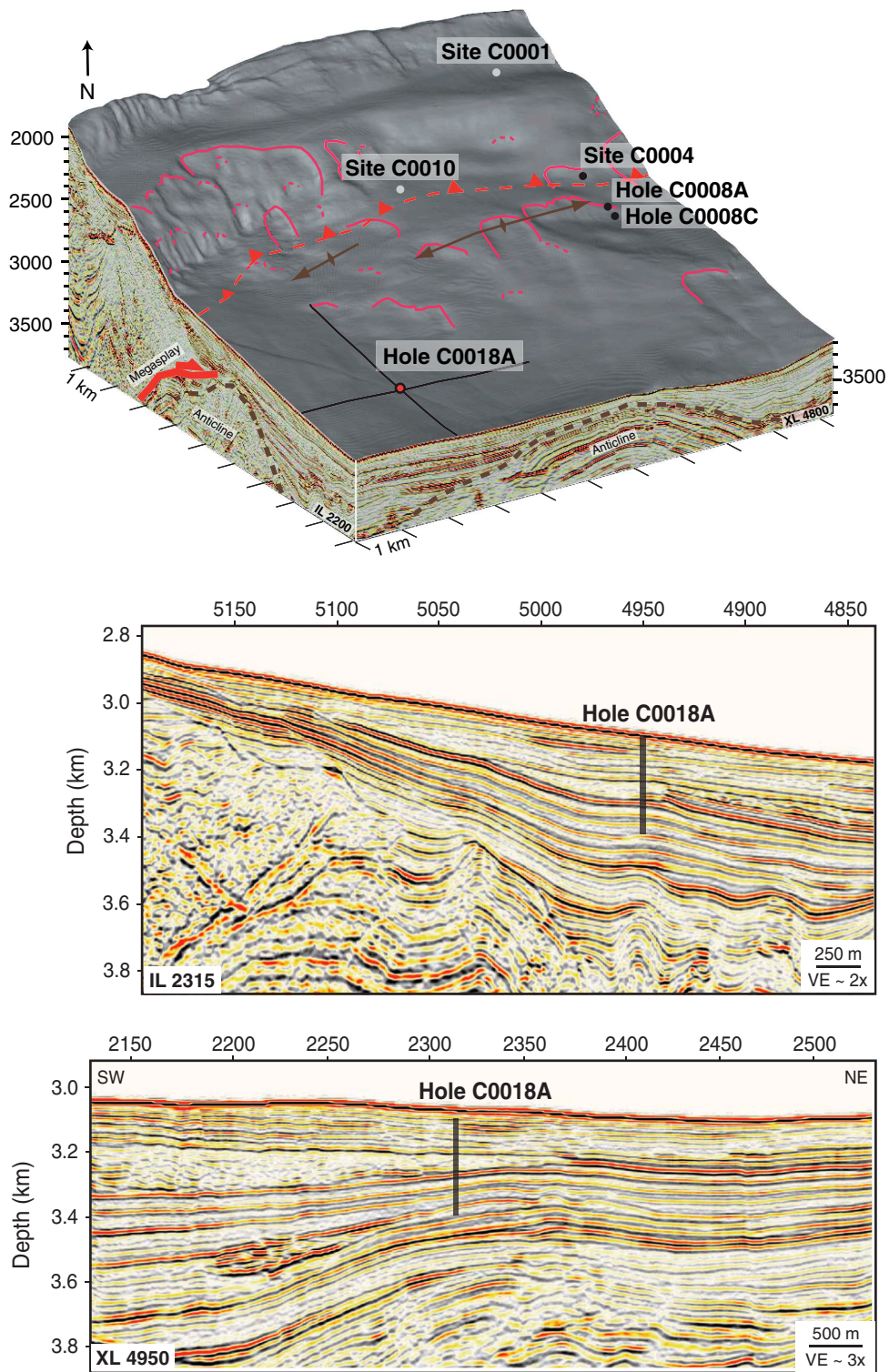


Figure F4. Schematic sedimentary log, Hole C00018A. MTD = mass transport deposit. FO = first occurrence, LO = last occurrence, LCO = last consistent occurrence, FCO = first consistent occurrence.

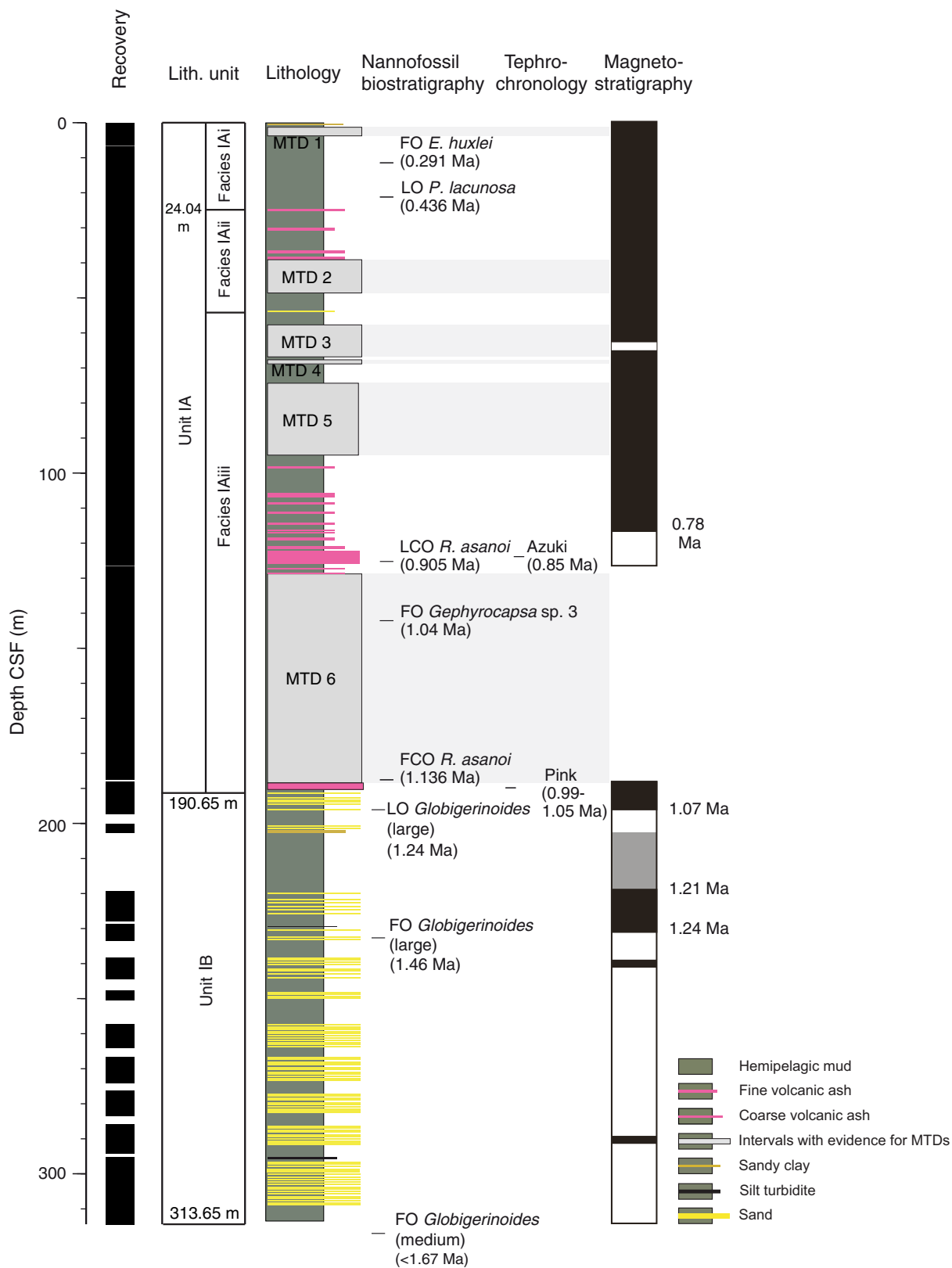


Figure F5. Top of MTD 2 showing chaotic facies and overlying turbidite. **A.** Core photo. **B.** Computed tomography (CT) scan. **C.** CT scan 3-D rendering.

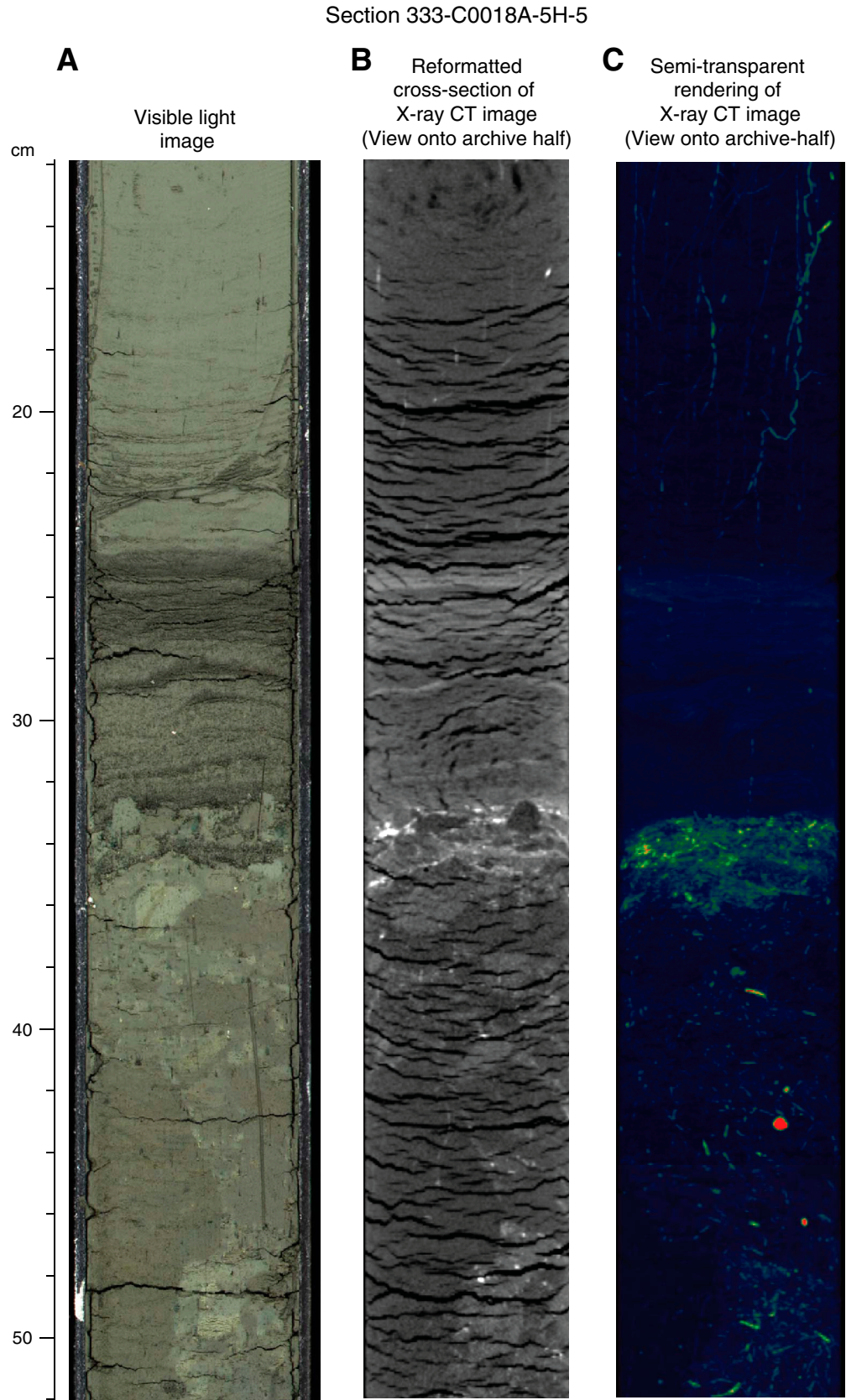


Figure F6. Shear zone at base of MTD 2. **A.** Core photo. **B.** Computed tomography (CT) scan. **C.** CT scan 3-D rendering showing high CT pyrite lines.

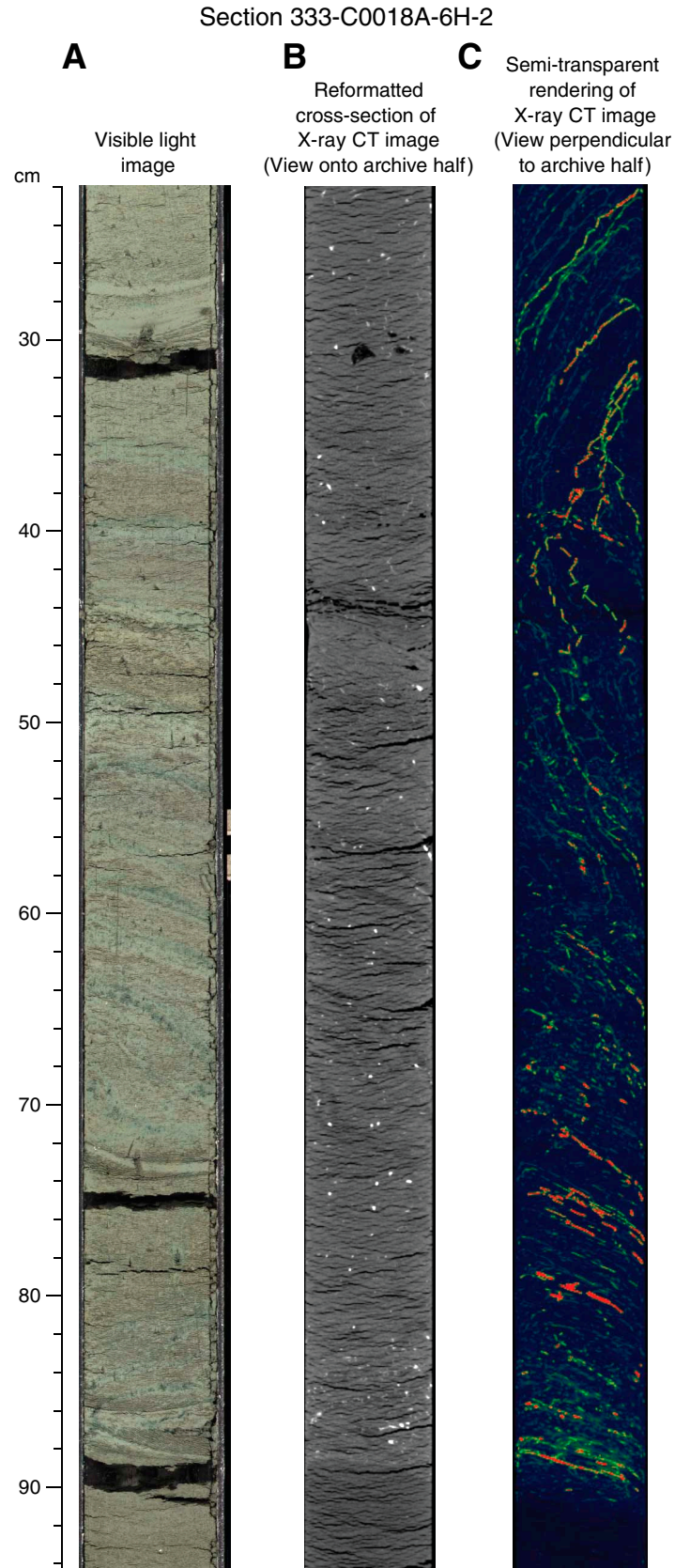


Figure F7. A. Core photo of a fluidized ash layer, corresponding to MTD 4, Subunit IA. B. Core photo of volcaniclastic layer, corresponding to Azuki volcanic event. C. Detail of Azuki volcaniclastic sand (Section 333-C0018A-14H-8, 46 cm). This sand is composed of pumice, volcanic lithic fragments, metamorphic lithic fragments, quartz, feldspar, and foraminifers. D. Smear slide photo of Azuki volcaniclastic sand (Section 333-C0018A-14H-8, 77 cm). This ash is mainly composed of volcanic glass shards with minor amounts of hornblende, orthopyroxene, and clinopyroxene. At the center of the photo an obsidian fragment is visible. E. Smear slide photo of volcanic ash corresponding to Pink volcanic event (Section 333-C0018A-23H-3, 49 cm). This ash is mainly composed of bubble wall volcanic glass shards and minor amount of hornblende.

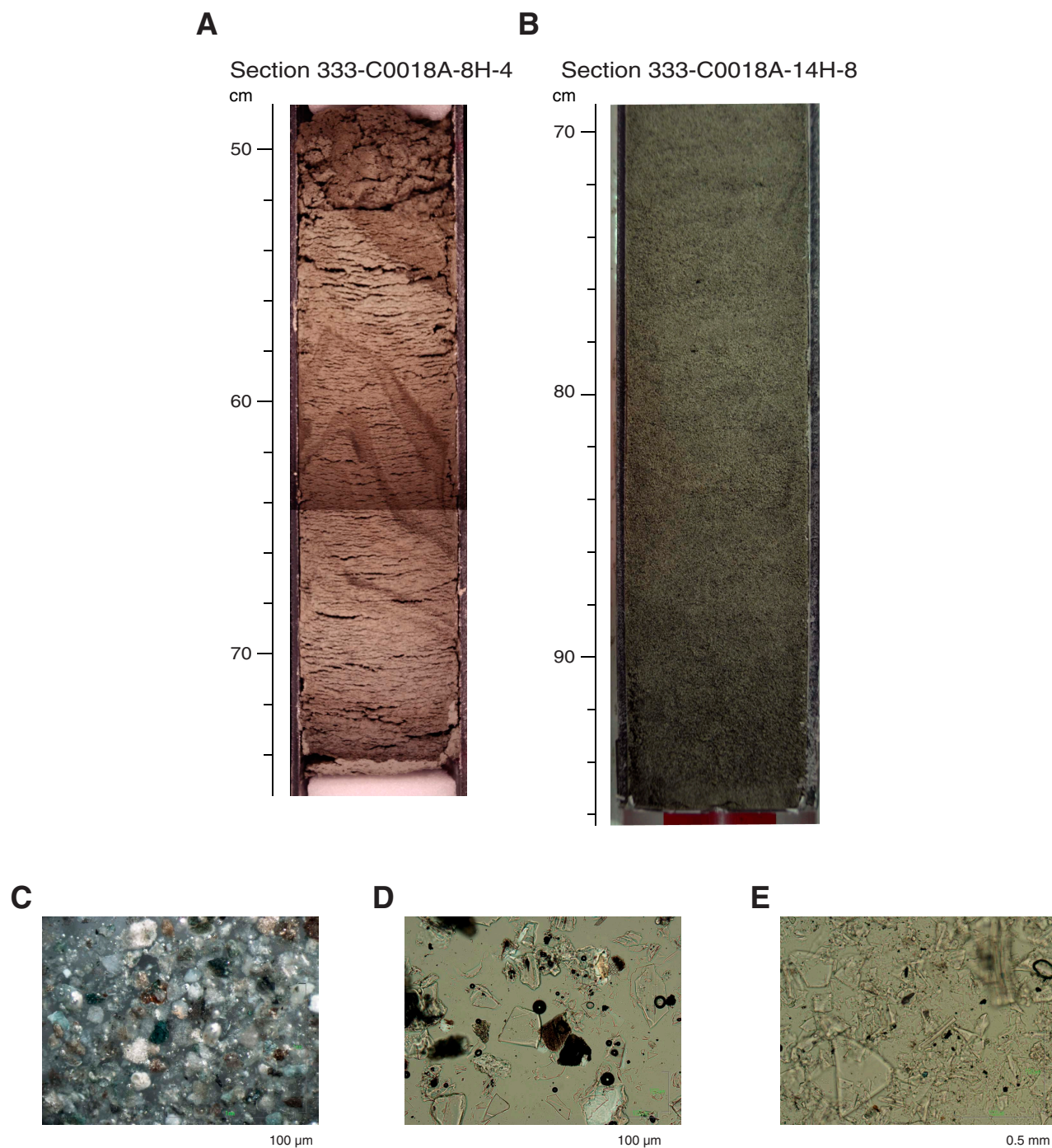


Figure F8. Photos showing chaotic style of internal deformation in MTD 6.

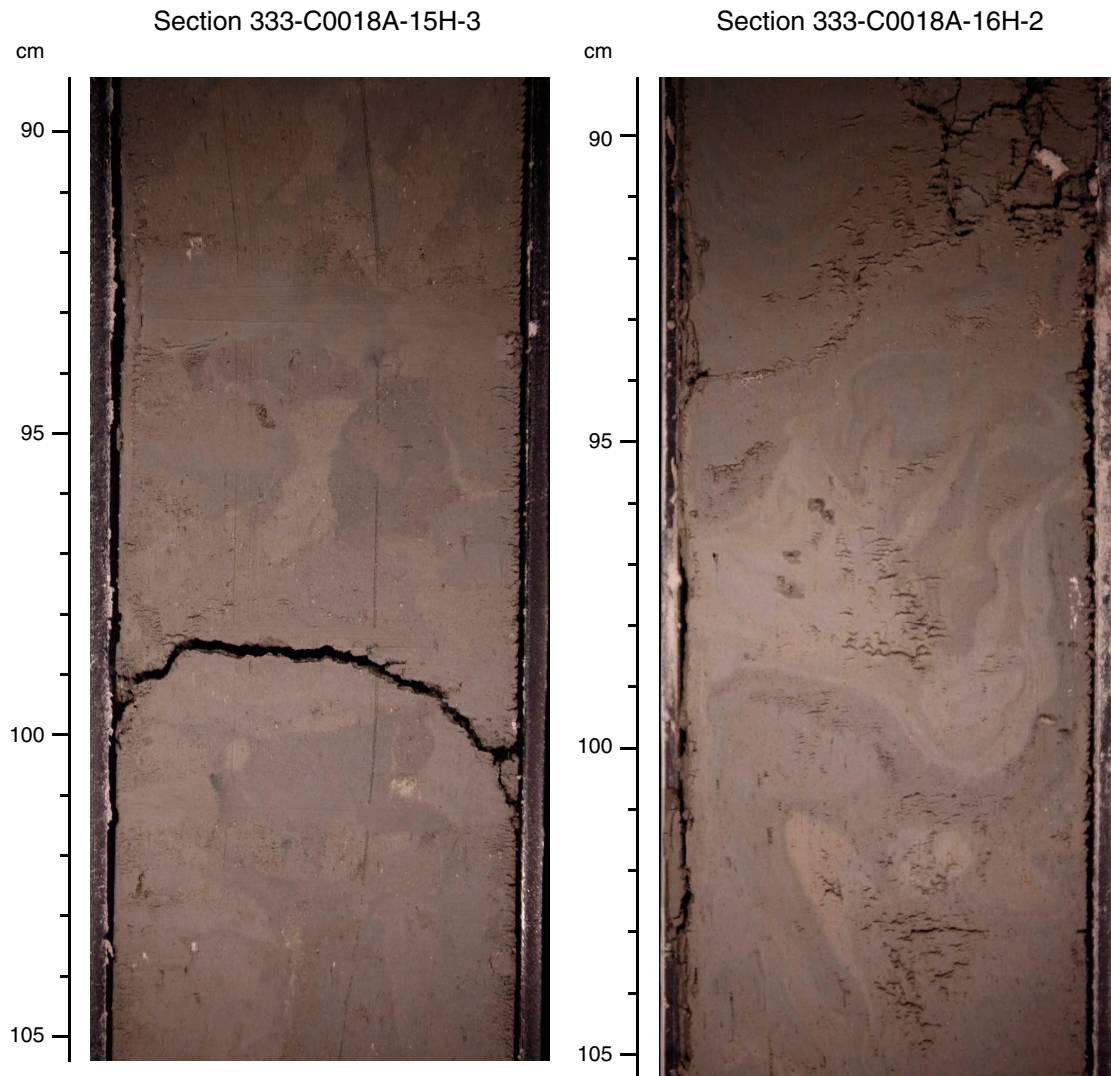
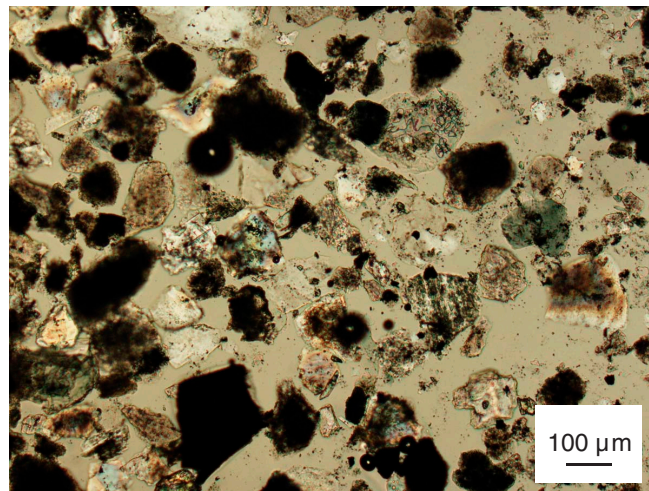


Figure F9. A. Core photo from a cyclic succession of turbidites showing fining-upward trends. B. Smear slide denoting sand and lithic grains in the turbidite succession. C. Detail showing erosion at base of turbidite deposits occurring in Subunit IB.

A Section 333-C0018A-25T-2



B Section 333-C0018A-29T-4, 114 cm



C Section 333-C0018A-29T-4

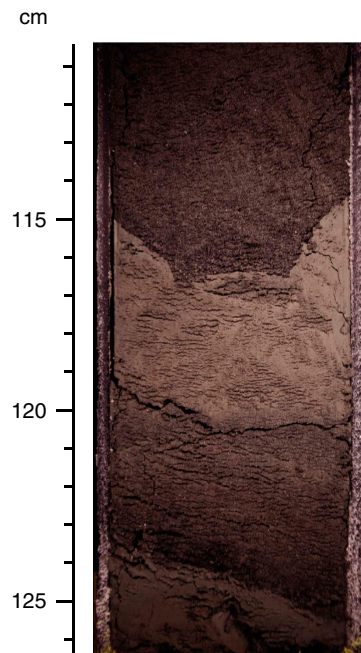


Figure F10. Summary of XRD data, Hole C0018A. Unit and facies boundaries are highlighted. Note the sharp Subunit IA/IB boundary observed on XRD data. MTD = mass transport deposit.

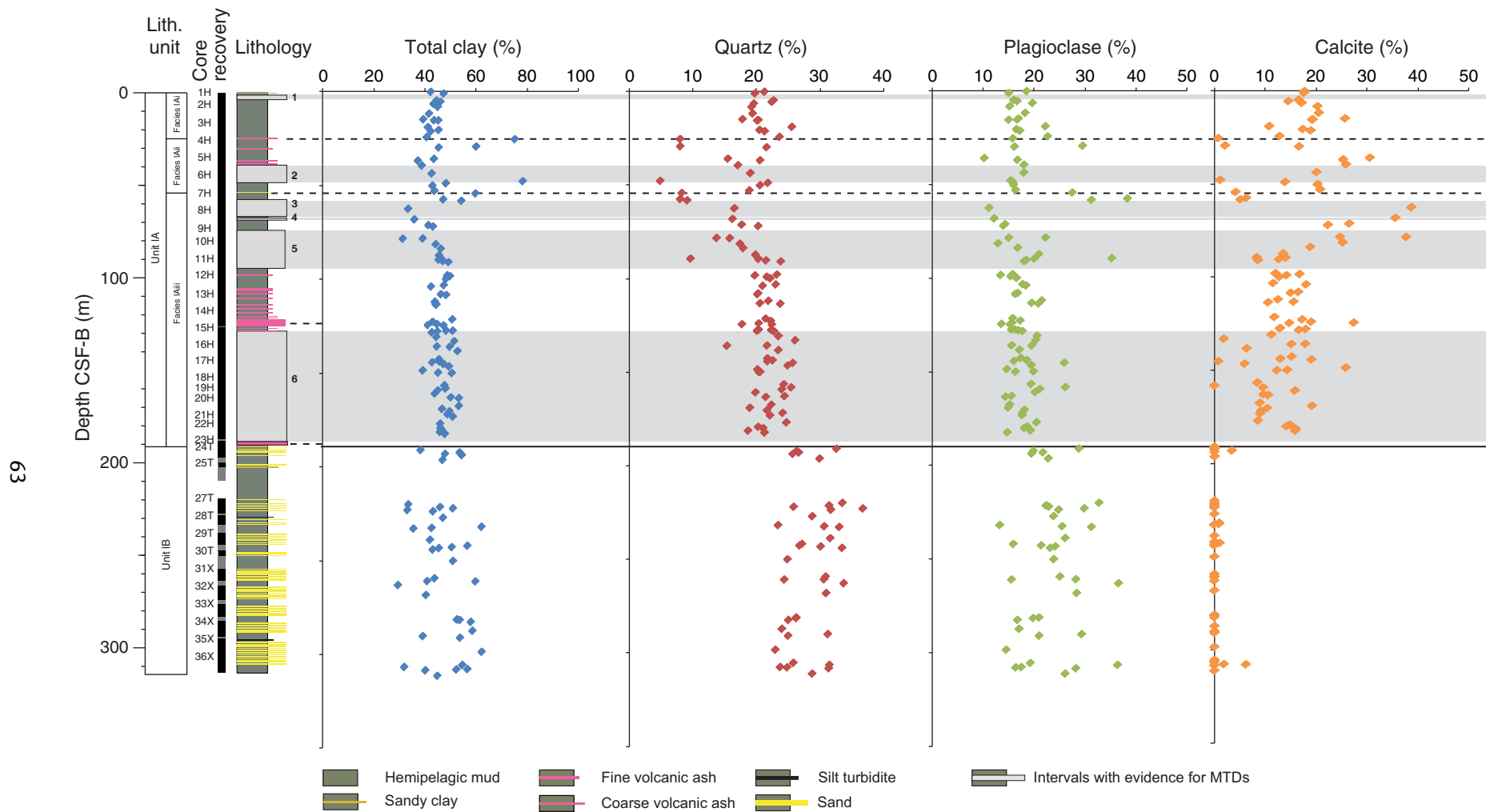


Figure F11. Variations of SiO₂, Al₂O₃, CaO, Fe₂O₃, MgO, and TiO₂ contents as a function of depth from XRF analysis from Holes C0011C and C0011D (red) and Expedition 322 Hole C0011B (yellow). MTD = mass transport deposit.

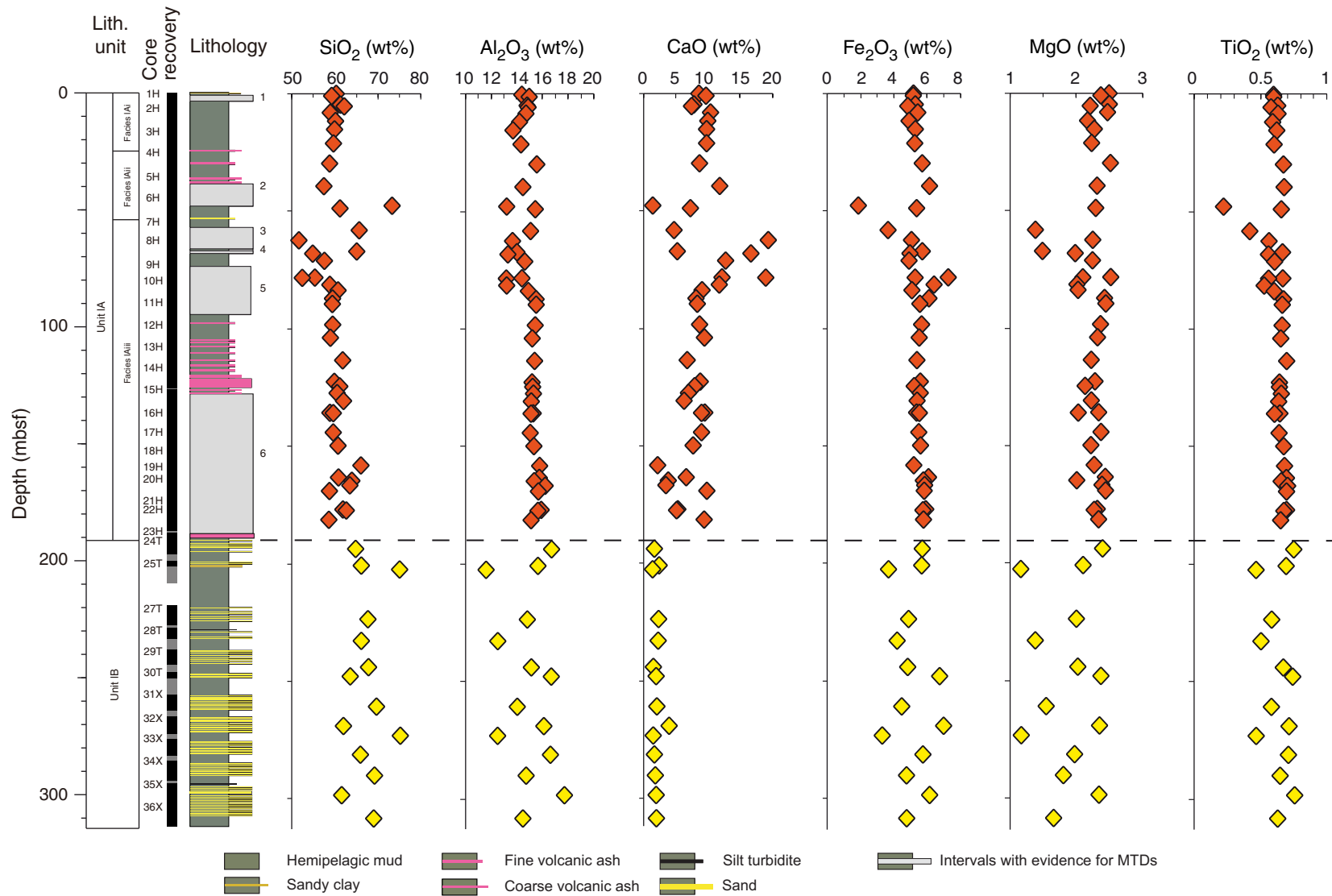


Figure F12. Distribution of bedding dip angles and deformation structures with depth. Orange bands = depth range of mass transport deposits (MTDs).

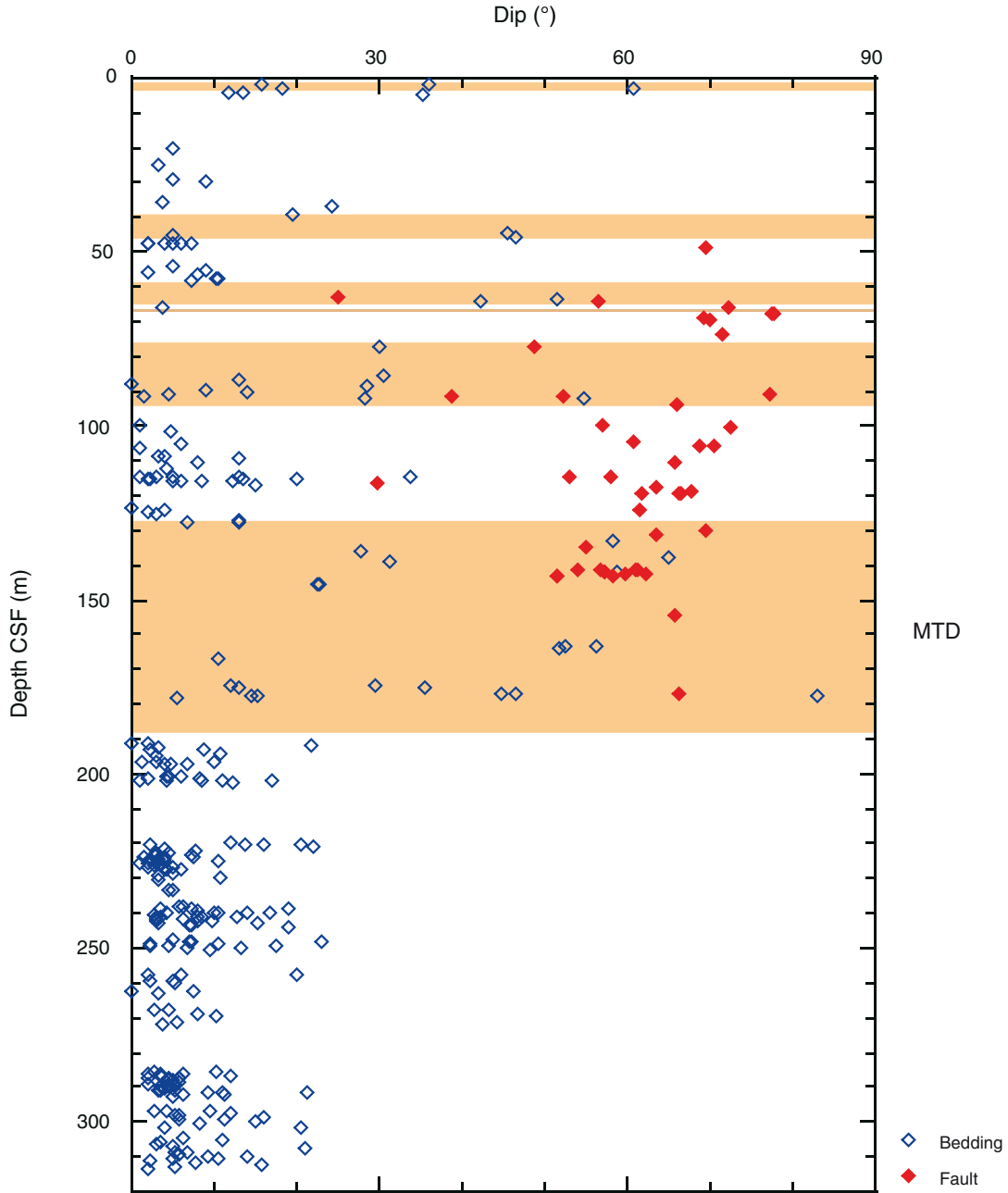


Figure F13. Lower-hemisphere equal-area projections. **A.** Poles to bedding above MTD. **B.** Poles to fault above MTD. **C.** Poles to folded bedding plane (black circles) and fold axis (green triangle) of slump fold (Fig. F14). **D.** Poles to bedding and fissility below MTD.

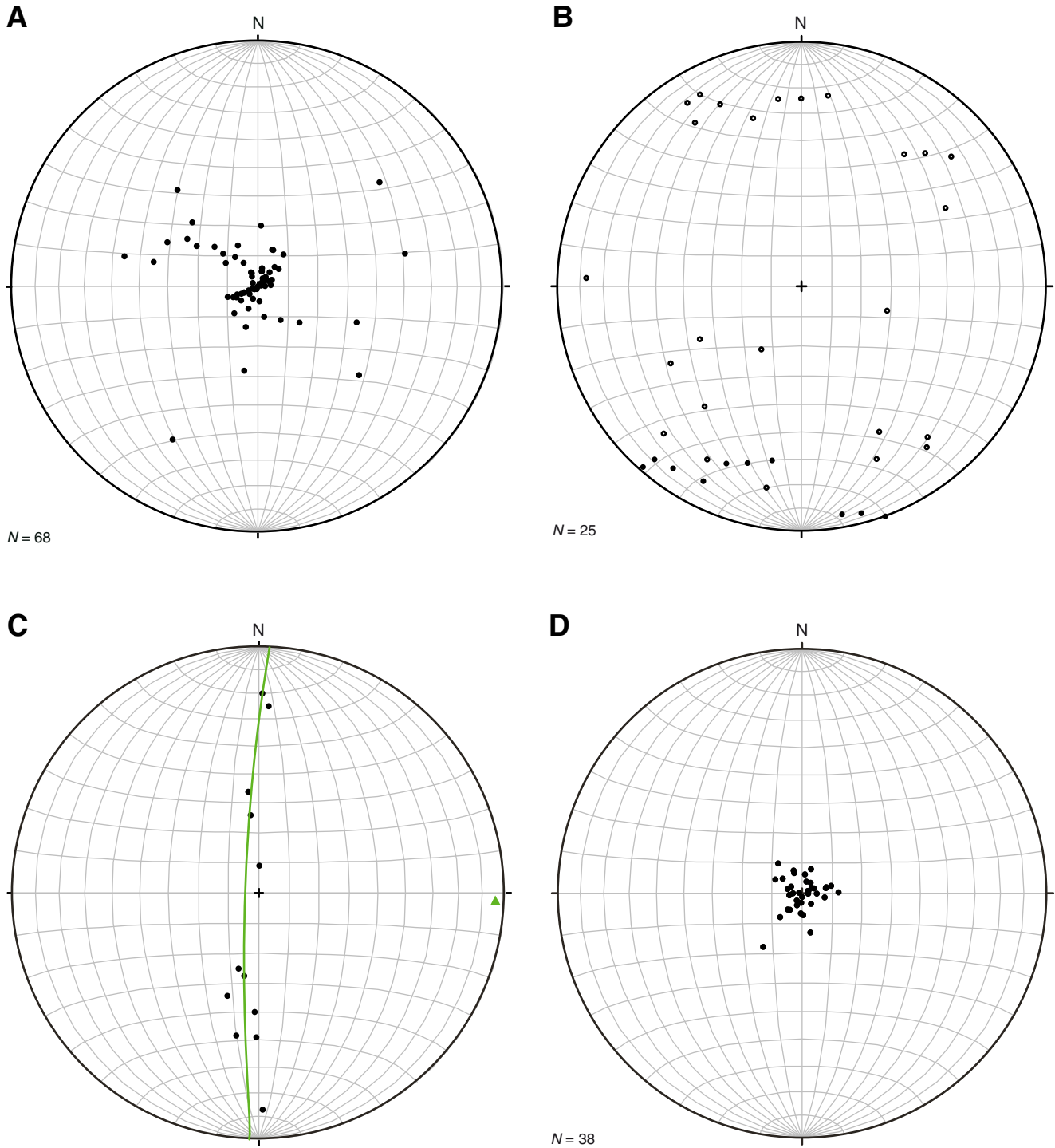


Figure F14. Appearance of slump fold (interval 333-C0018A-5H-6, 73–88 cm) on core photo (left) and CT scan (right) image.

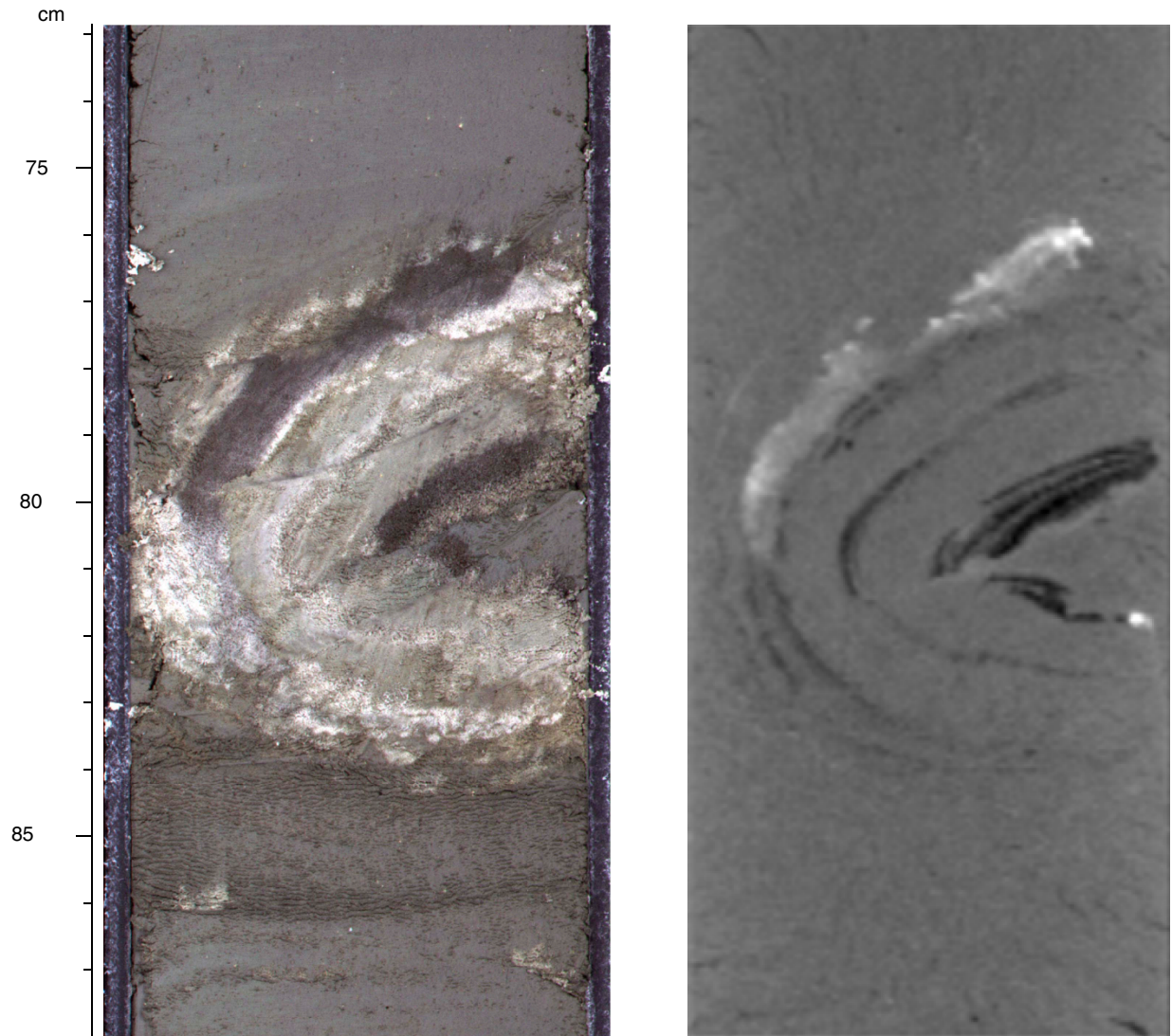


Figure F15. Appearance of shear zone (interval 333-C0018A-17H-6, 53–76 cm) on core photo (left) and CT scan (right) image. Red triangles = location of shear zones.

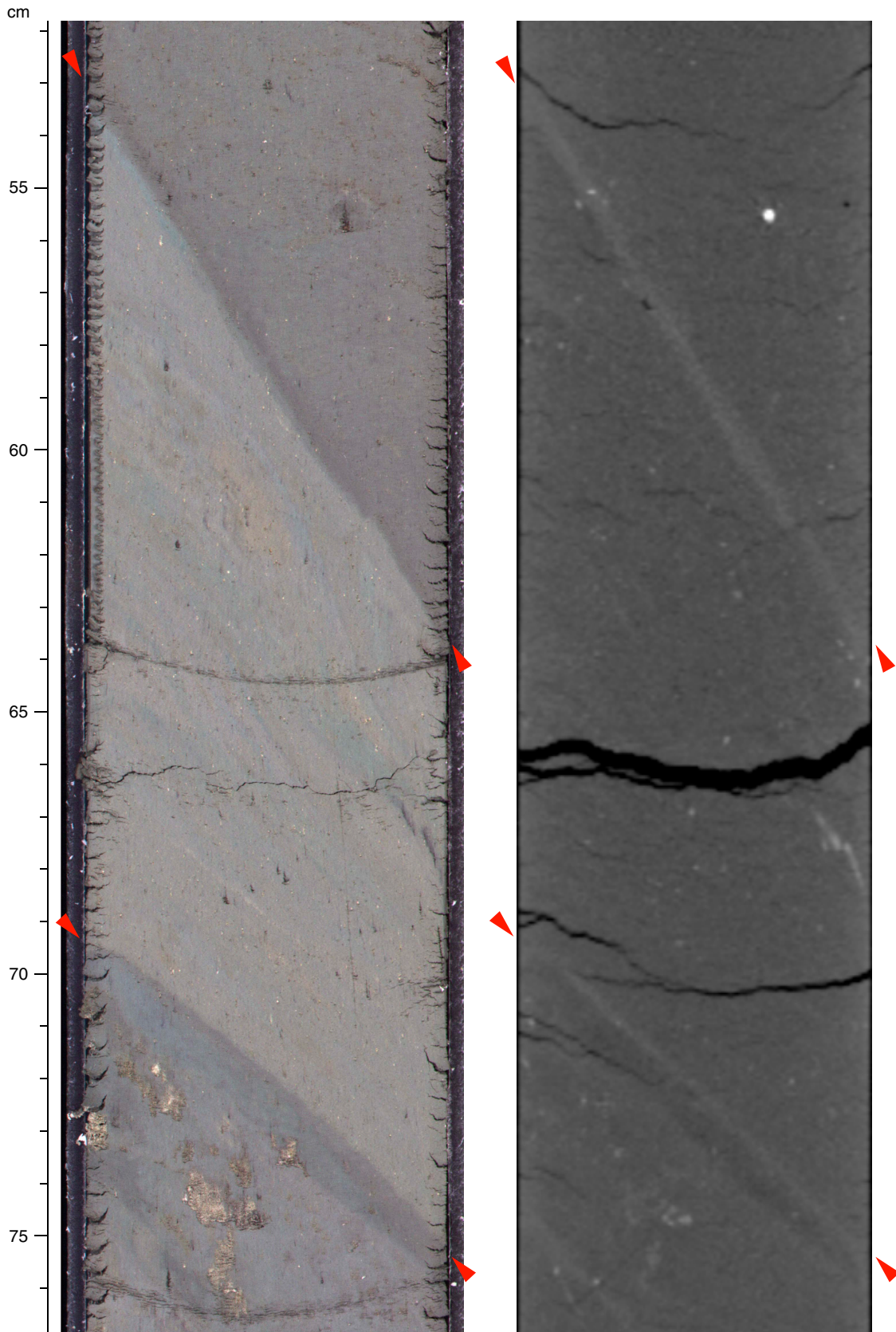


Figure F16. Summary of physical properties, porosity, shear strength, and resistivity, Site C0018. MTD = mass transport deposit. For porosity, blue = mud/silt samples, red = sand/ash samples.

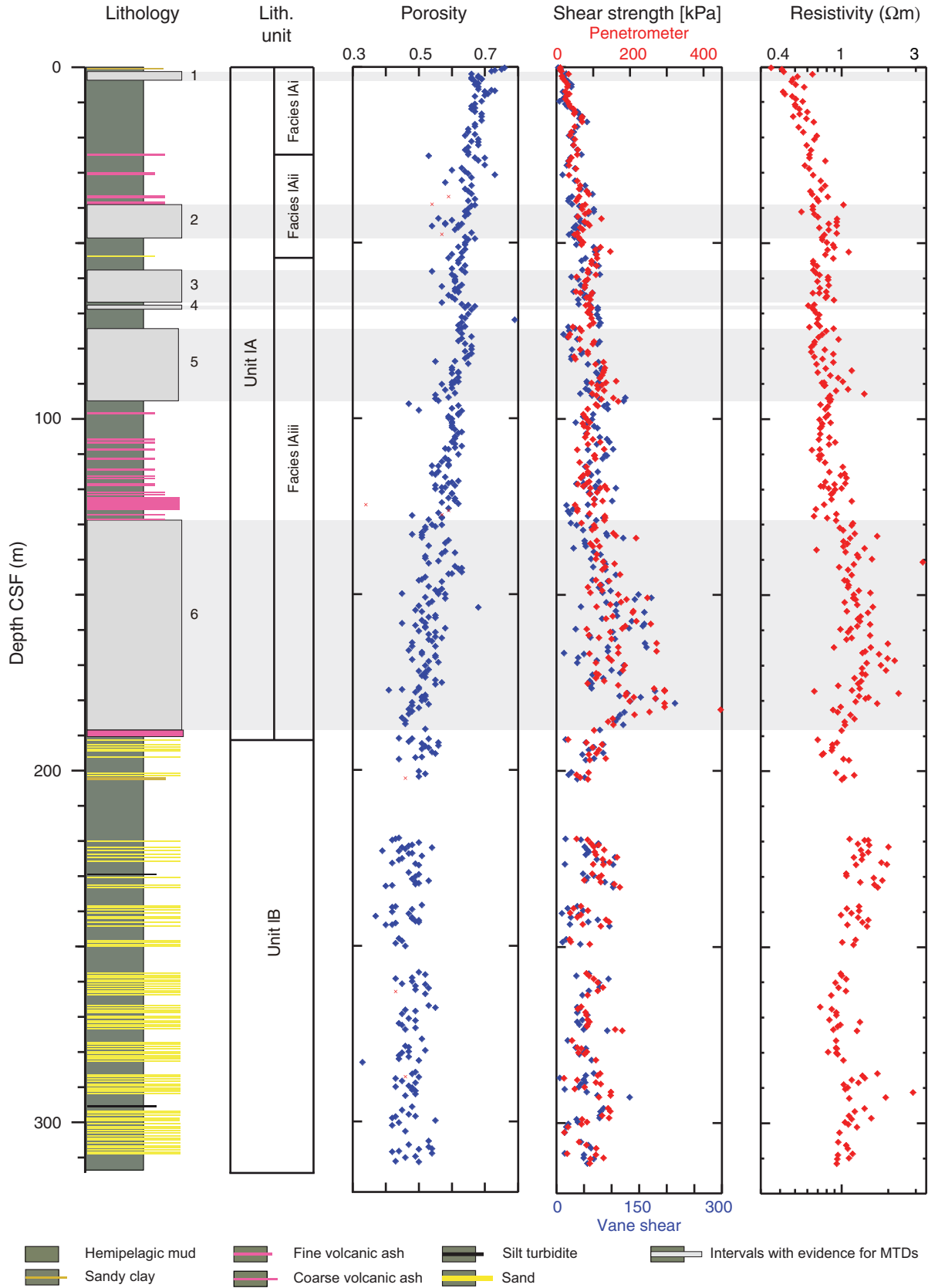


Figure F17. A. Volume of interstitial water recovered, Hole C0018A. B. Dissolved sulfate profile, used to estimate (C) percent contamination values.

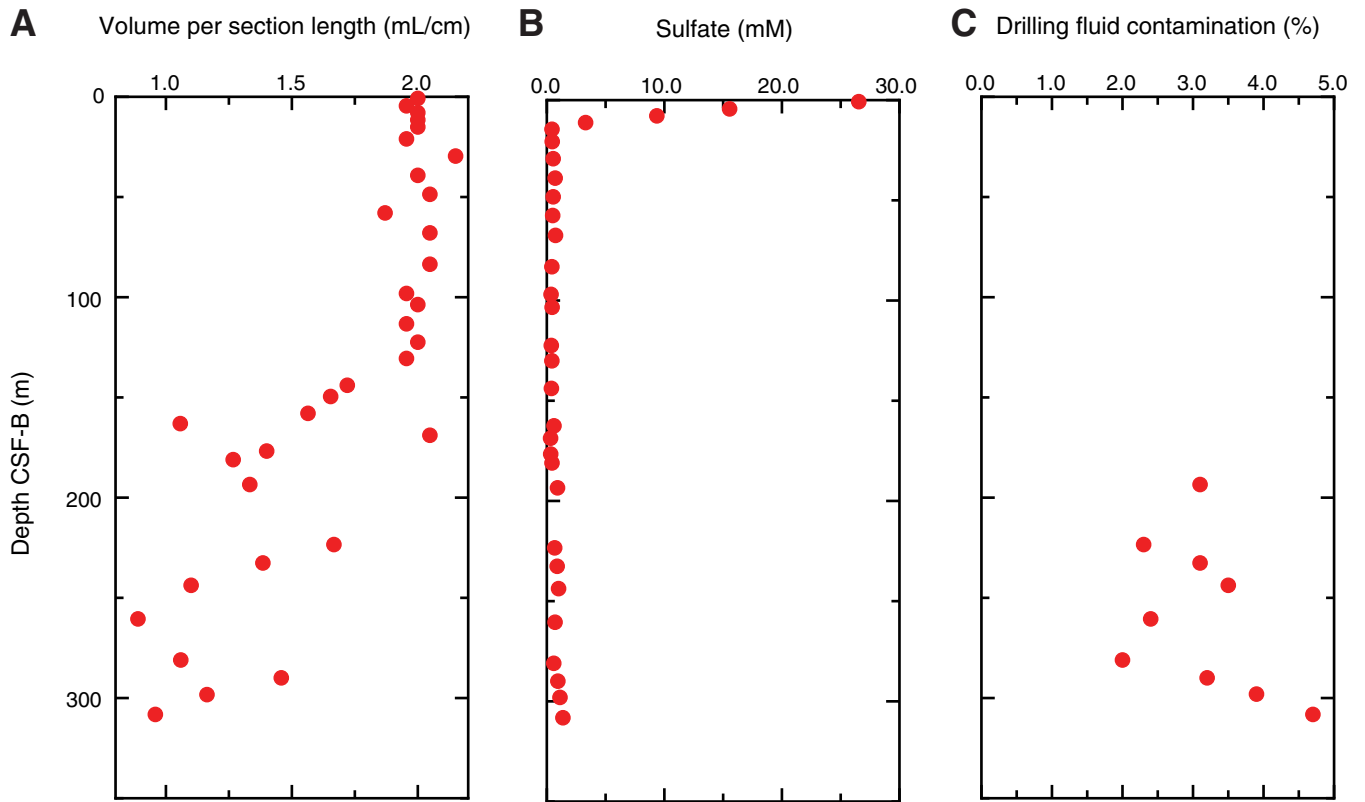


Figure F18. Pore water constituents (salinity, chlorinity, bromide, pH, alkalinity, sodium, ammonium, phosphate, Br/Cl, and boron), Hole C0018A.

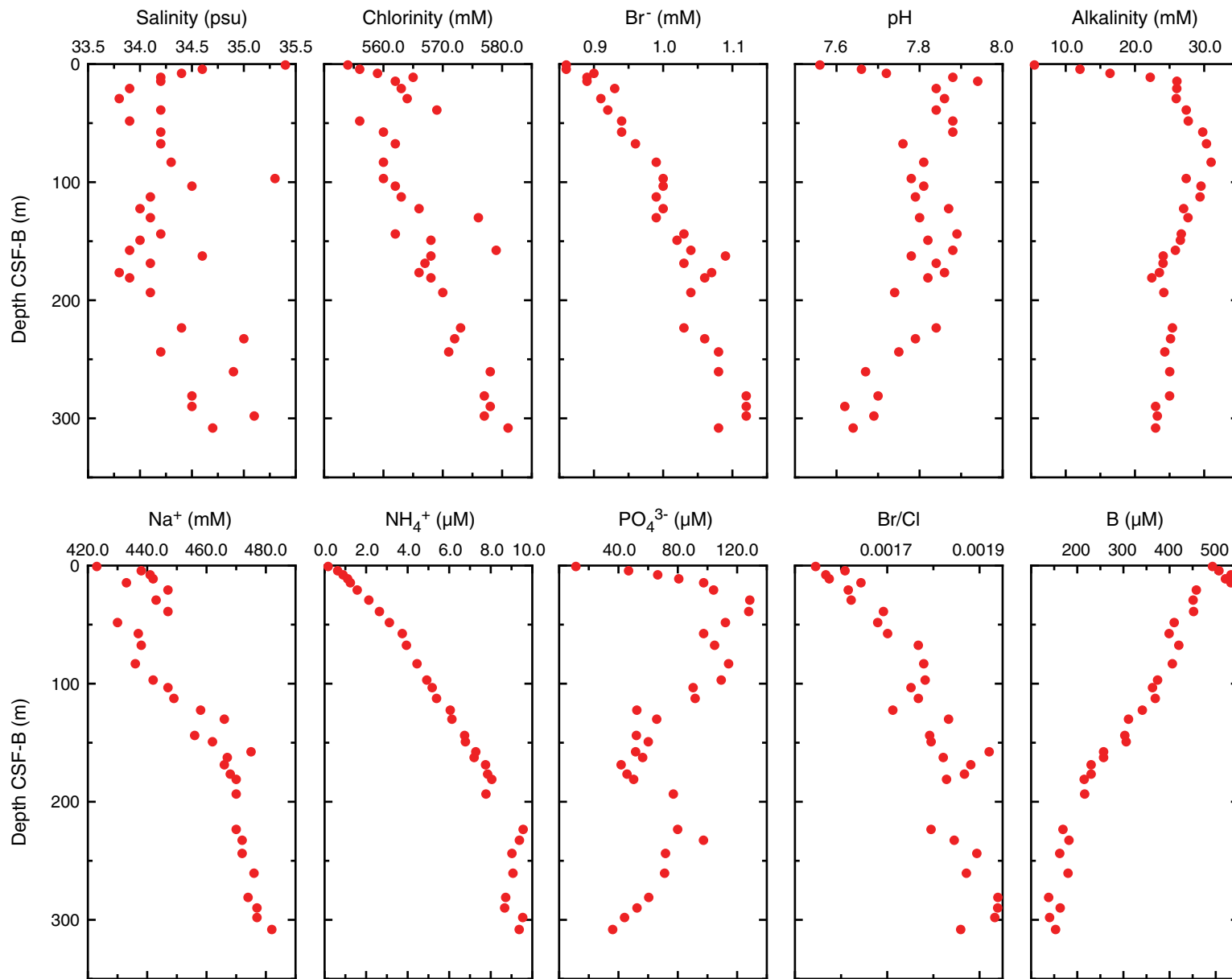


Figure F19. Pore water constituents (potassium, magnesium, calcium, silica, iron, lithium, strontium, barium, and manganese), Hole C0018A.

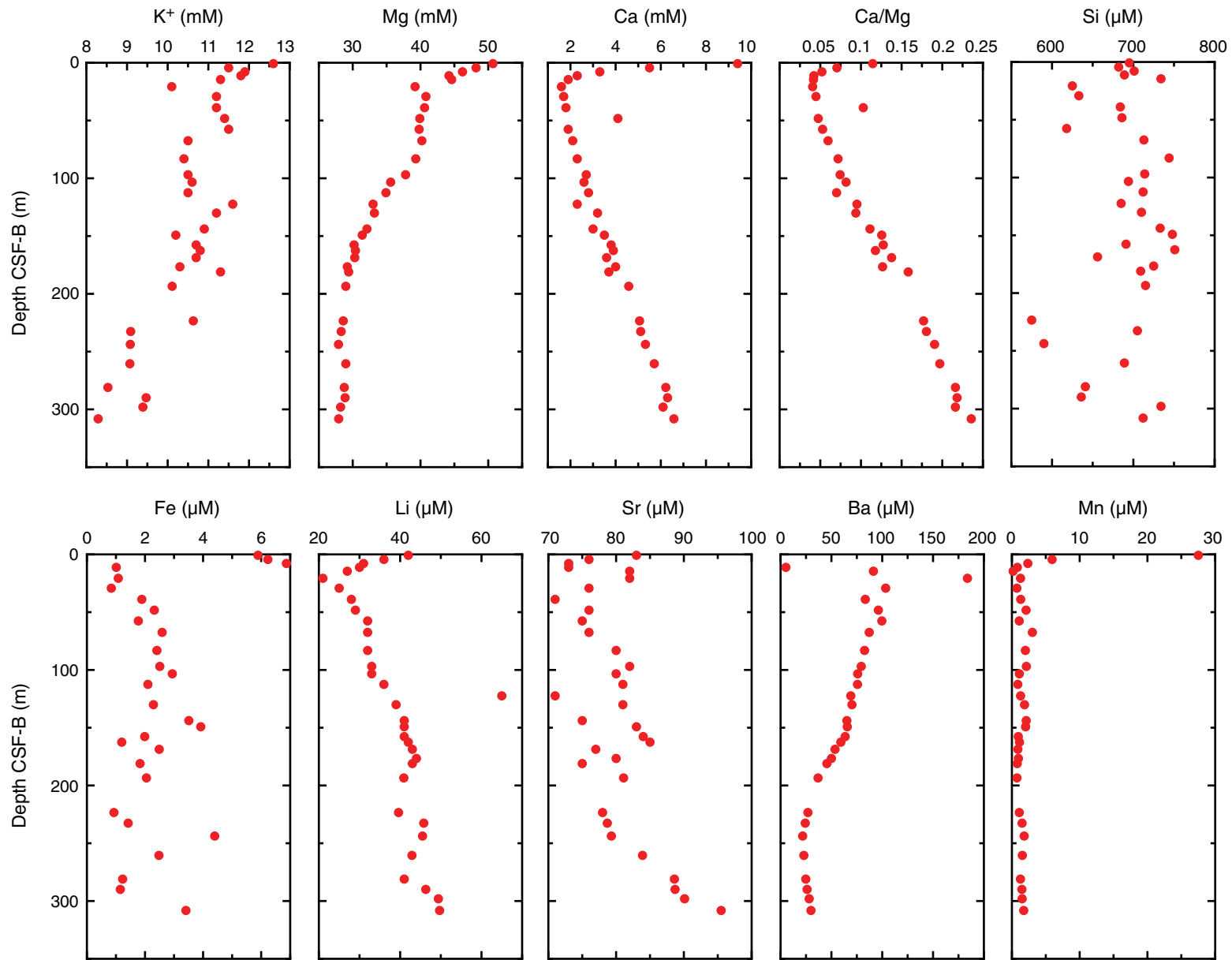


Figure F20. Methane, ethane, and C₁/C₂ ratios, Site C0018. C₁/C₂ is set at 100,000.0 when ethane concentration is below detection.

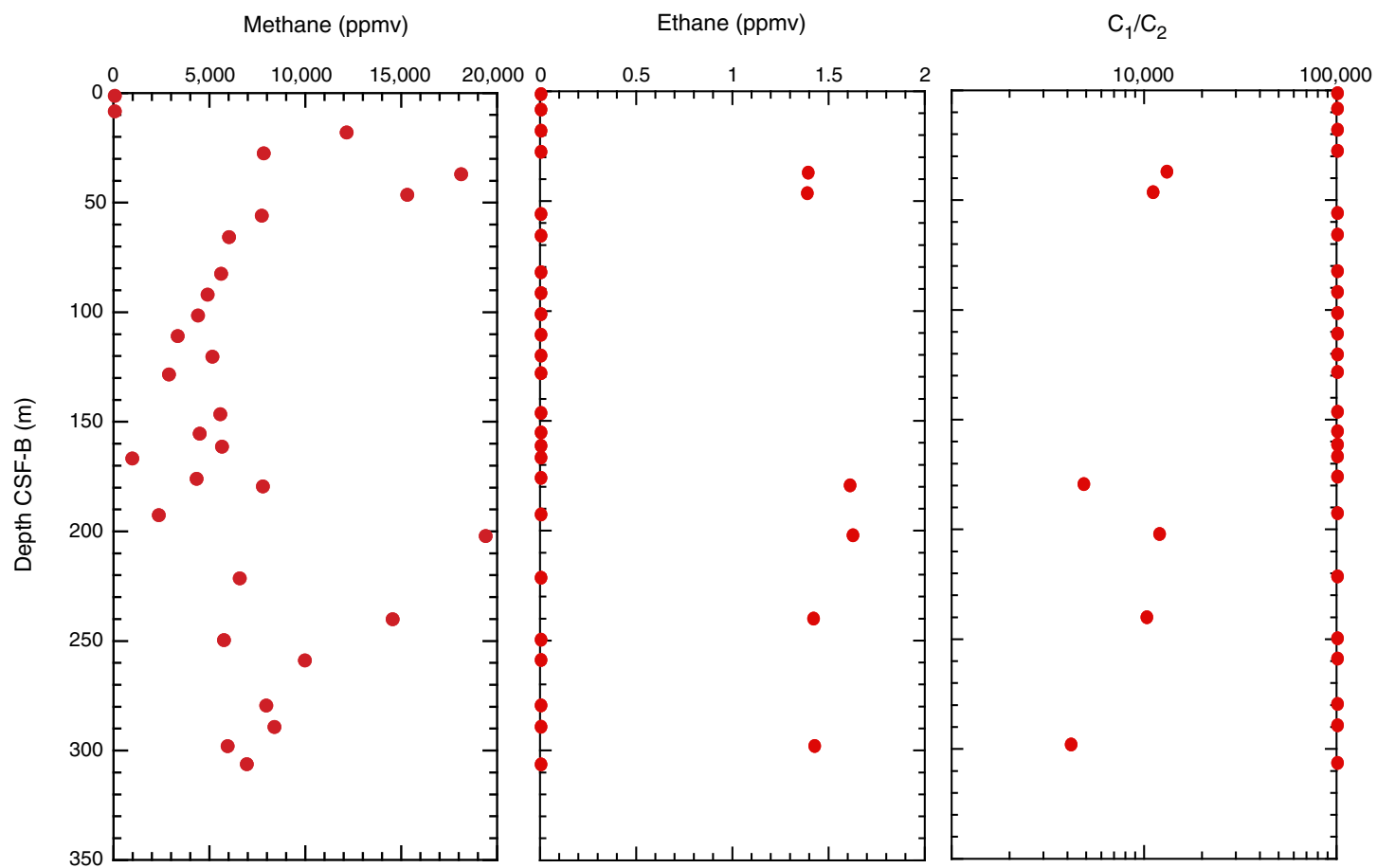


Figure F21. Calcium carbonate, total organic carbon (TOC), total nitrogen (TN), atomic ratios of TOC to TN (TOC/TN_{at}), and total sulfur (TS) contents in bulk sediment, Hole C0018A.

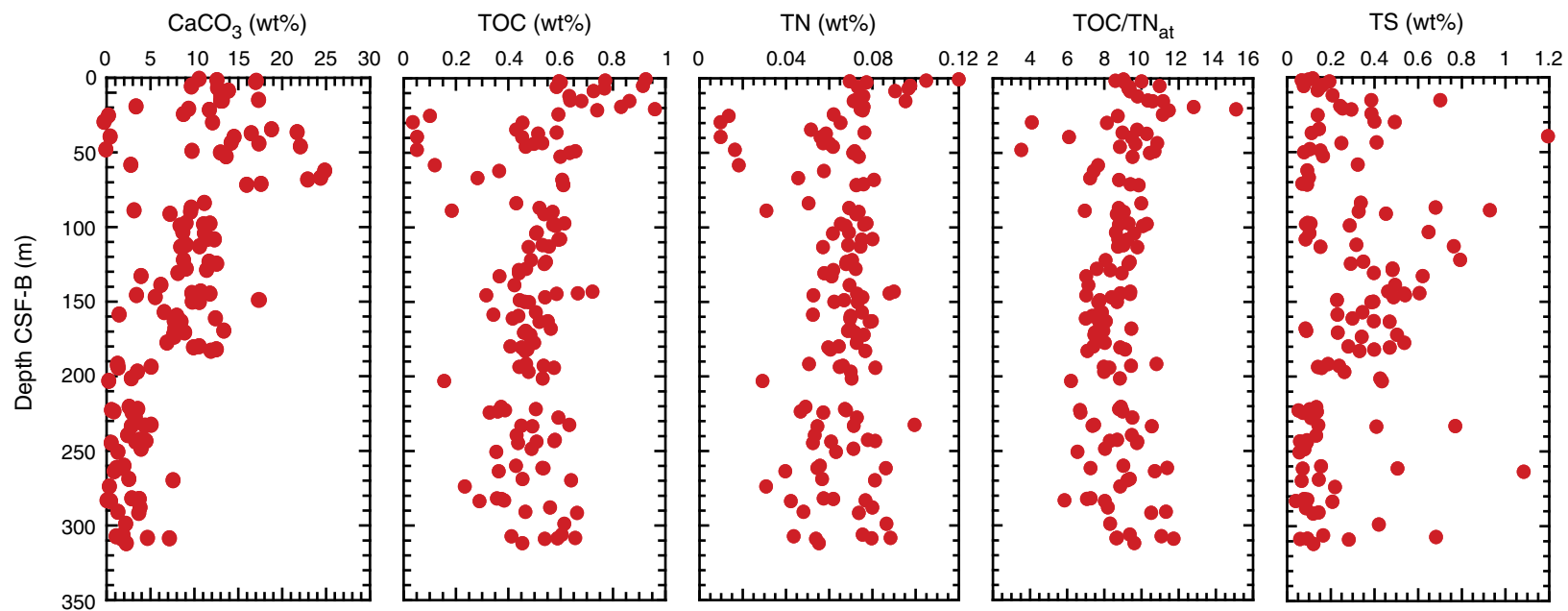


Figure F22. Lithology of Site C0018 on seismic profile. IL = in-line. VE = vertical exaggeration. B, G, N, and O = key seismic horizons. MTD = mass transport deposit. Figure modified after Strasser et al. (2011).

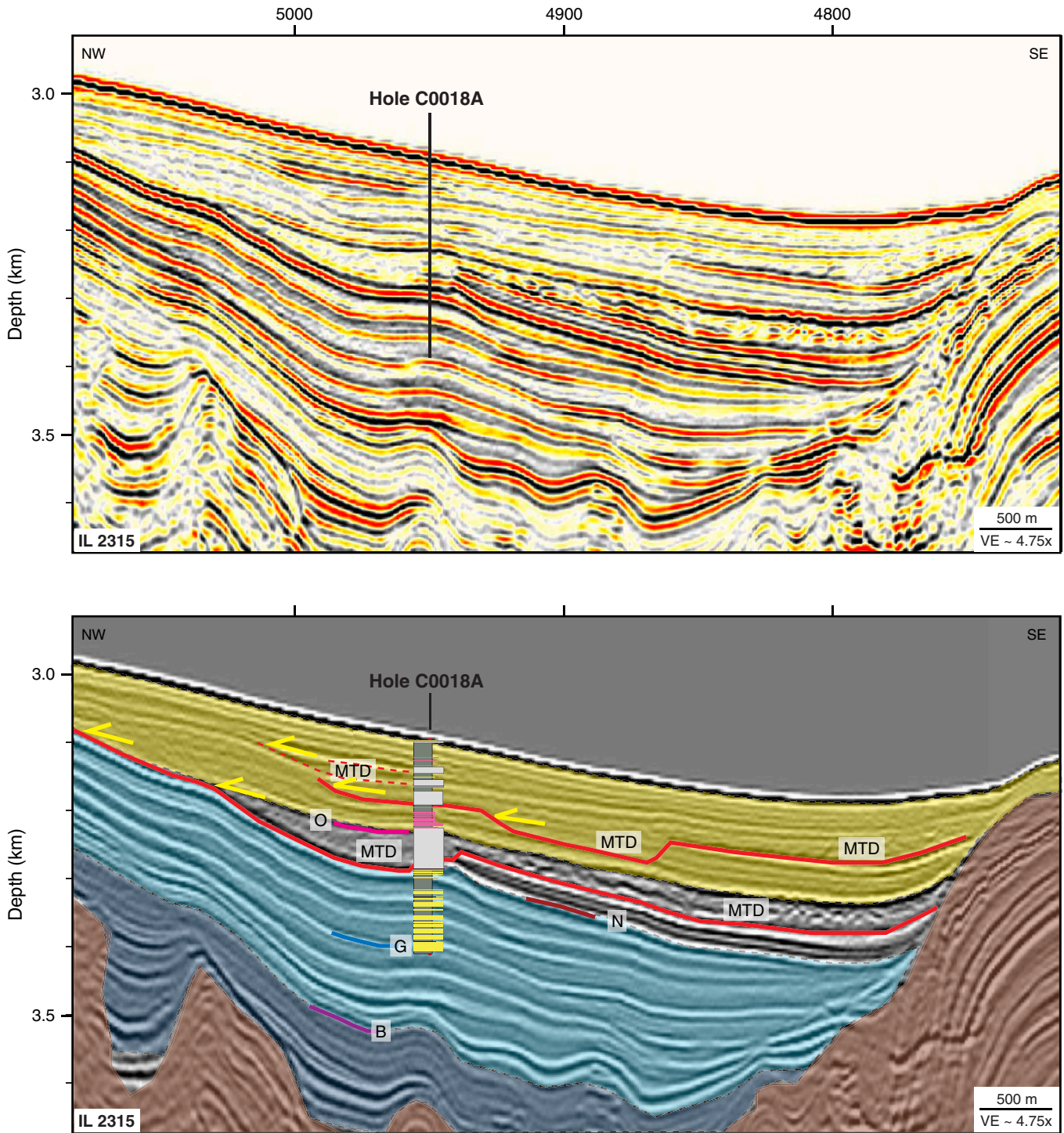


Figure F23. Summary of formation temperature measurements performed with APCT-3 at all three sites. Thermal gradient estimations from linear fit are indicated.

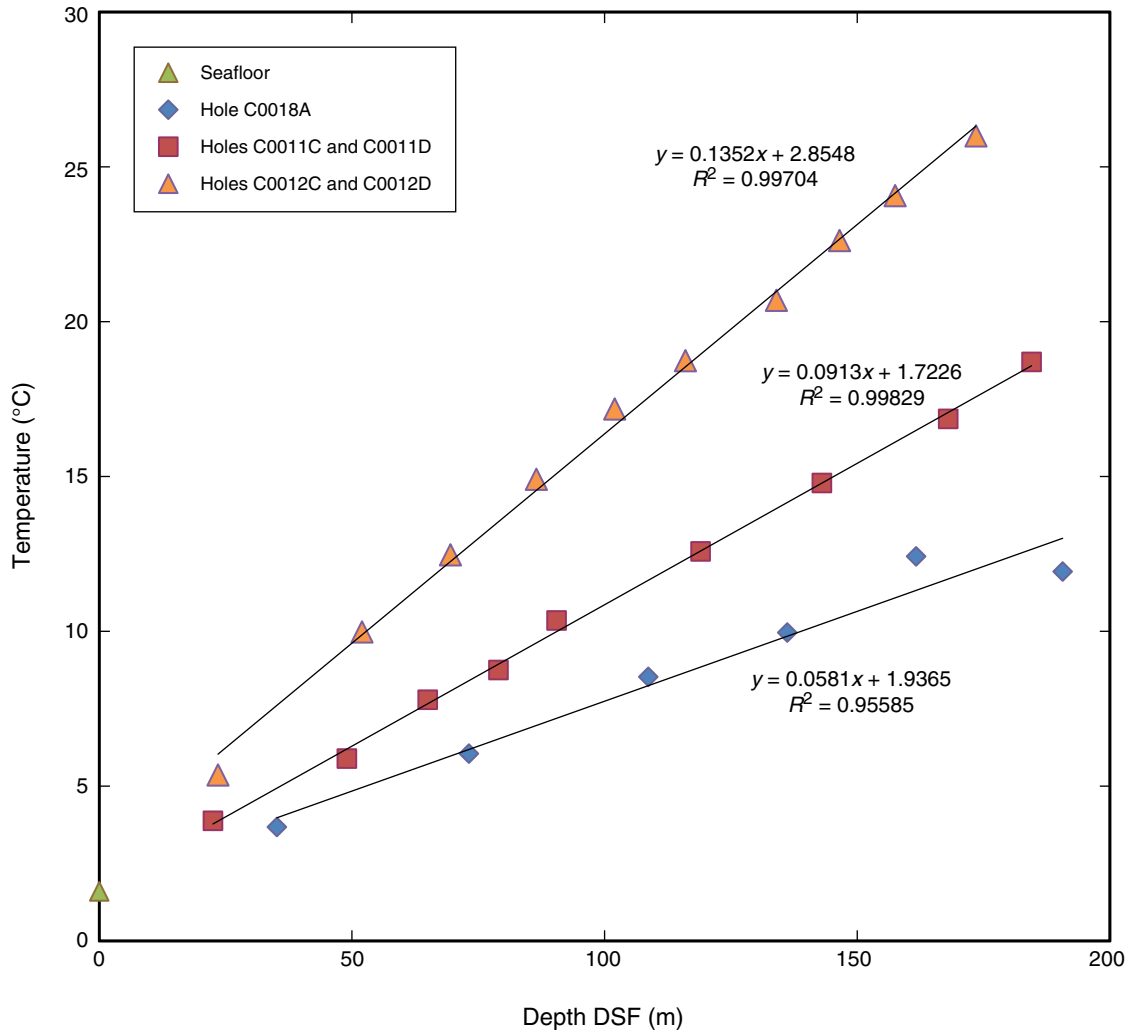


Figure F24. Detailed bathymetric map of Kashinosaki Knoll and Nankai Trough showing location of Sites C0011, C0012, and C0018.

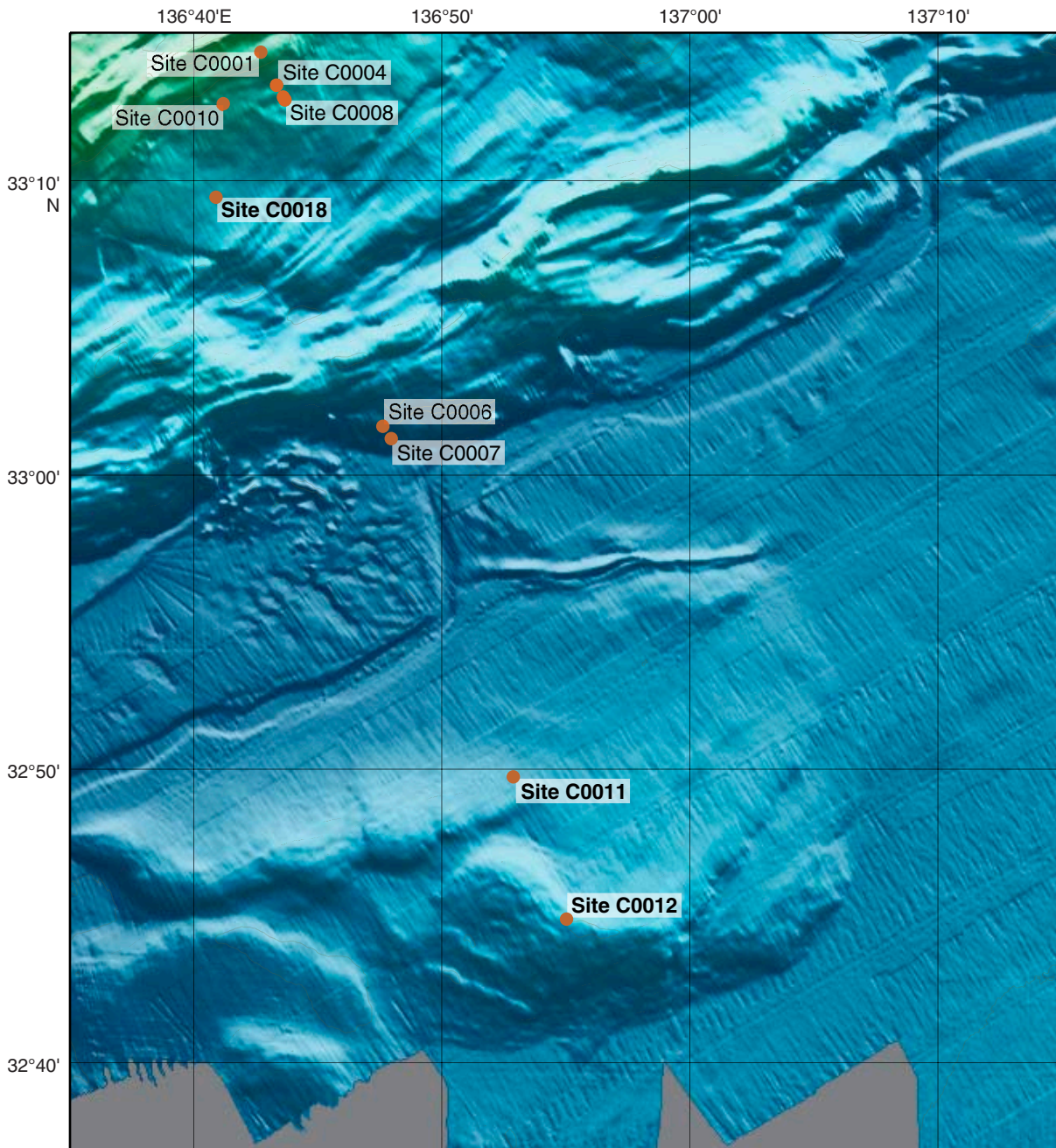


Figure F25. Lithologic columns on seismic background across Kashinosaki Knoll showing Sites C0011 and C0012, using results from Expeditions 333 and 322 (Underwood et al., 2010). VE = vertical exaggeration.

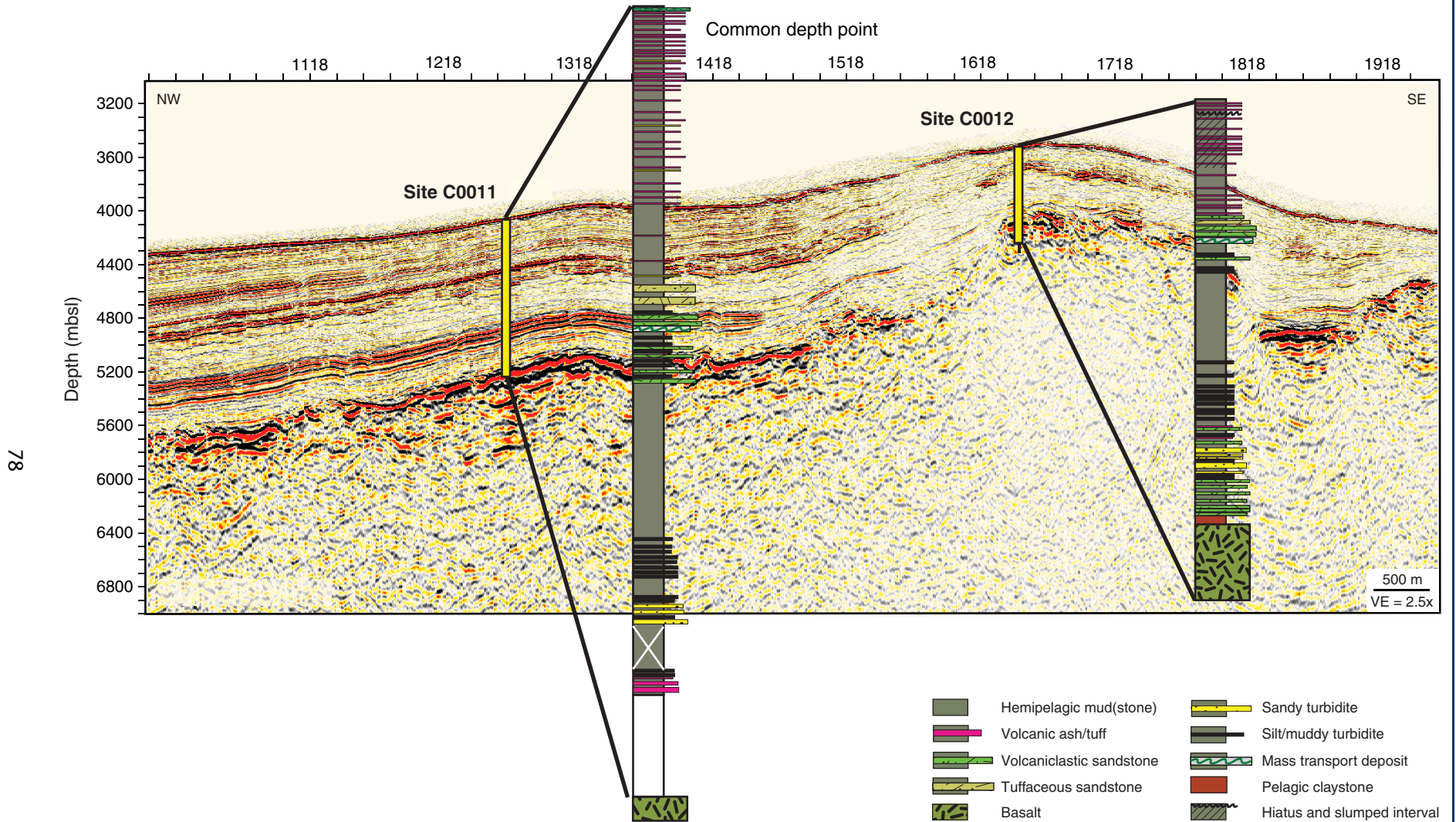


Figure F26. Sedimentary log, Holes C0011C and C0011D. MTD = mass transport deposit.

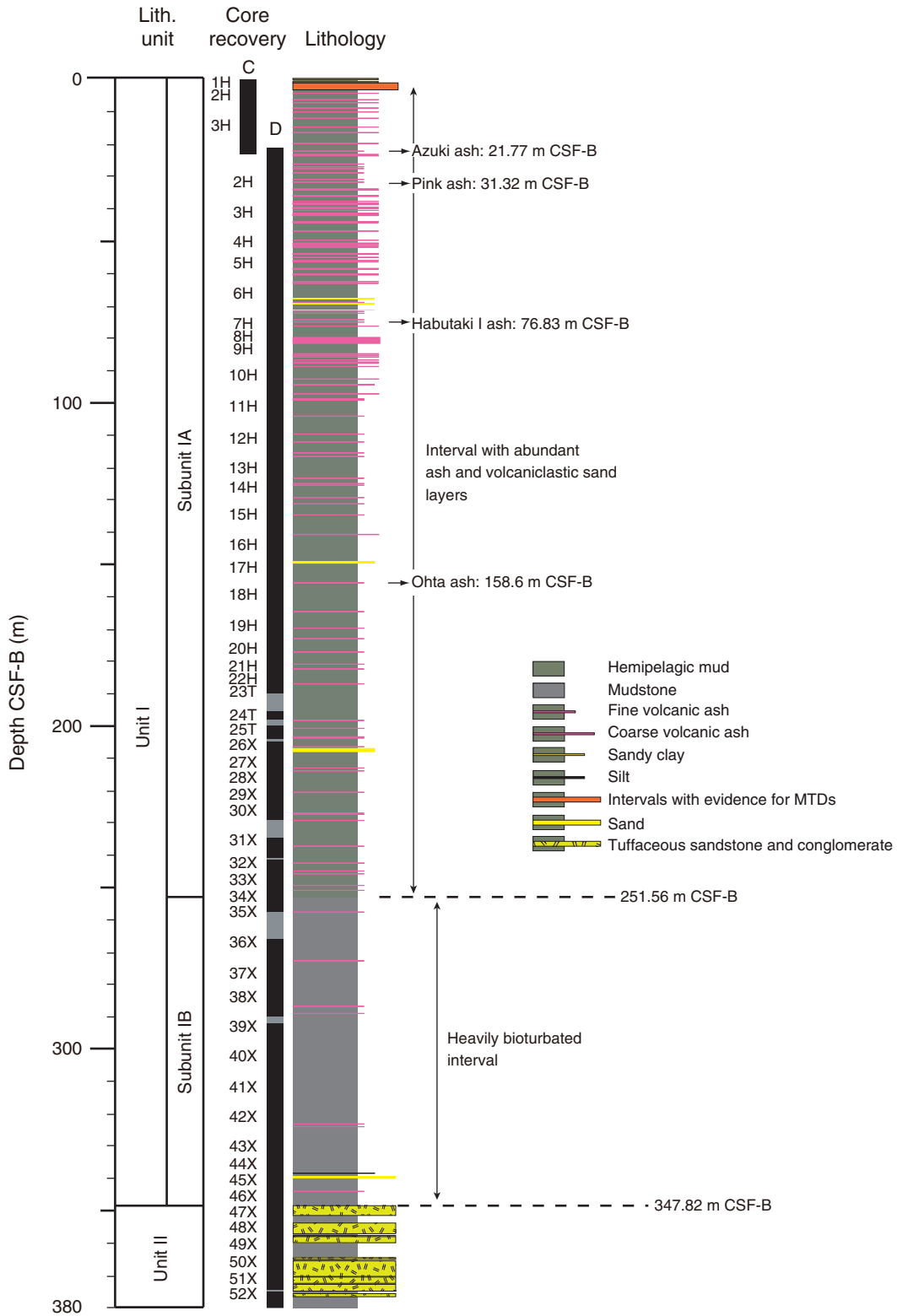


Figure F27. Summary of XRD data, Holes C0011C and C0011D. Unit and subunit boundaries are highlighted. Note that the Unit I/II boundary has no associated discontinuity in XRD data. MTD = mass transport deposit.

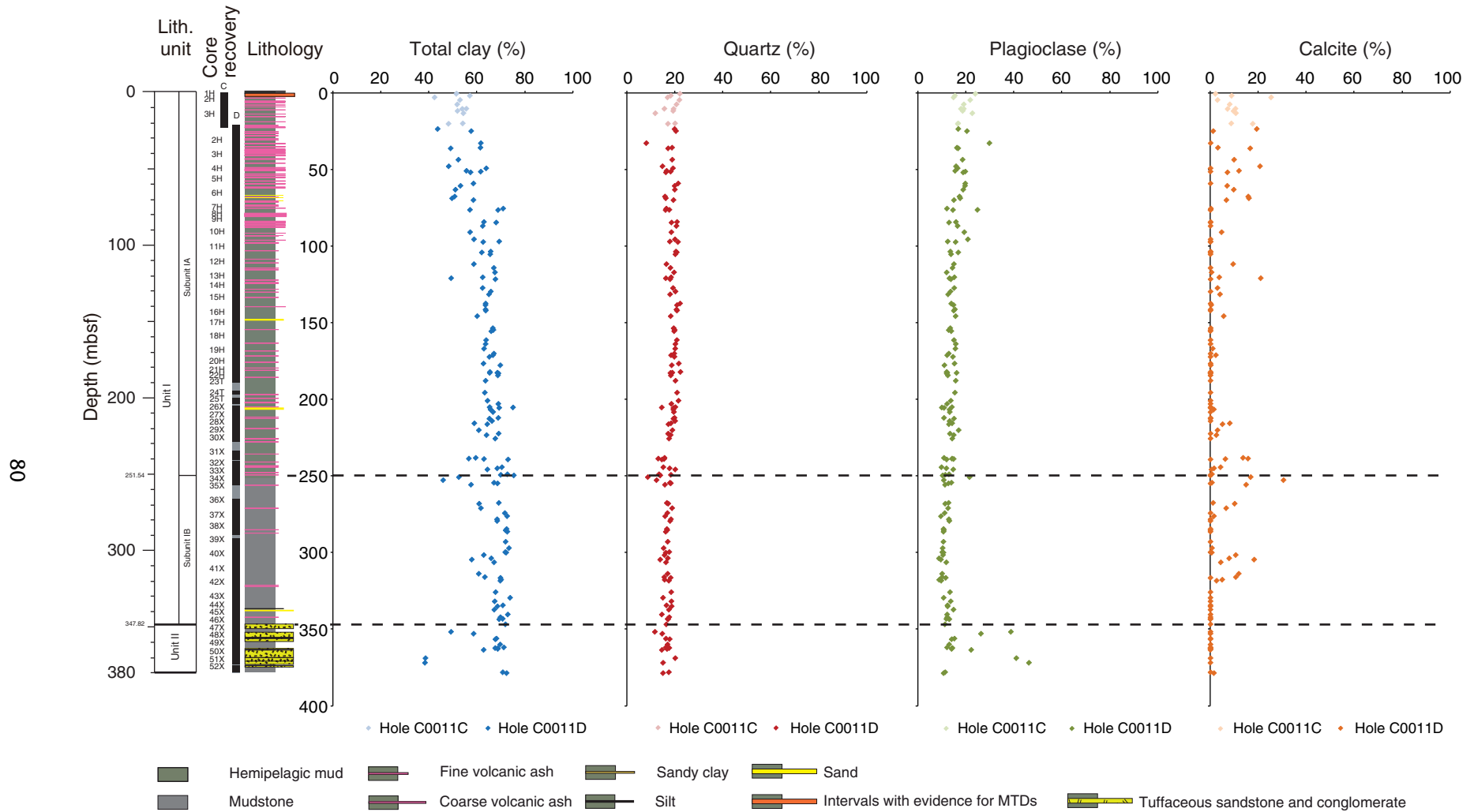


Figure F28. Variations of ash alteration state across Subunit IA/IB boundary and Unit I/II boundary. **A.** Unaltered glass shards in ash layers above 251.54 m CSF-B (Subunit IA). **B.** First appearance of altered glass in the succession. The appearance of such a degree of ash alteration characterizes strata within Subunit IB. **C.** Relatively larger degree of alteration to the ash shown in B. **D.** Reappearance of unaltered ash within Unit II.

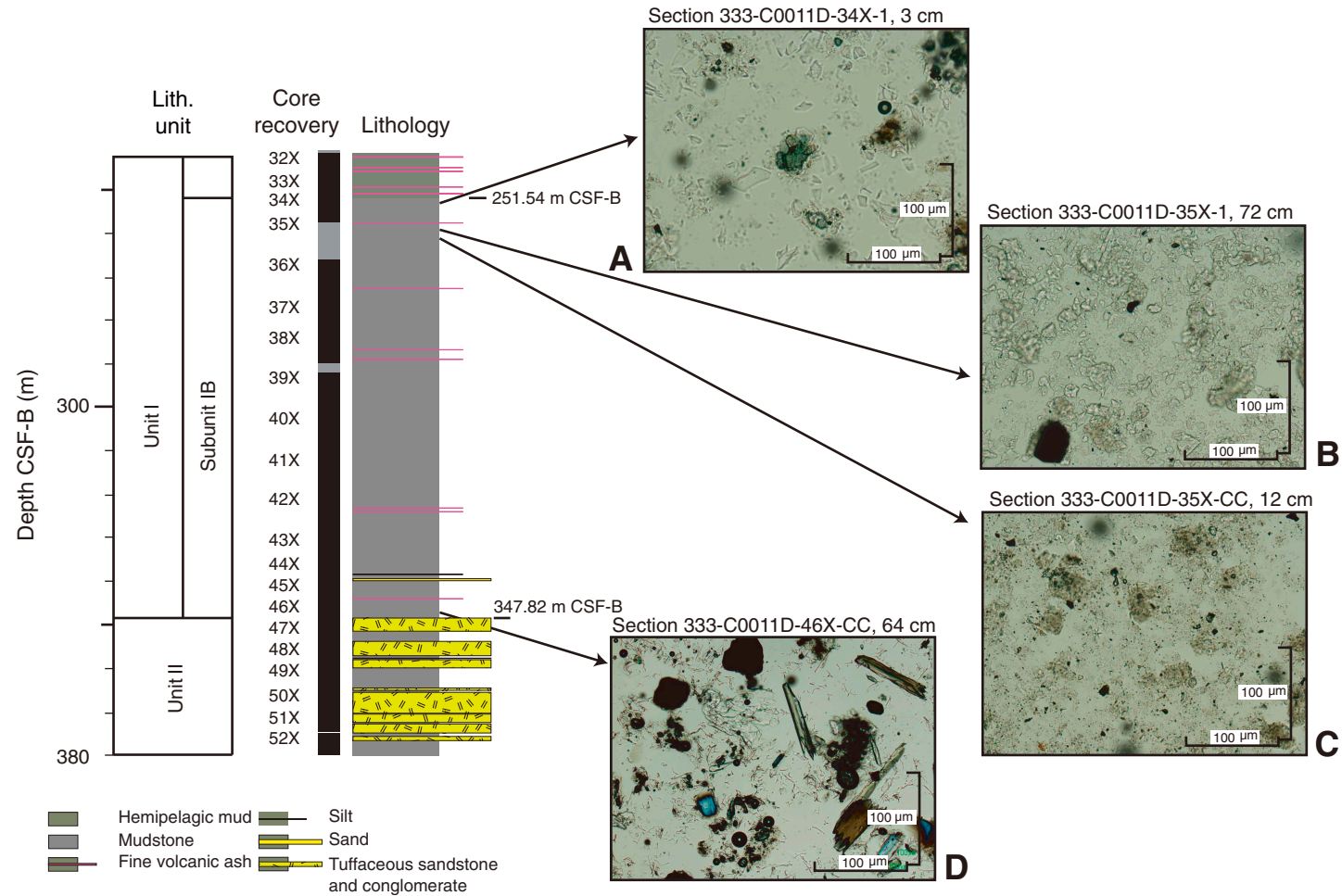


Figure F29. Core photos highlighting lithologic and textural differences between Unit I and Unit II, Hole C0011D. **A.** Section 333-C0011D-1H-1 ash layer interpreted as Azuki tephra (0.85 Ma; Hayashida et al., 1996). Greenish brown hemipelagites present cyclic green layers, which have increased iron content according to XRF logging data. Clay is mottled and often bioturbated, particularly in Subunit IB. **B.** Section 333-C0011D-50X-3 showing tuffaceous sandstone facies with heterolithic gravels. **C.** Detail of section 333-C0011D-51X-2 showing coarse tuffaceous sandstone with pumice (P), mudstone (M), and ash pebbles.

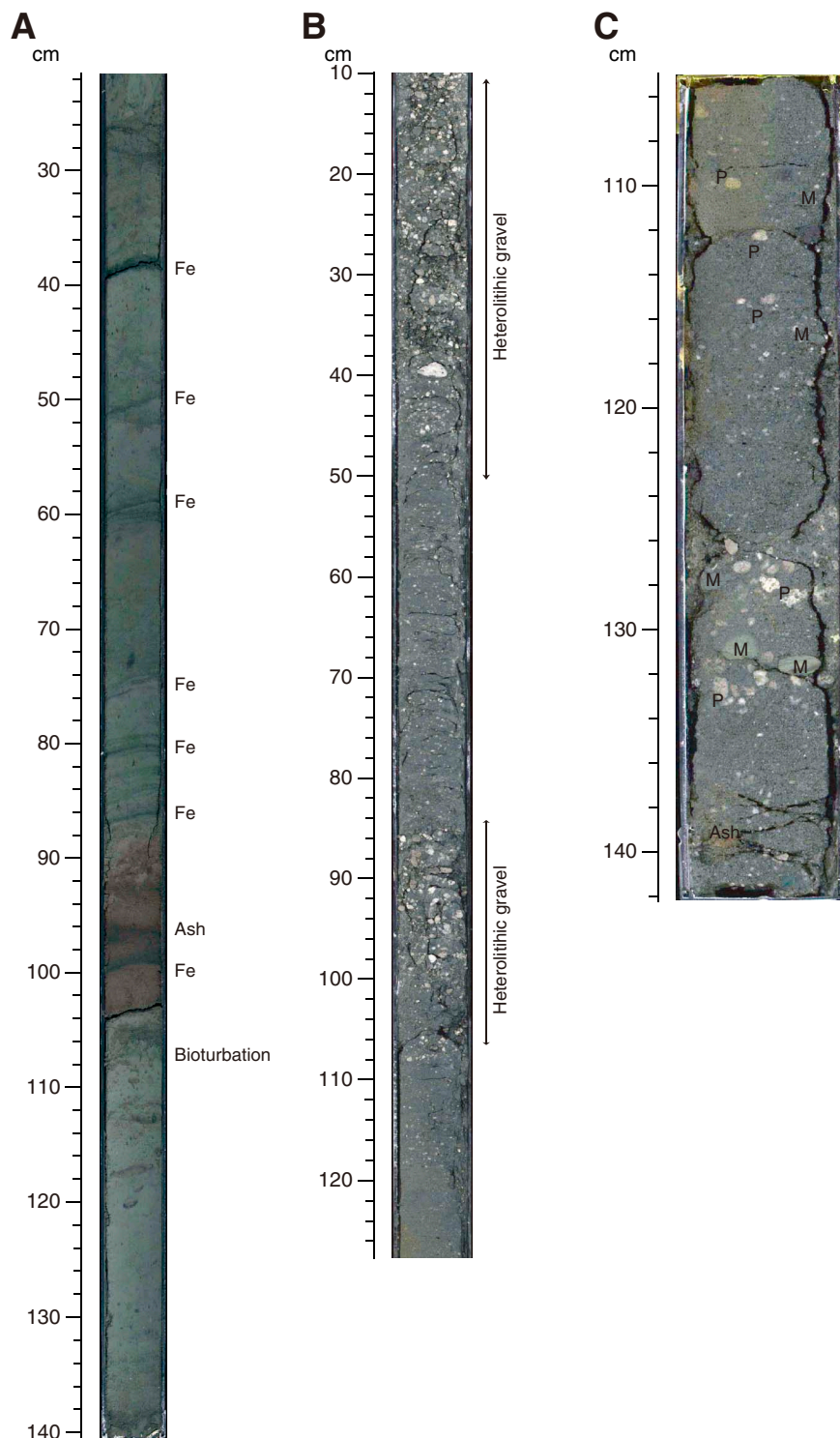


Figure F30. Variations of SiO₂, Al₂O₃, CaO, Fe₂O₃, Na₂O, K₂O, and P₂O₅ contents as a function of depth at Site C0011 from X-ray fluorescence (XRF) analysis. For lithology key, see Figure F26.

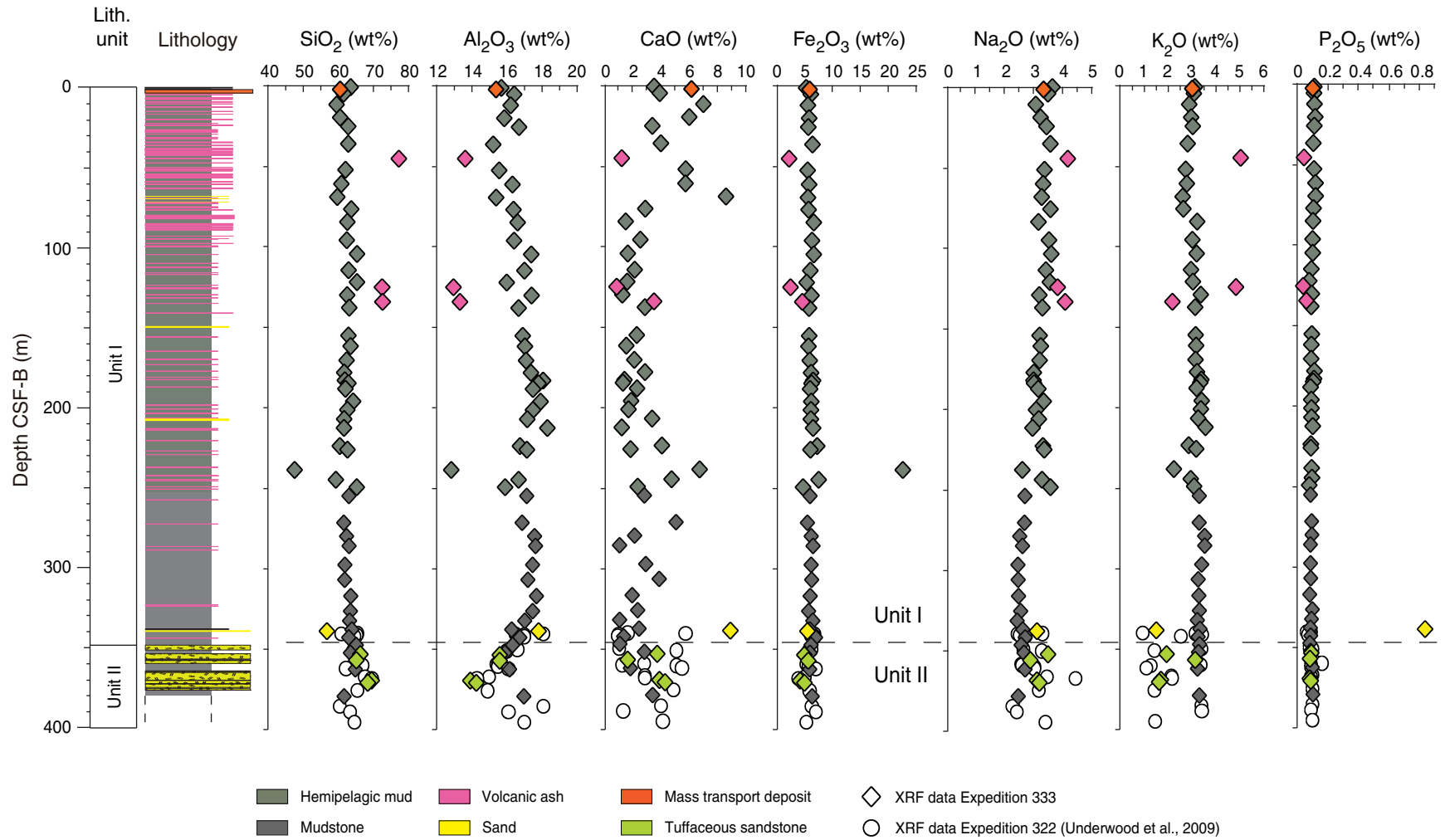


Figure F31. Distribution of bedding dip angles and deformation structures with depth, Holes C0011C and C0011D.

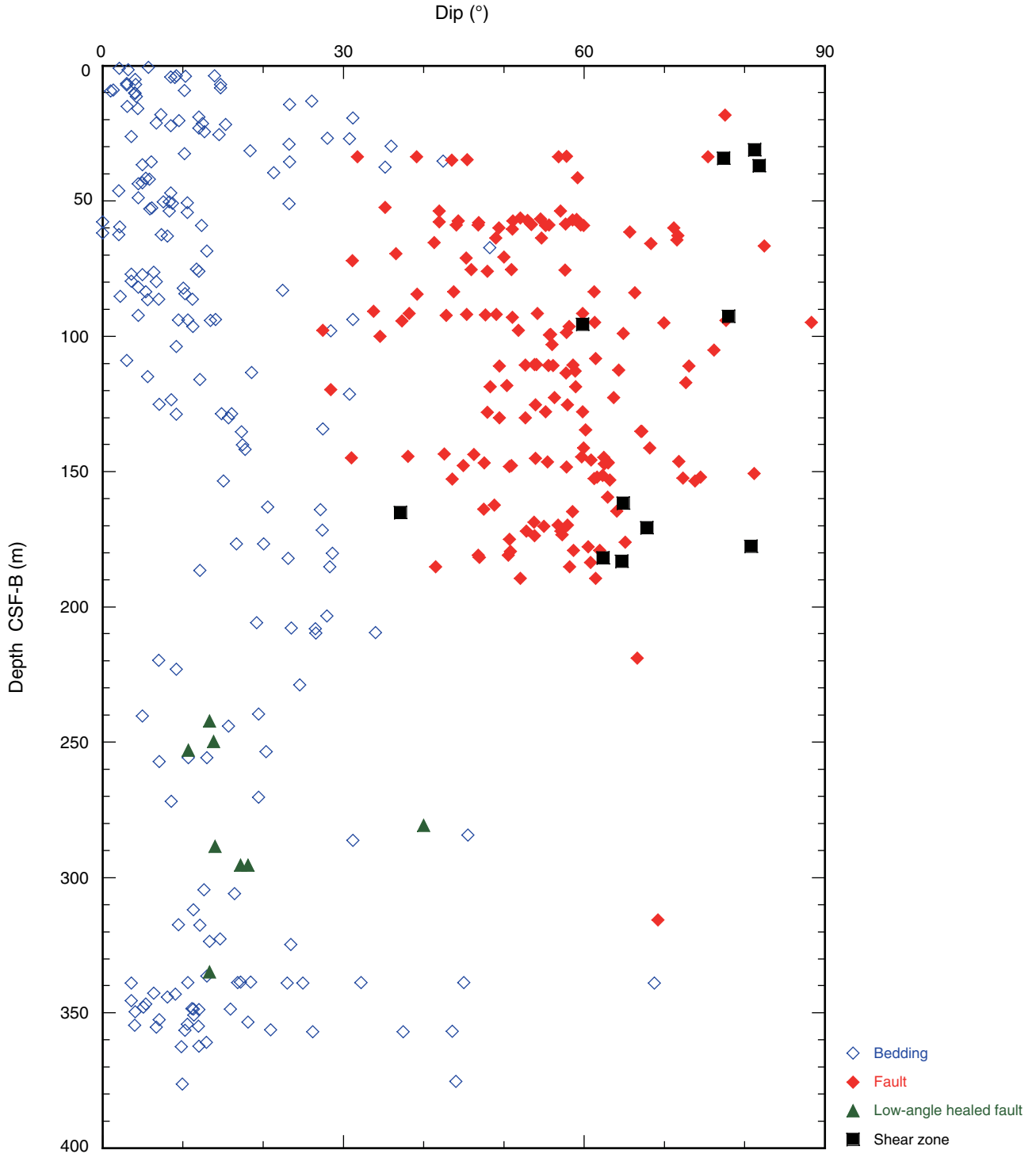
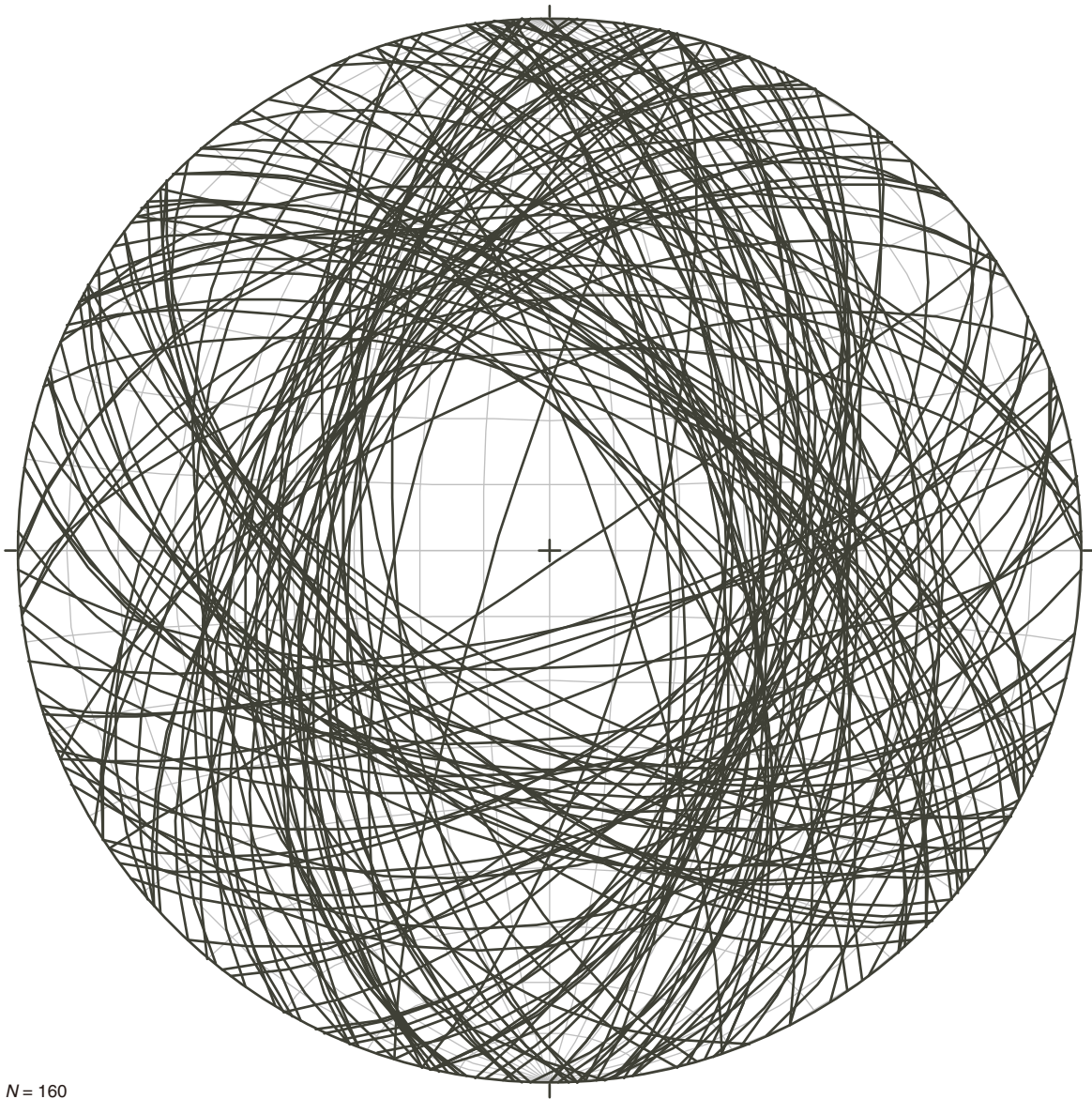


Figure F32. Lower-hemisphere equal-area projections of fault data, Holes C0011C and C0011D.



$N = 160$

Figure F33. Magnetic susceptibility and remanent magnetization before and after 30 mT AF demagnetization and stratigraphic interpretation of magnetic reversals, Site C0011. Green = NRM after 30 mT AF demagnetization, blue = remanent magnetization after 30 mT AF demagnetization, red = remanent magnetization after 400°C thermal demagnetization.

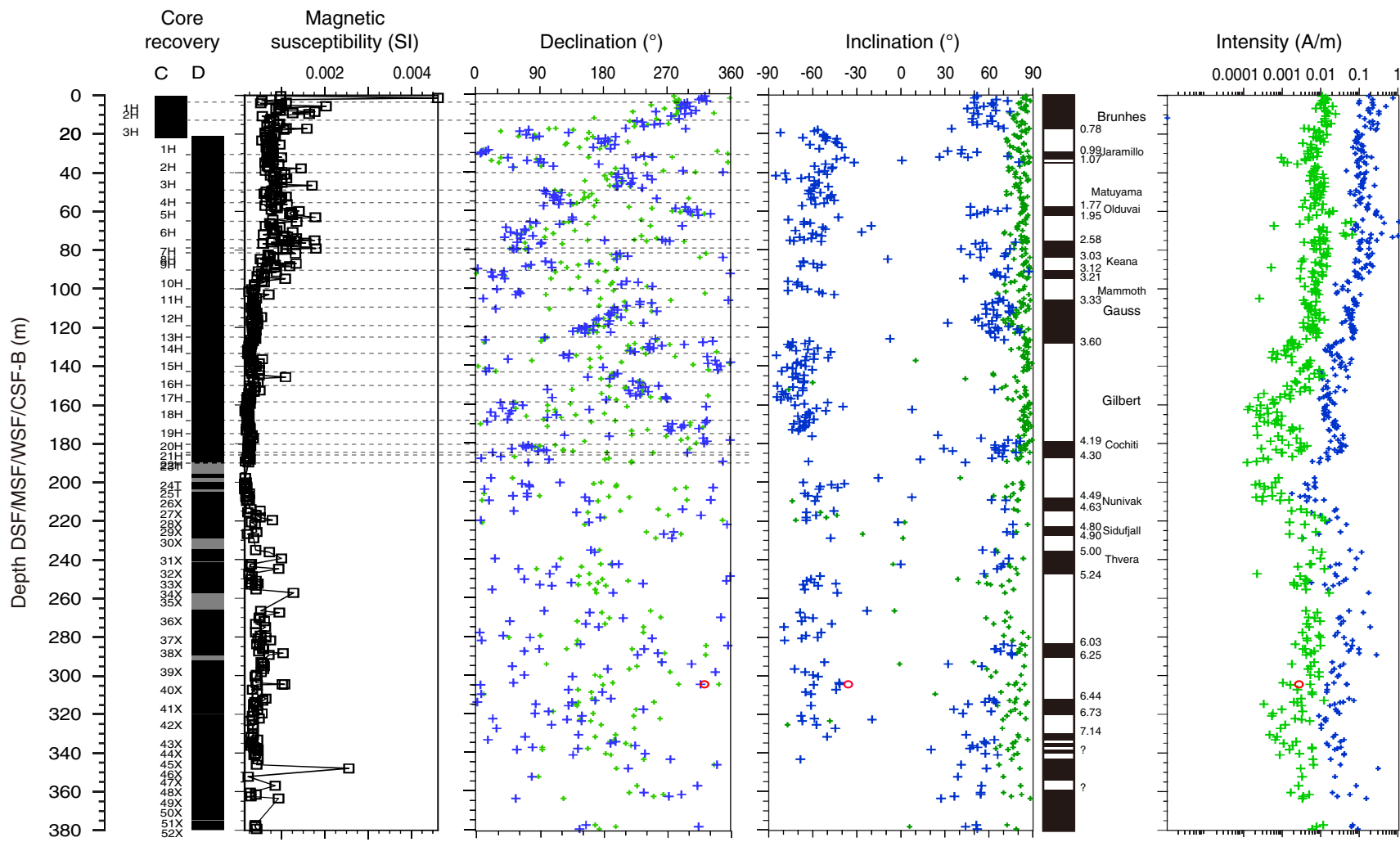


Figure F34. Resistivity measurements made on split sections from Site C0011 plotted with whole-round multisensor core logger (MSCL-W) resistivity and porosity from MAD measurements.

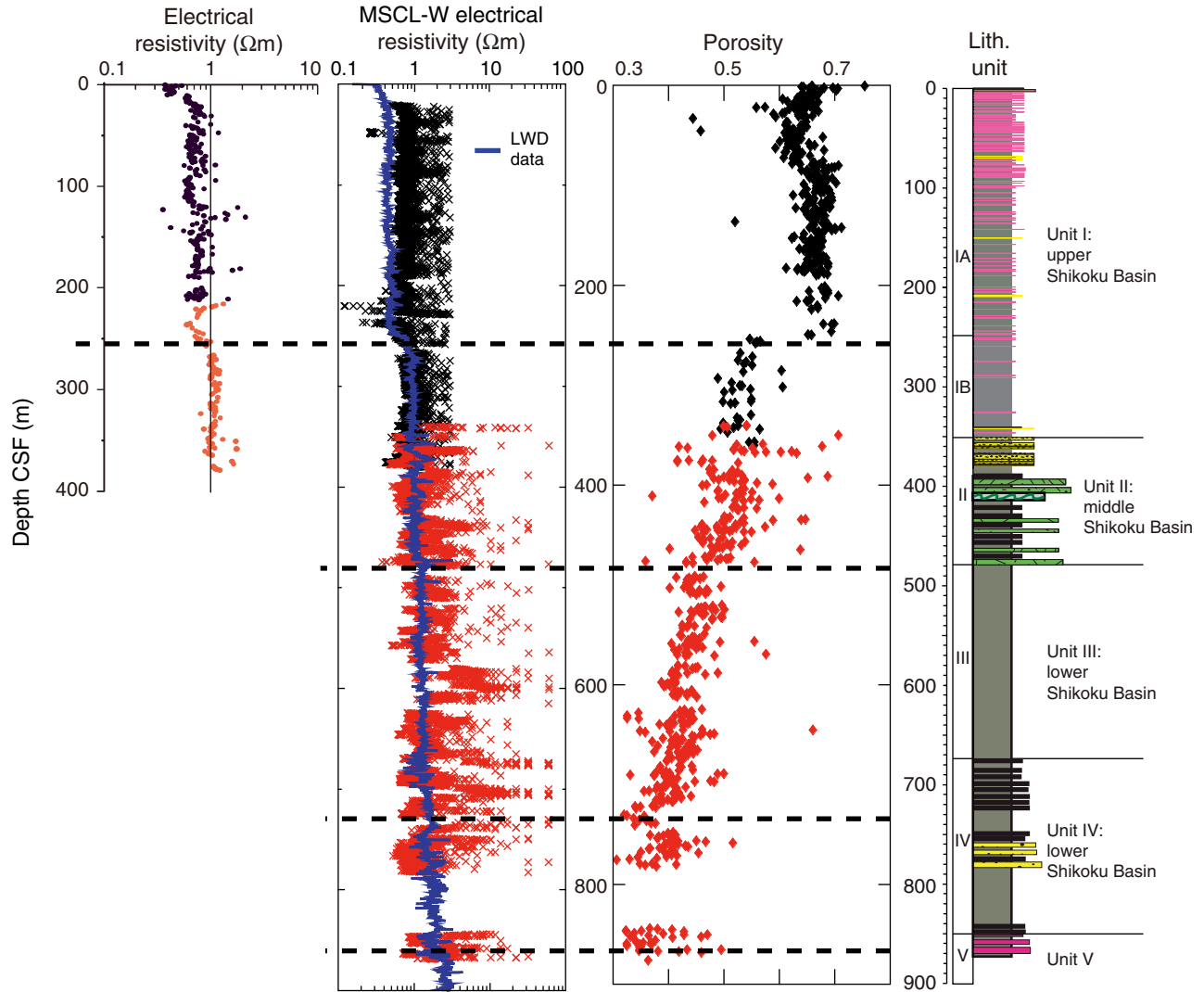


Figure F35. Penetrometer and vane shear measurements from Site C0011 plotted with porosity from MAD measurements.

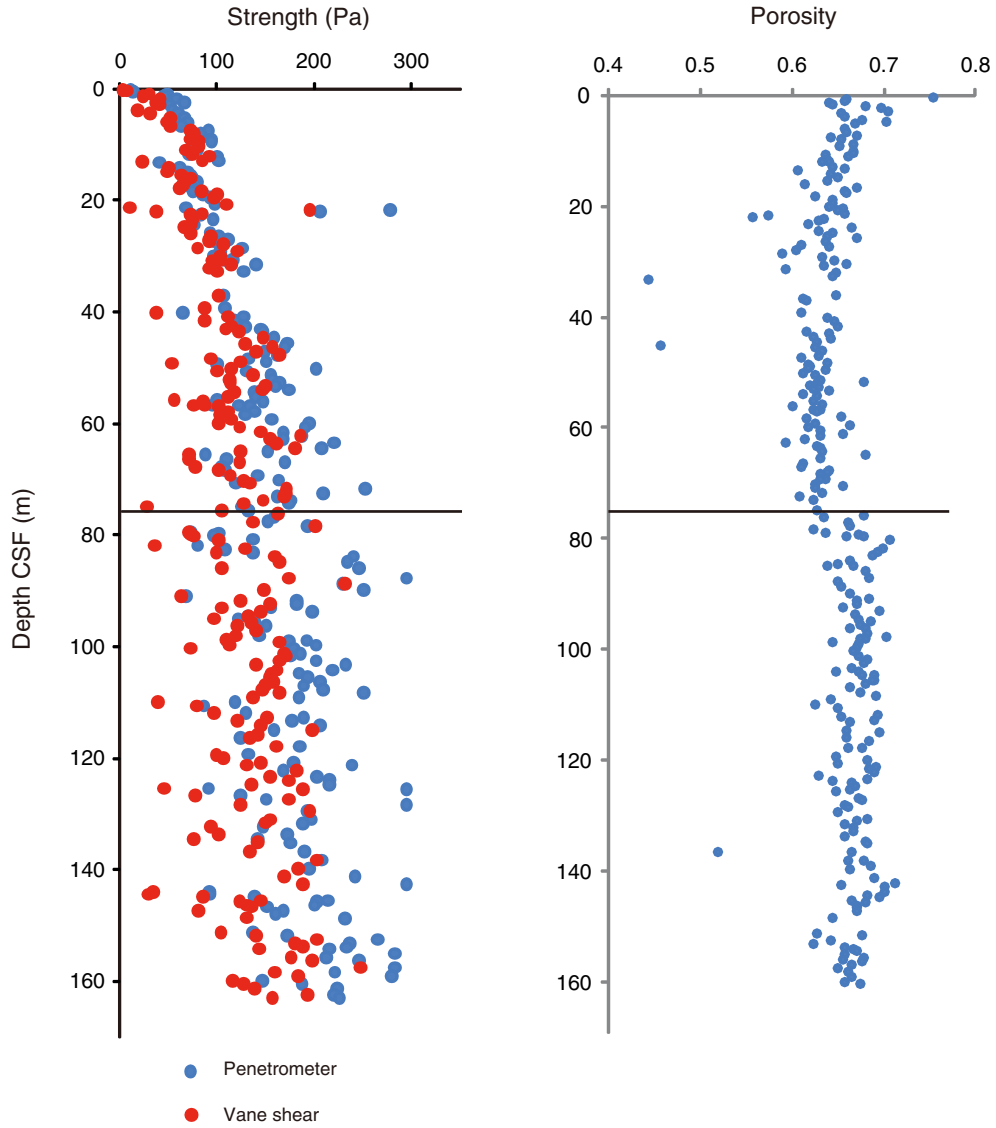


Figure F36. A. *P*-wave velocity measured in Holes C0011D (Expedition 333) and C0011B (Expedition 322). B. Vertical plane anisotropy from Holes C0011D and C0011B.

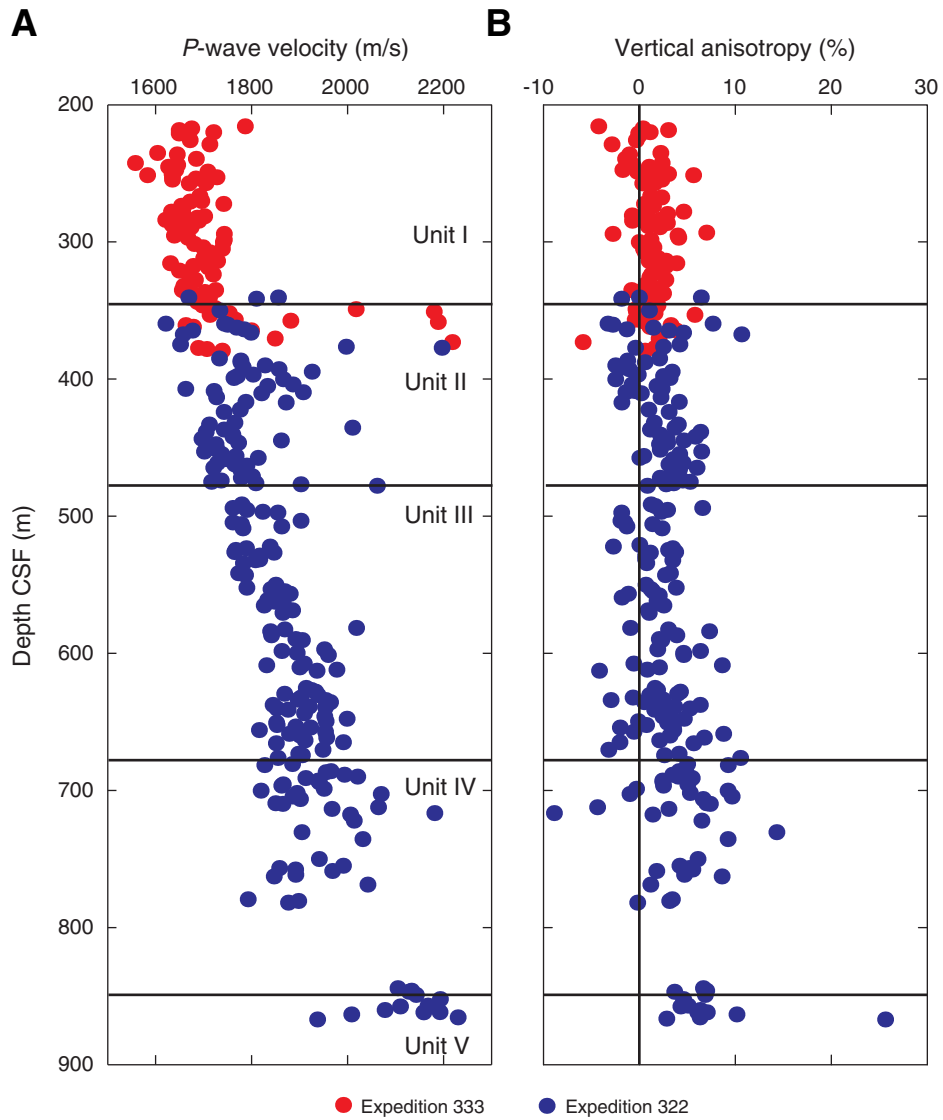


Figure F37. **A.** Volume of interstitial water recovered from Holes C0011C and C0011D per length of interstitial water section (mL/cm). **B.** Dissolved sulfate profile, used to estimate the **(C)** percent contamination values in cores taken via EPCS and ESCS from Holes C0011C and C0011D (red) and Expedition 322 Hole C0011B (blue).

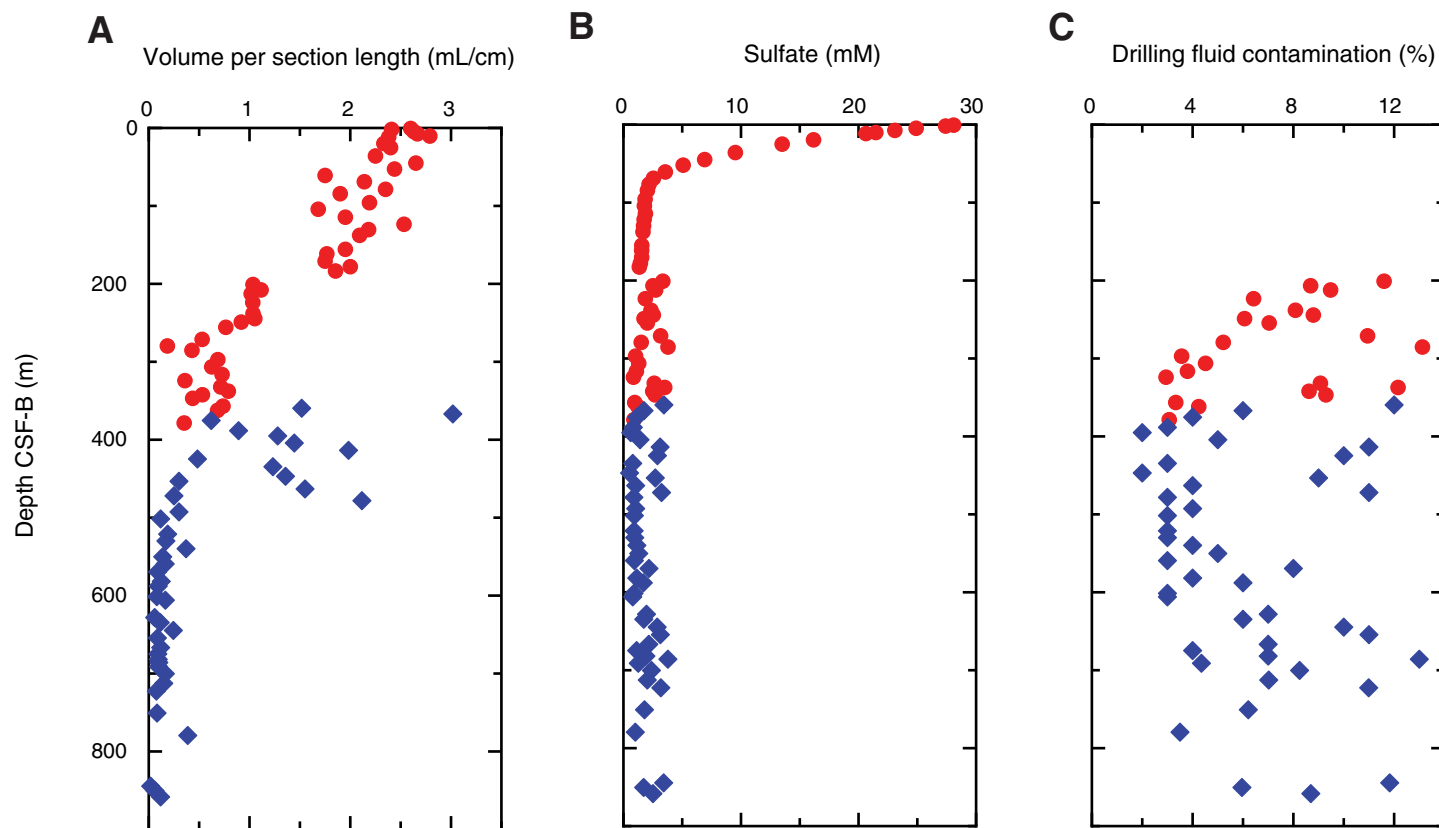


Figure F38. Interstitial water constituents (salinity, chlorinity, bromide, pH, alkalinity, sodium, ammonium, phosphate, Br/Cl, and boron) from Holes C0011C and C0011D (red) and Expedition 322 Hole C0011B (blue).

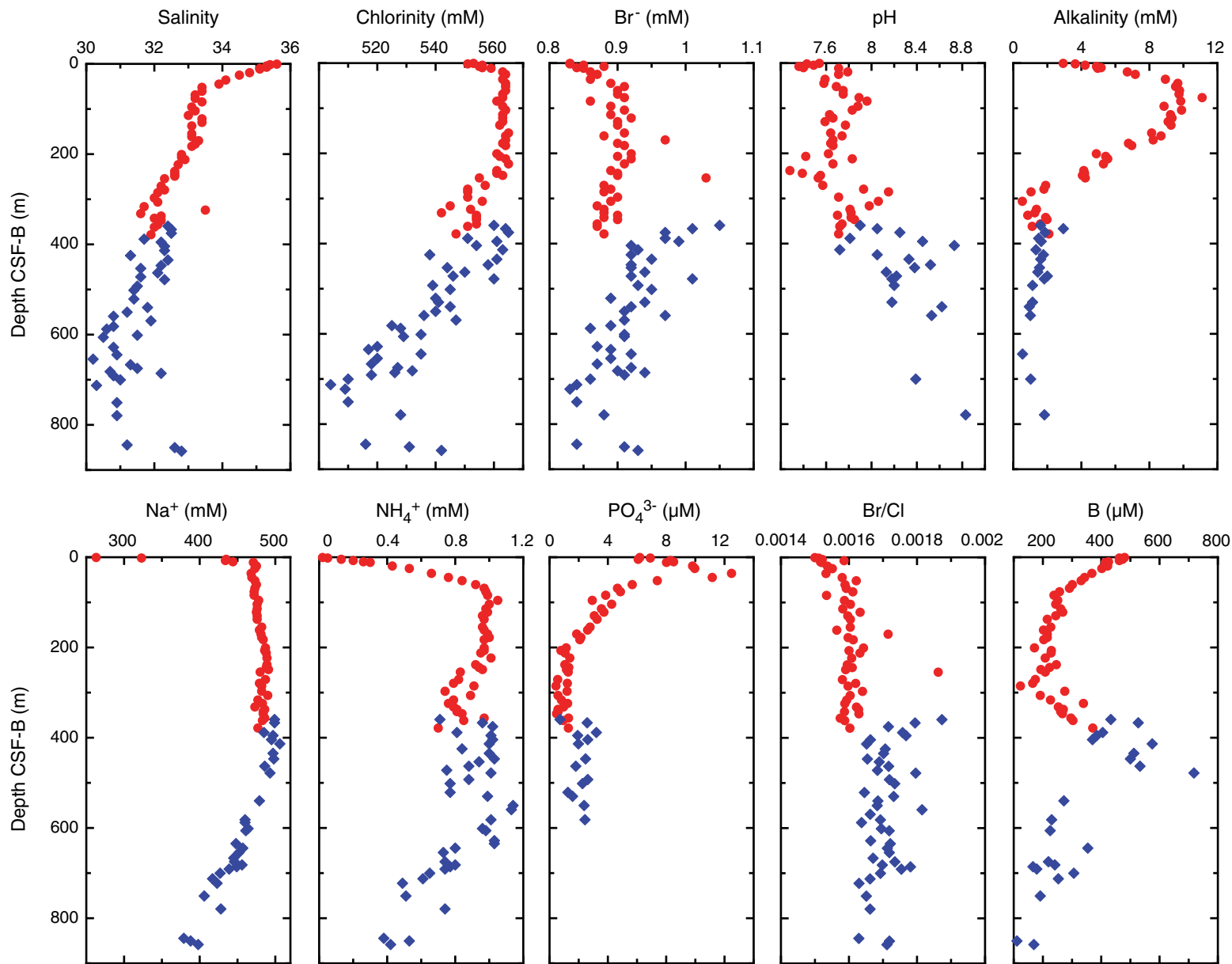


Figure F39. Interstitial water constituents (potassium, magnesium, calcium, Ca/Mg, silica, iron, lithium, strontium, barium, and manganese) from Holes C0011C and C0011D (red) and Expedition 322 Hole C0011B (blue).

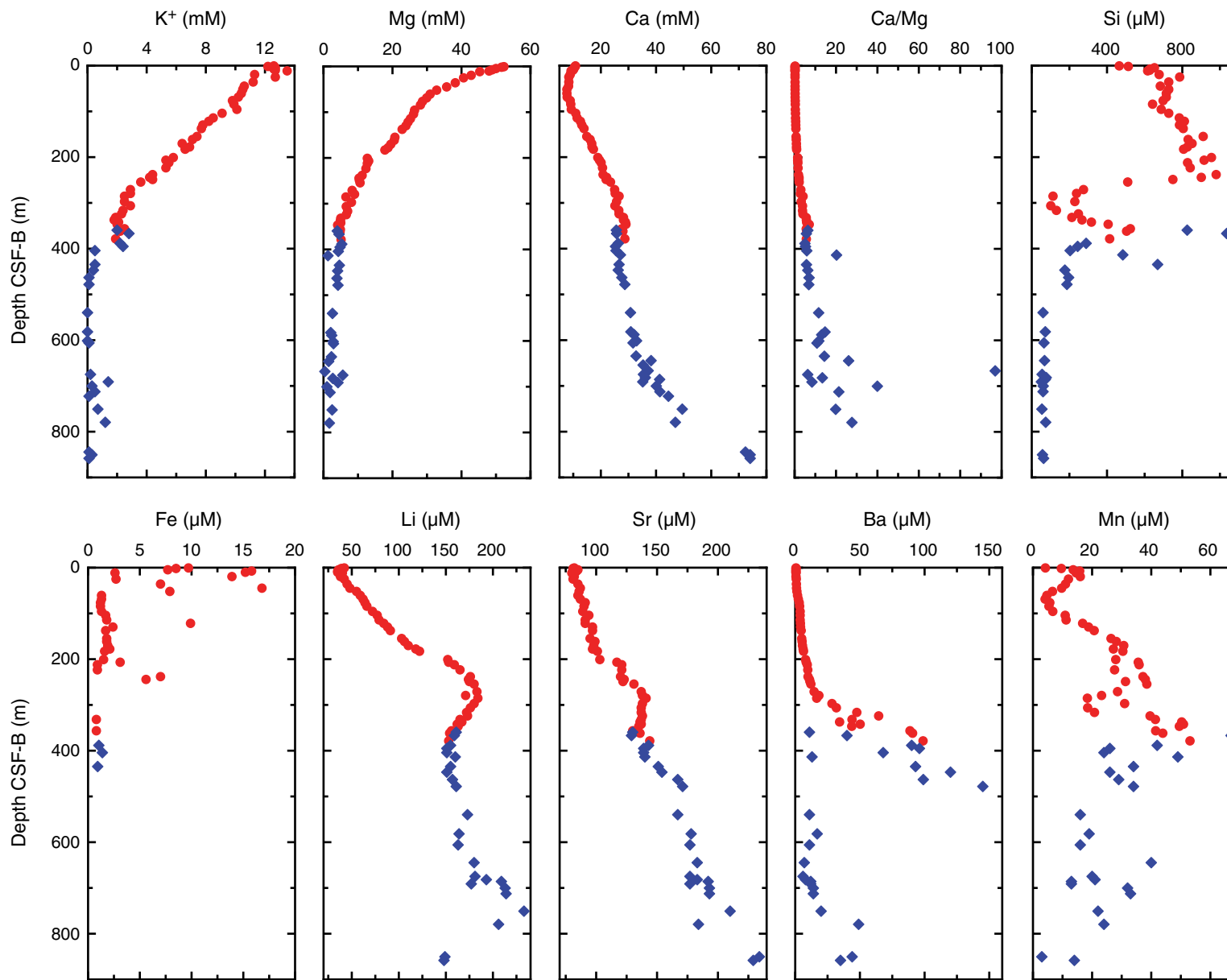


Figure F40. Methane concentrations in headspace samples, Holes C0011C (blue) and C0011D (red).

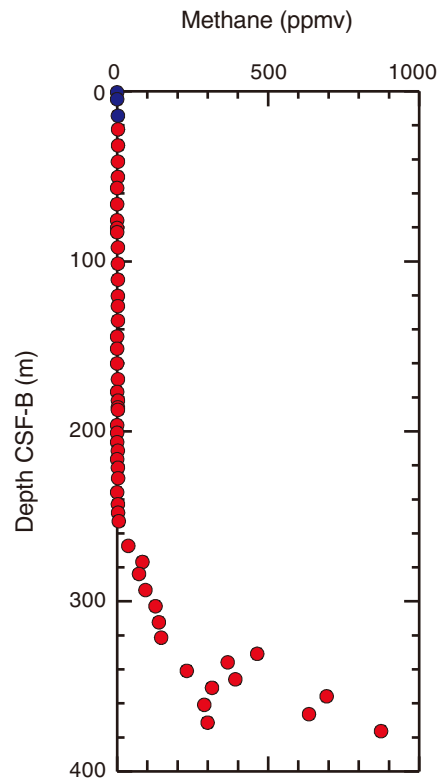


Figure F41. Calcium carbonate, total organic carbon (TOC), total nitrogen (TN), total sulfur (TS), and atomic ratios of TOC to TN (TOC/TN_{at}) in bulk sediment, Holes C0011C (blue circles) and C0011D (red circles).

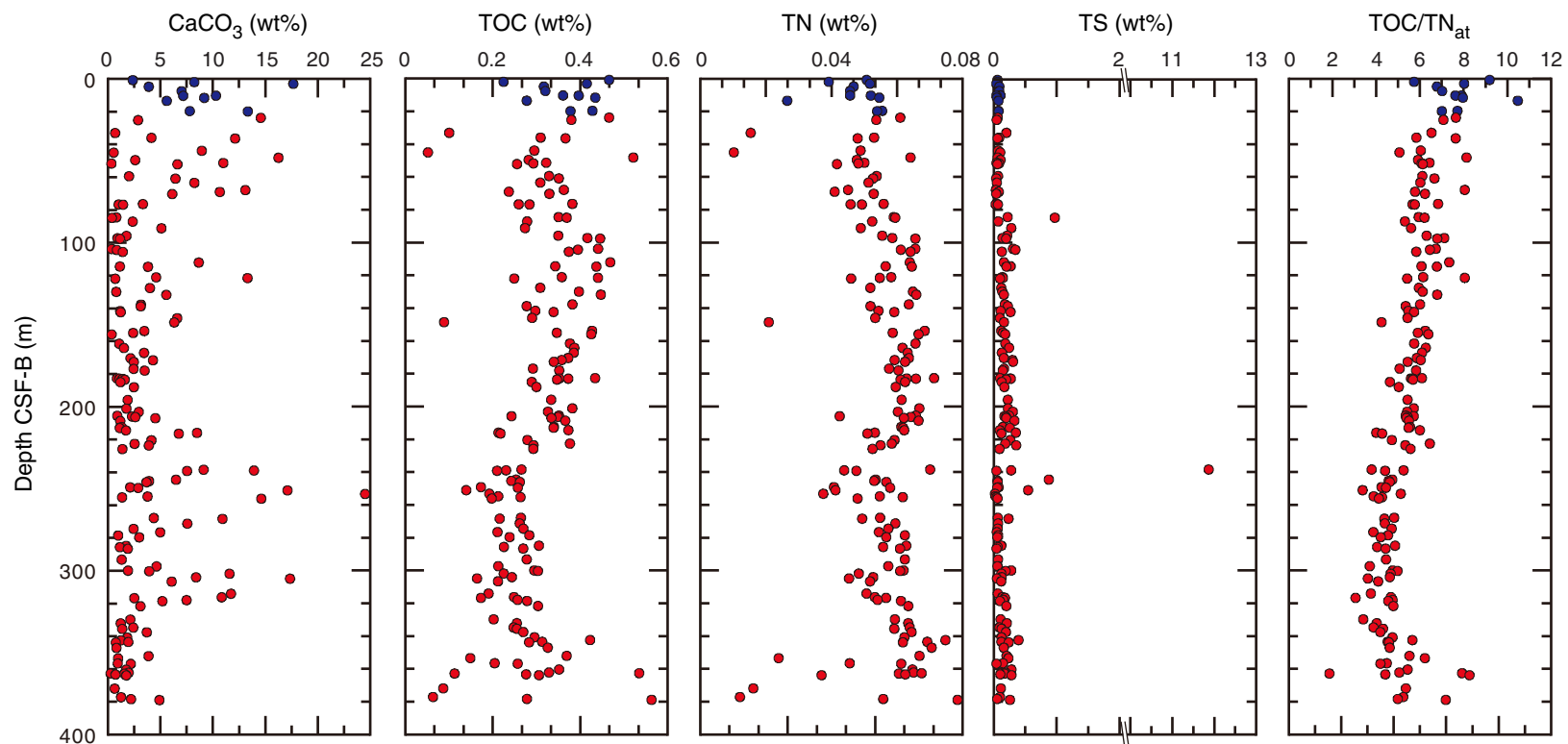


Figure F42. Sedimentary log, Holes C0012C and C0012D.

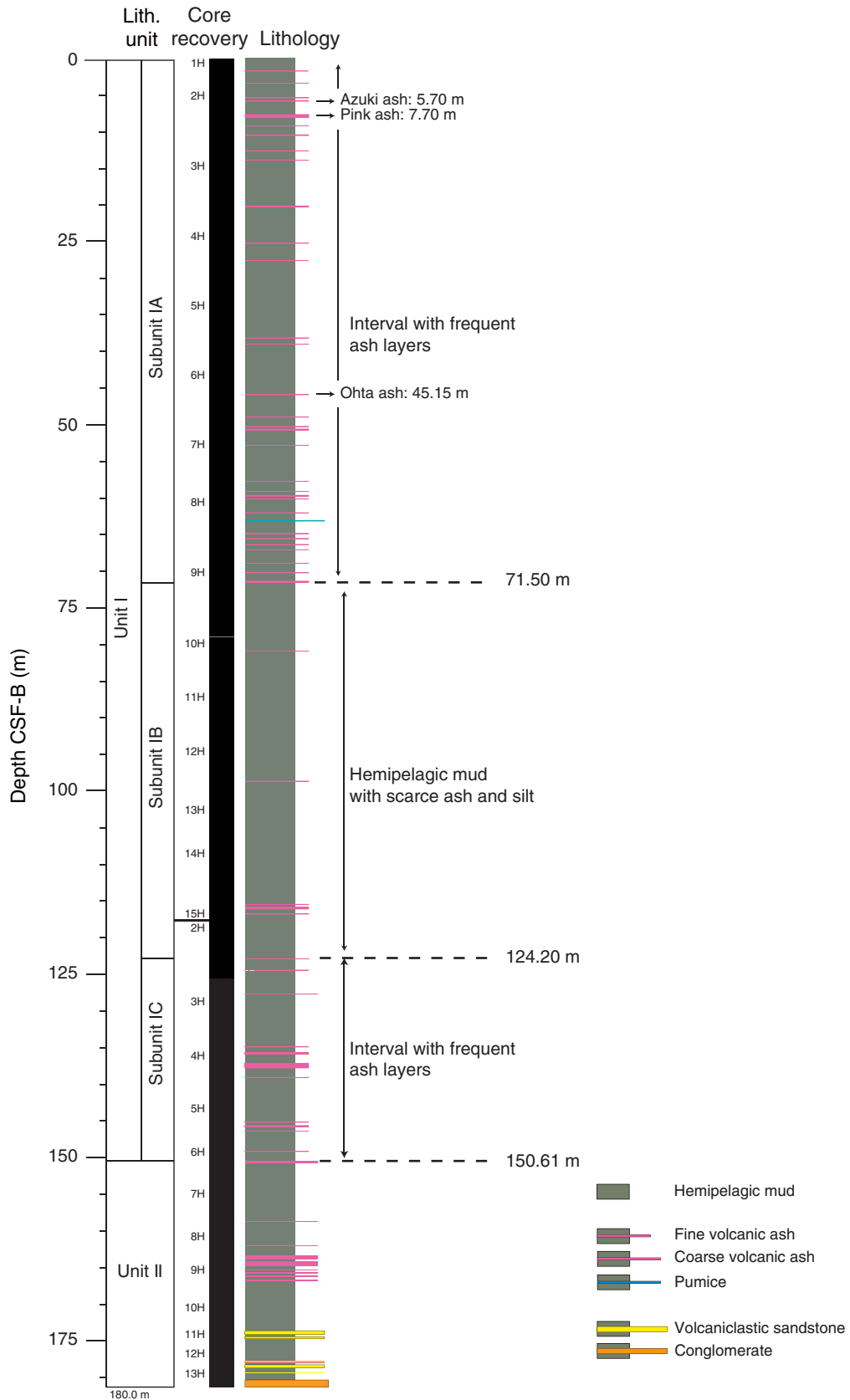


Figure F43. Summary of XRD data, Holes C0012C and C0012D. Unit and subunit boundaries are highlighted. Note the inexistence of a sharp Unit I/II boundary as observed on XRD data.

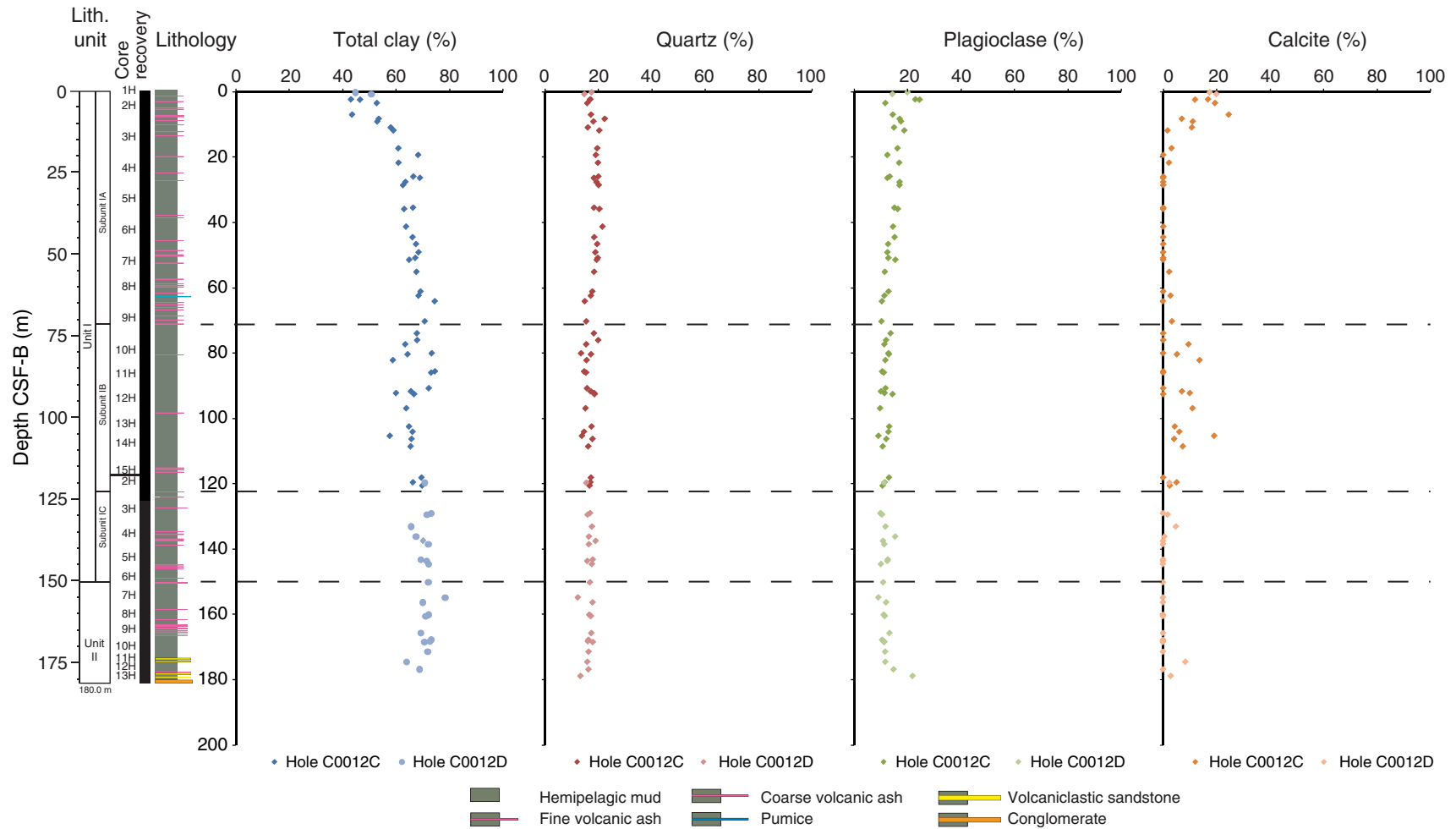


Figure F44. Variations of SiO₂, Al₂O₃, CaO, Fe₂O₃, MgO, MnO, and P₂O₅ as a function of depth at Site C0012 from X-ray fluorescence (XRF) data and comparison with Expedition 322 results.

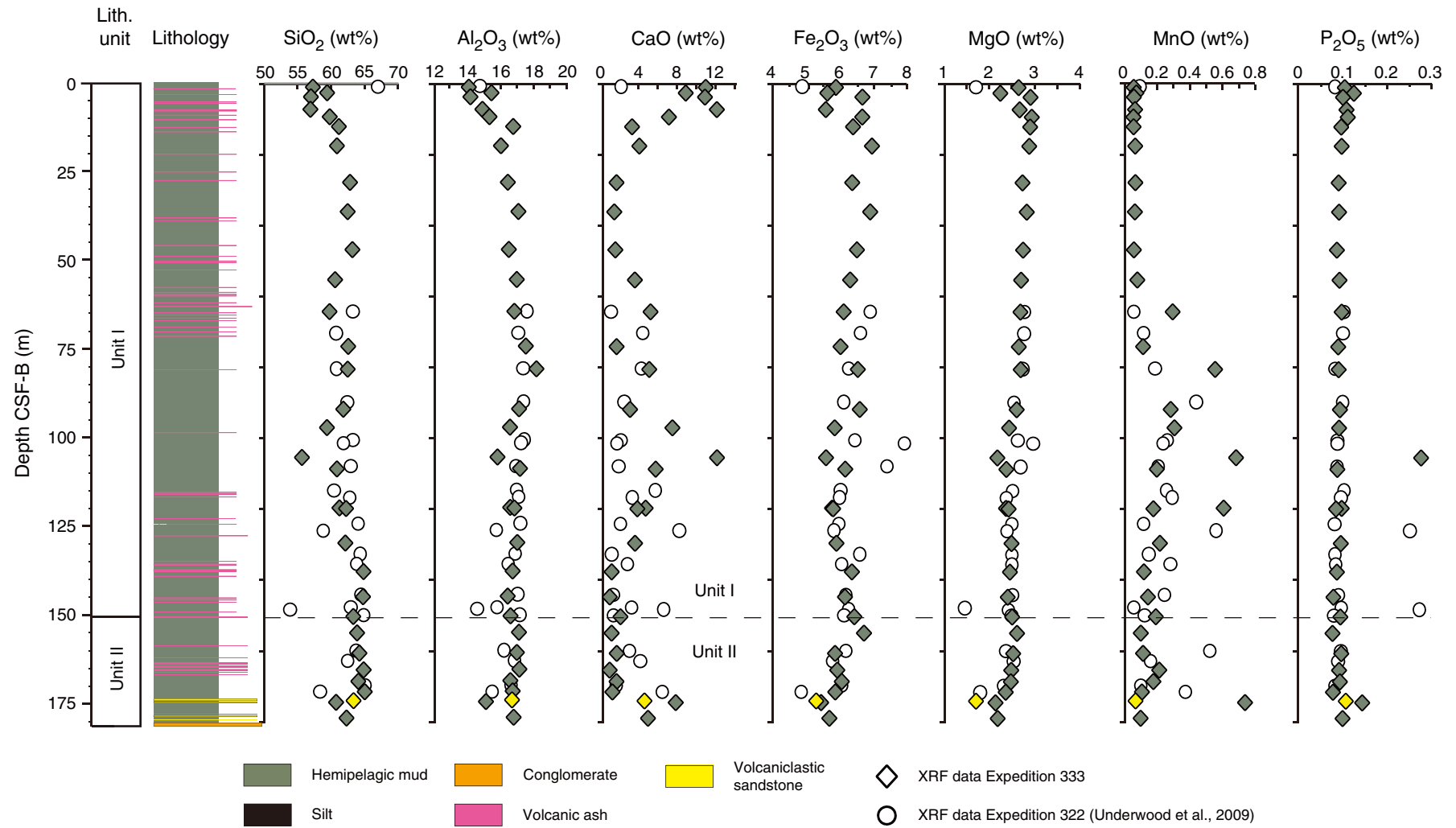


Figure F45. A. Distribution of bedding dip angles and deformation structures with depth, Holes C0012C and C0012D. Lines = boundaries between four zones defined based on dipping angle distribution. B. Equal-area stereographic projections (lower hemisphere) of bedding plane poles above 15 m CSF (Zone 1). C. Equal-area stereographic projections (lower hemisphere) of bedding planes and poles between 15 and 85 m CSF (Zone 2). D. Equal-area stereographic projections (lower hemisphere) of fault planes and poles (all zones).

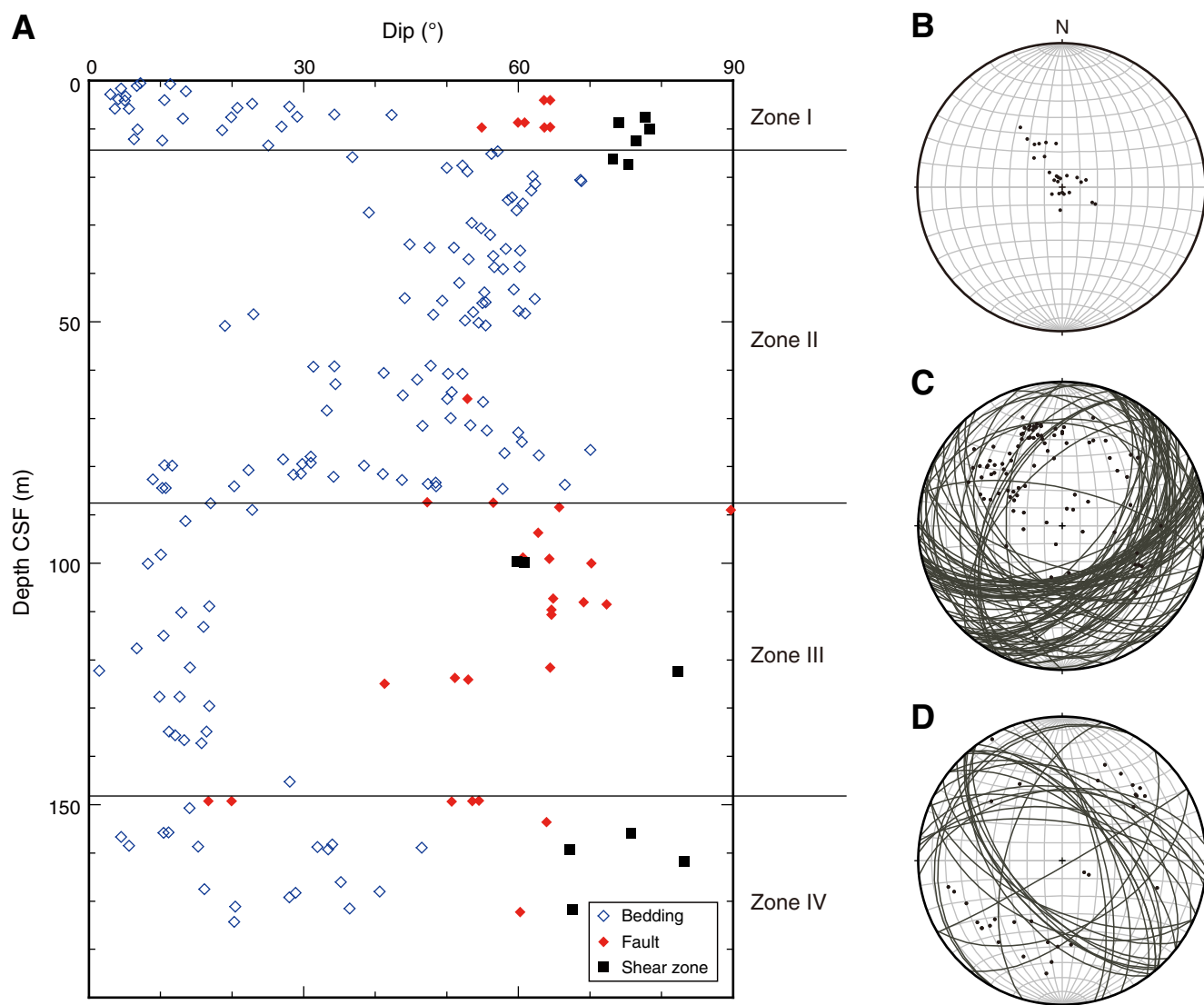


Figure F46. Correlation between Sites C0011 and C0012 based on remanent magnetization inclination and magnetic susceptibility. Chron and subchron correlations (red), tephra layer correlations (blue), and unconformity (red wavy) are indicated. Green box = ~80 m section that is missing from Site C0012, question mark = unclear magnetic polarity correlation.

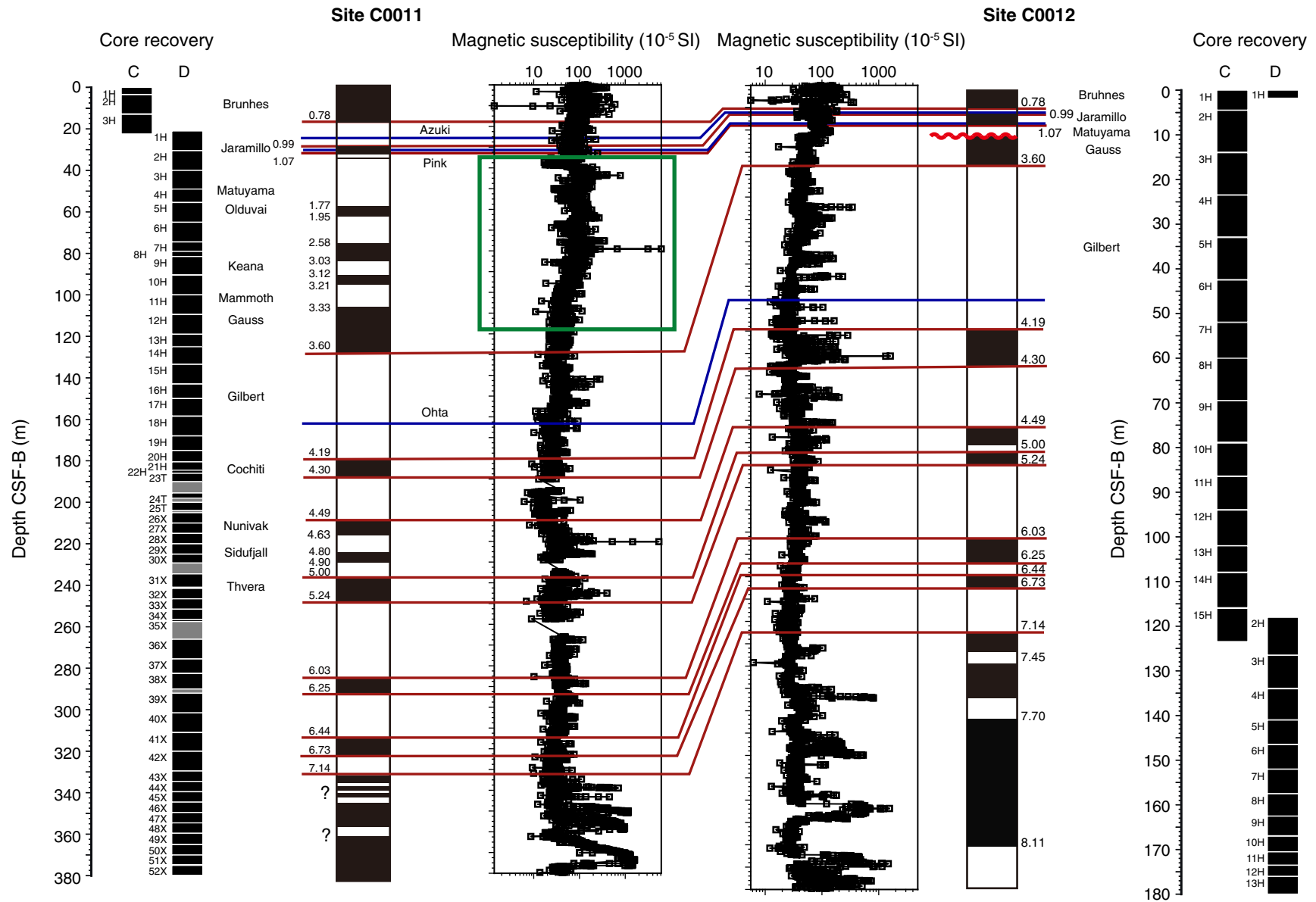


Figure F47. Bulk density, porosity, and grain density data, Site C0012. Solid symbols = results from Holes C0012C, C0012D, and C0012E; open symbols = results from Expedition 322 Hole C0012B. Sands are indicated by red squares (solid for Holes C0012C, C0012D, and C0012E and open for Hole C0012B). Light blue triangles = basalts from Holes C0012E, C0012F, and C0012G.

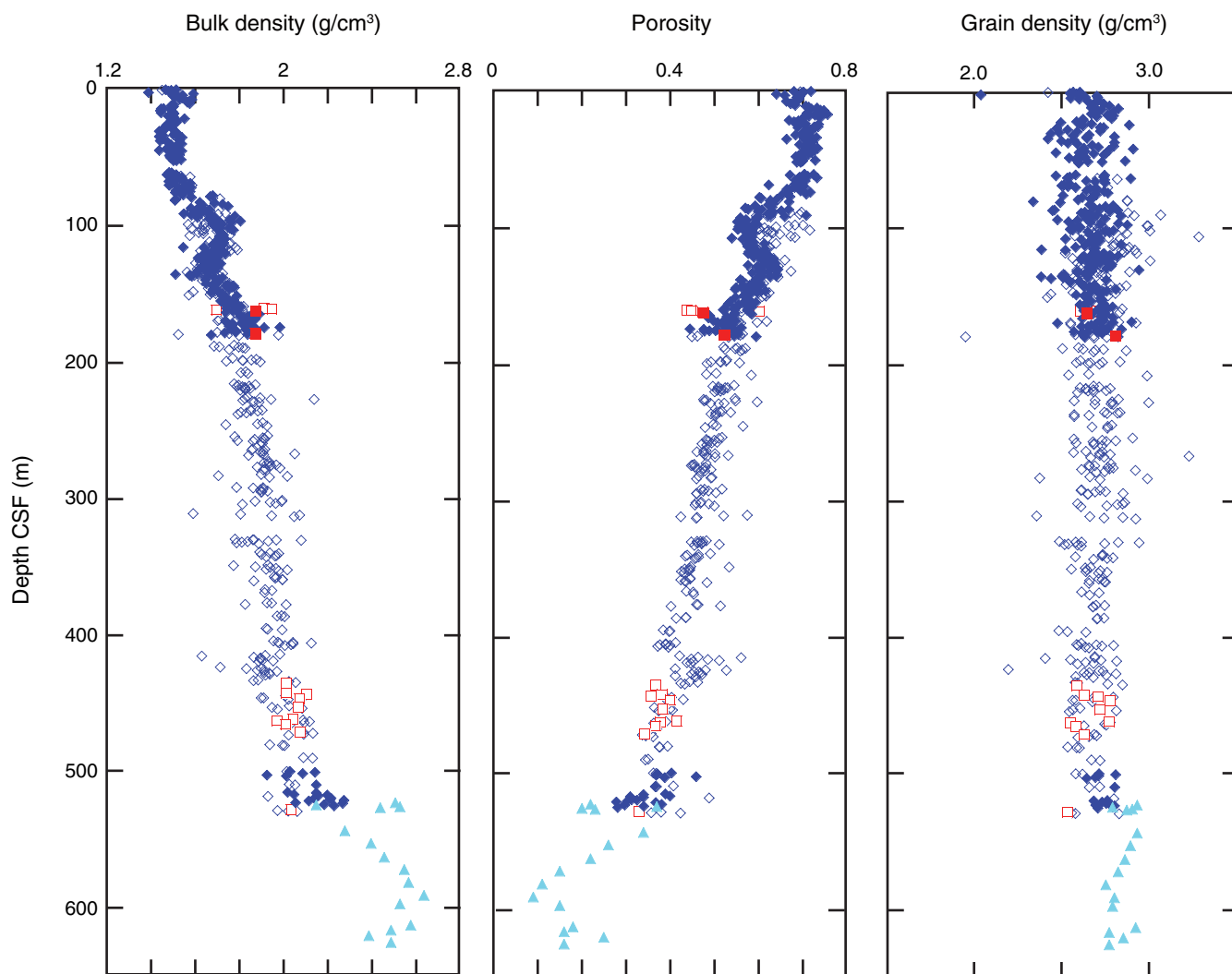


Figure F48. Comparison of porosity data from Site C0011 mudstones and Site C0012 mudstones.

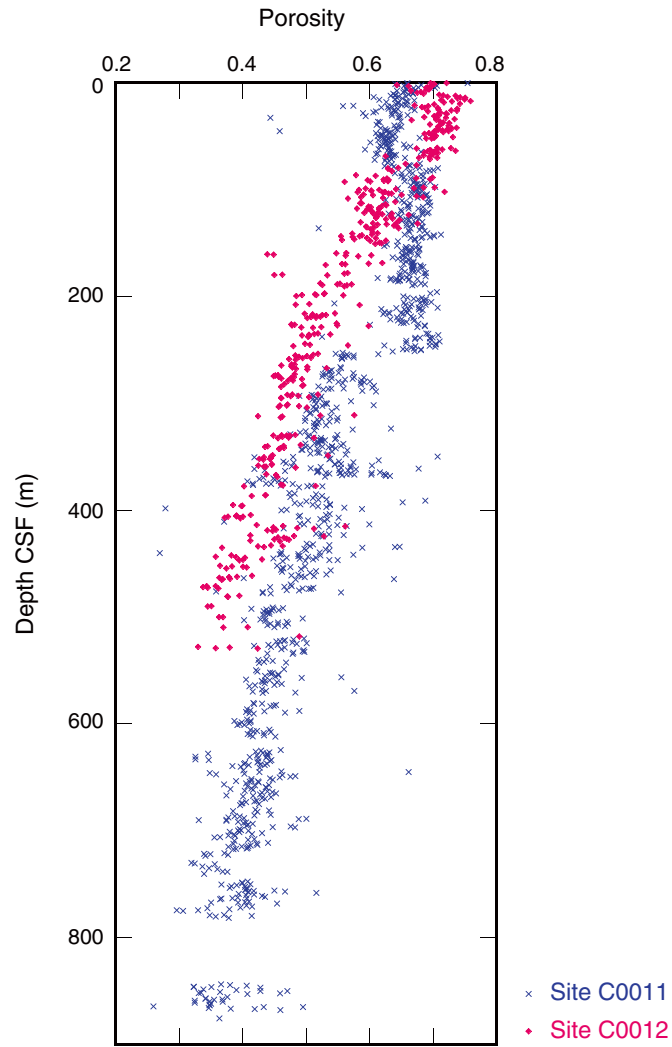


Figure F49. **A.** *P*-wave velocity in the *z*-direction measured on discrete samples. **B.** Vertical plane anisotropy of *P*-wave velocity determined from measurements on discrete samples. Positive is higher velocity in horizontal direction. **C.** Resistivity in the *z*-direction measured on discrete samples. **D.** Vertical plane anisotropy of resistivity determined from measurements on discrete samples. Positive is higher resistivity in horizontal direction.

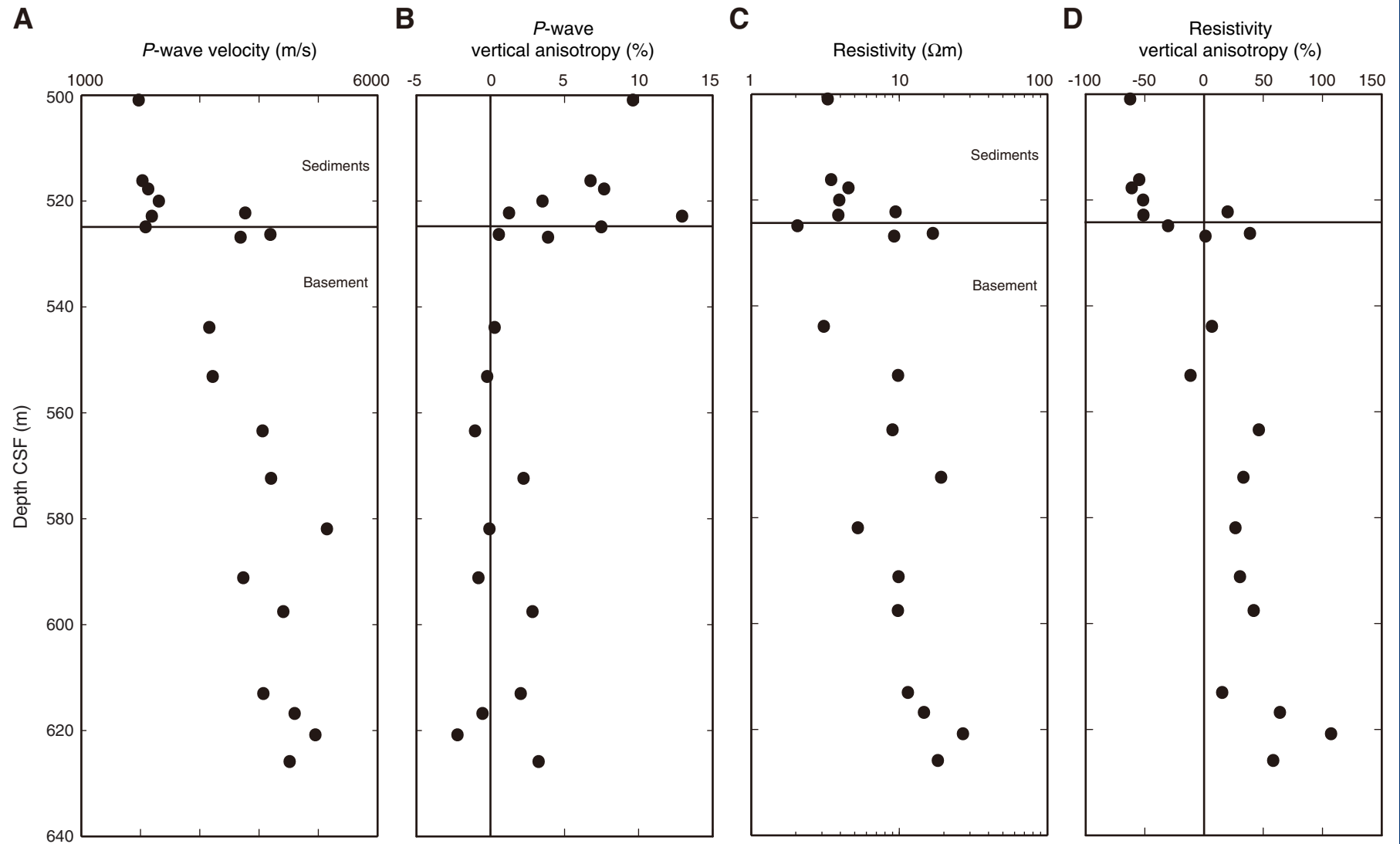


Figure F50. A. Volume of interstitial water recovered per length of interstitial water section (mL/cm) from Holes C0011C, C0011D, C0011E, and C0011G (red) and Expedition 322 Hole C00112A (blue). B. Dissolved sulfate profile.

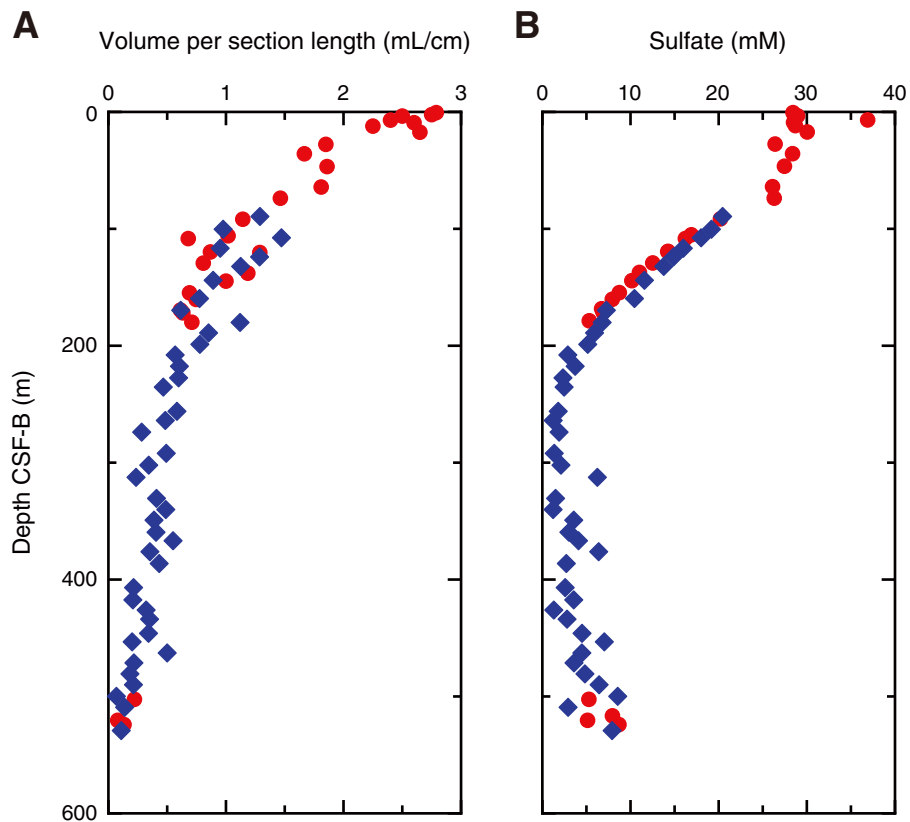


Figure F51. Interstitial water constituents (salinity, chlorinity, bromide, pH, alkalinity, sodium, ammonium, phosphate, Br/Cl, and boron) from Holes C0012C, C0012D, C0012E, and C0012G (red) and Expedition 322 Hole C00112A (blue).

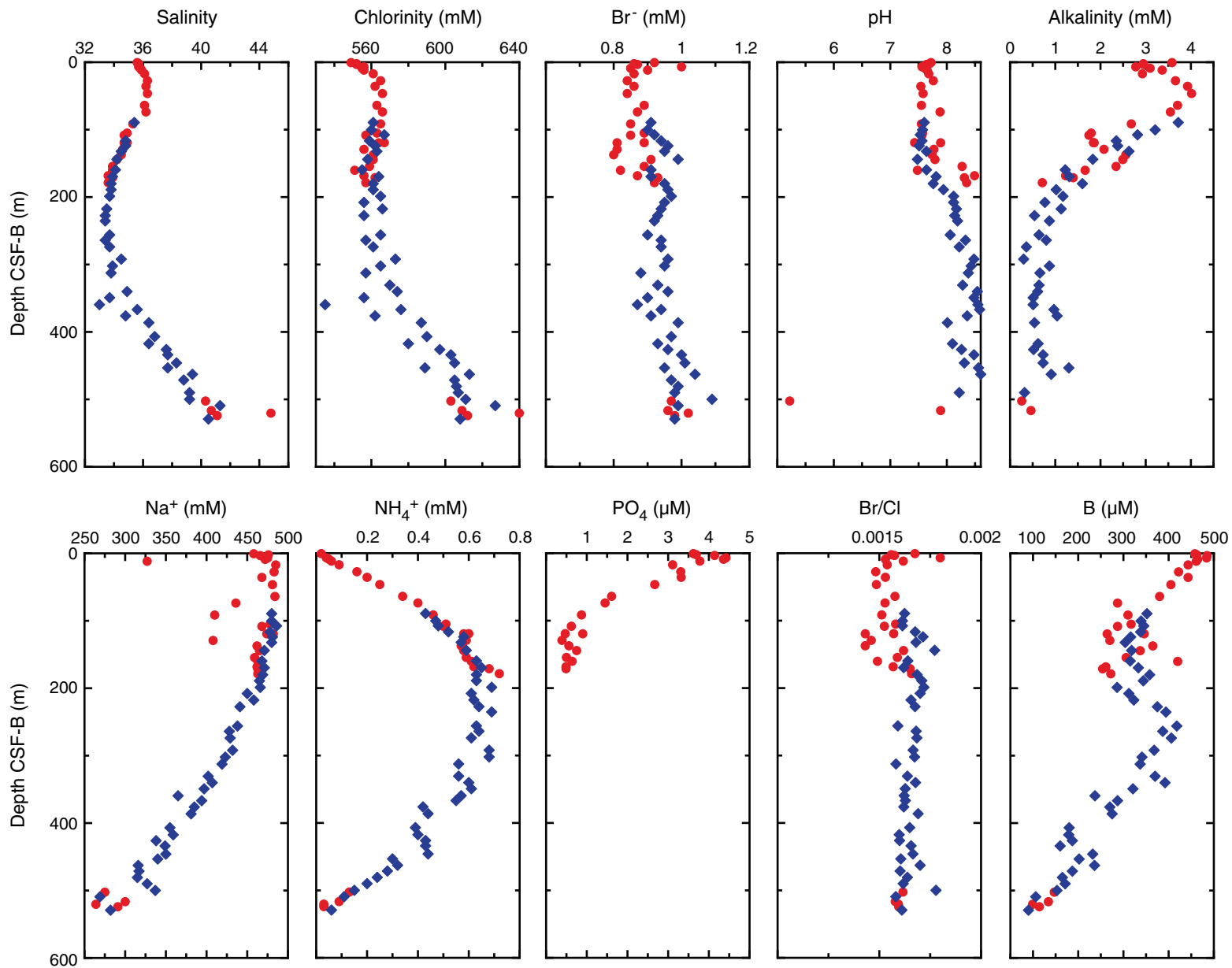


Figure F52. Interstitial water constituents (potassium, magnesium, calcium, Ca/Mg, silica, iron, lithium, strontium, barium, and manganese) from Holes C0012C, C0012D, C0012E, and C0012G (red) and Expedition 322 Hole C0012A (blue).

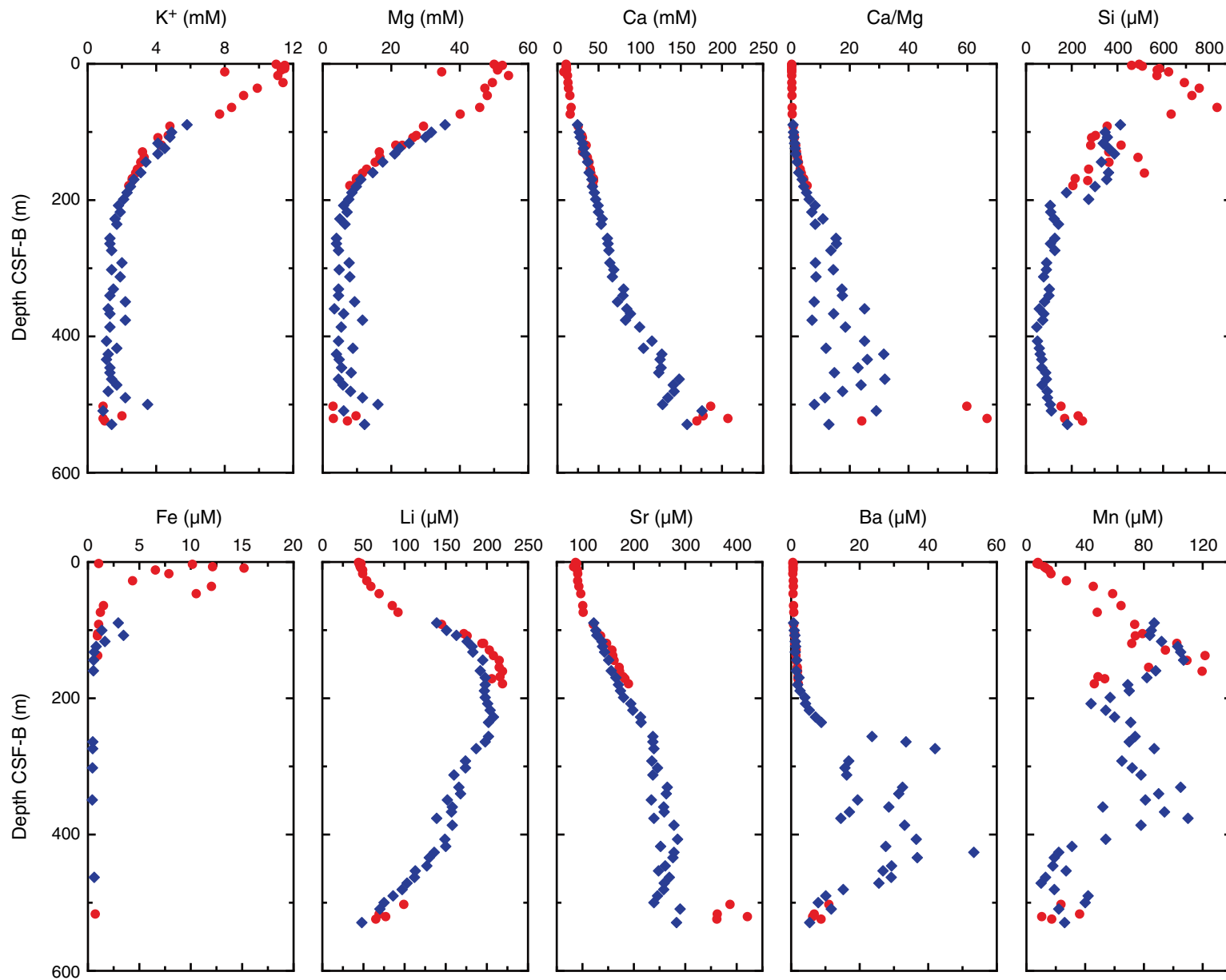


Figure F53. Methane, ethane, and C₁/C₂ ratios, Holes C0012C, C0012D, and C0012E. C₁/C₂ is set at 100,000.0 when ethane concentration is below detection.

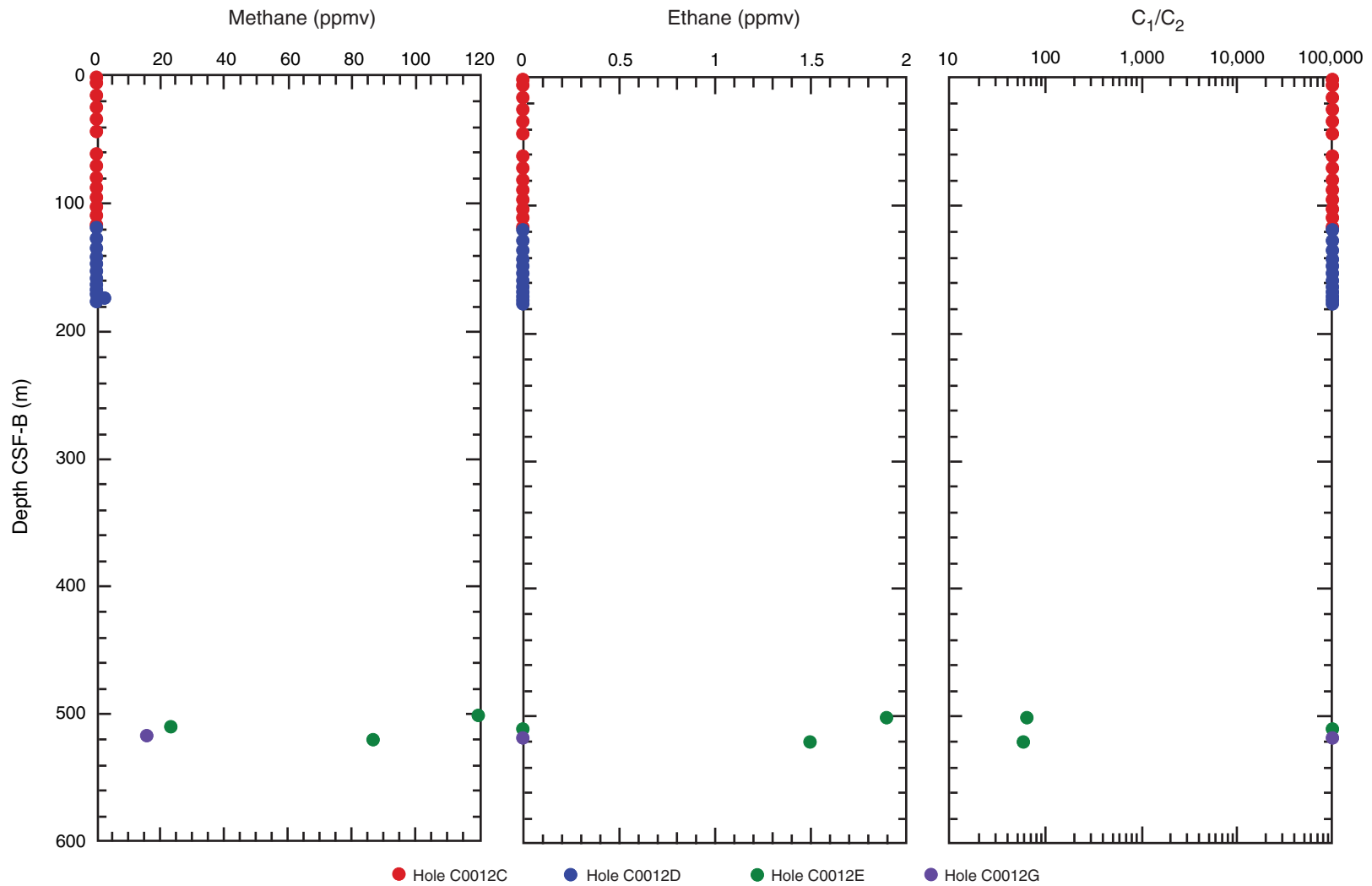


Figure F54. Calcium carbonate, total organic carbon (TOC), total nitrogen (TN), atomic ratios of TOC to TN (TOC/TN_{at}), and total sulfur (TS) in bulk sediment, Holes C0012C, C0012D, and C0012E.

